Aerosol Assisted Chemical Vapour Deposition of Photo-catalytic Composite and Doped TiO_2 Thin Films

This Thesis is submitted in partial fulfilment of the requirements for the Degree of Doctor of Chemistry.

Nicholas Philip Chadwick

University College London

Department of Chemistry

2015

Declaration

I, Nicholas Philip Chadwick, confirm that the work presented in this thesis is wholly my own. Where information has been derived and obtained from other sources I confirm that this has been indicated as such. All work is my own sparing TAS experiments, which were undertaken in collaboration with Dr. Andreas Kafizas.

Abstract

This thesis details the use of Aerosol Assisted Chemical Vapour Deposition (AACVD) to synthesise doped and composite titanium dioxide (TiO_2) thin films for use in technological applications. These applications range from advanced transparent coatings for self-cleaning windows to materials for the irradiation induced remediation of compromised water sources.

First, a TiO_2/SnO_2 composite, which had been synthesised and characterised previously, is investigated by combinatorial AACVD (C-AACVD) itself a novel form of AACVD which separates precursor streams until they are in the reactor. This achieved films which graduate from TiO_2 to SnO_2 allowing changes in physical and elemental structure to be easily related to variances in functional properties.

Next a new form of AACVD is used for the first time to provide insight into the growth of the TiO_2/SnO_2 composite, which is not achieved using combinatorial methods. Time Resolved AACVD (TR-AACVD) allows the creation of thin films that vary as a function of time, rather than elemental concentration as in combinatorial AACVD (C-AACVD). Advantageously many films can be created in a single deposition, allowing a full deposition to investigate the full growth of a material of interest.

Whilst nitrogen doped TiO_2 is a well characterised material within the scientific literature, questions still remain as to the true physical reasons for its functional properties. In this work Transient Absorption Spectroscopy (TAS) is used in conjunction with X-ray Photoelectron Spectroscopy (XPS) and photo-activity measurements to chart

how the material changes as a function of irradiation time, providing an idea of how nitrogen doped TiO_2 would fair in an environmental setting outside the laboratory.

Finally, capitalising on the production of nitrogen doped TiO_2, nitrogen and niobium co-doped TiO_2 is synthesised using combinatorial AACVD to create a film which graduates from N: TiO_2 to Nb: TiO_2 with co-doped states created in between. The incorporation of TCO and photo-catalytic properties in TiO_2 is explored.

Publications

Published

(1) Ponja, S. *et al*. Aerosol Assisted Chemical Vapour Deposition of Hydrophobic TiO_2–SnO_2 Composite Film with Novel Microstructure and Enhanced Photo-catalytic Activity. J. Mater. Chem. A 1, 6271 (2013). (Chapter III)

(2) Chadwick, N*. et al*. Combinatorial Aerosol Assisted Chemical Vapour Deposition of a Photo-catalytic Mixed SnO_2/TiO_2 Thin Film. J. Mater. Chem. A 2, 5108 (2014). (Chapter III)

(3) Chadwick, N. *et al.* The Use of Time Resolved Aerosol Assisted Chemical Vapour Deposition in Mapping Metal Oxide Thin Film Growth and Fine Tuning Functional Properties. J. Mater. Chem. A 00, 1–9 (2014). (Chapter IV)

(4) Bawaked, S. M. *et al.* Aerosol Assisted Chemical Vapour Deposition of Conductive and Photo-catalytically Active Tantalum Doped Titanium Dioxide Films. J. Mater. Chem. A 2, 12849 (2014).

(5) Sathasivam, S. *et al*. Combinatorial Atmospheric Pressure CVD of a Composite TiO_2/SnO_2 Thin Film. Chem. Vap. Depos. 20, 69–79 (2014).

(6) Sathasivam, S. *et al*. Tungsten Doped TiO_2 with Enhanced Photo-catalytic and Opto-electrical Properties via Aerosol Assisted Chemical Vapour Deposition. Sci. Rep. 5, 10952 (2015).

In Preparation

(7) Work from Chapter V: Chadwick, N.; Kafizas, A.; Quesada Cabrera, R.; Sotelo Vasquez, C.; Basahel, S. N.; Althabaiti, S. A.; Alyoubi, A. Q.; Durrant, J.; Parkin, I. P.; Carmalt, C. J.

(8) Work from Chapter VI: Chadwick, N.; Glover, E.; Mokhtar, M.; Bawaked, S. M.; Obaid, A. Y; Parkin, I. P.; Carmalt, C. J.

Acknowledgements

There are many I would like to thank.

I thank my best friend Leanne, for being a constant source of inspiration and for pushing me most when I needed it. Unfortunately, I am eternally indebted to her and I have no idea how to repay her.

My other thanks are directed to my principal supervisor Professor Claire Carmalt, who gave me the opportunity to pursue research in materials science at University College London and I am extremely grateful. Claire has been a fantastic supervisor and I couldn't recommend her enough. My secondary supervisor Professor Ivan Parkin also deserves my thanks as he has, despite his incredibly busy schedule, always been there for support and incredibly reliable. I am thus indebted to these two people especially. Thank you.

I would like to thank my mum and dad for being the best, most supportive and caring people I know.

My friends also deserve a mention for keeping me sane.

List of Figure and Tables

Chapter I: Introduction and Literature Review

Chapter II: Methods

Chapter III: Combinatorial Aerosol Assisted Chemical Vapour Deposition of a Photo-Catalytic Mixed SnO_2/ TiO_2 Thin Film

Chapter V: The UV – Induced Surface Segregation of Interstitial Nitrogen and Its Stoichiometric Contribution to the Observed Photo-catalytic Rate in N-TiO_2

Chapter VI: The Incorporation of High Photo-catalytic Activity and Low Resistivity in N/Nb Co-doped TiO_2 Thin Films by Combinatorial AACVD

Chapter VII: Conclusions and Future Work

No figures.

Acronyms

TiO_2 – Titanium dioxide

AACVD – Aerosol Assisted Chemical Vapour Deposition

C-AACVD – Combinatorial Aersol Assisted Chemical Vapour Deposition

TR-AACVD – Time Resolved Aerosol Assisted Chemical Vapour Deposition

XRD – X-ray Diffraction

XPS – X-ray Photoelectron Spectroscopy

SEM – Scanning Electron Microscopy

UV/Vis – Ultraviolet-visible

Rz – Resazurin

TAS – Transient Absorption Spectroscopy

DOS – Density of States

$NTiO_2$-20 – 20% doped $NTiO_2$

$NTiO_2$-200 – 200% doped $NTiO_2$

BPA – Bisphenol A

UN – United Nations

WHO – World Health Organisation

FQE – Formal Quantum Efficiency

FQY – Formal Quantum Yield

HOMO – Highest Occupied Molecular Orbital

LUMO – Lowest Unoccupied Molecular Orbital

Table of Contents

1 Chapter I: Introduction

There has been much focus in the past few decades on creating and commercialising technologies with the concept of ambient energy utilisation as their core design principle. Sustained research in these areas has heralded advances in photovoltaic solar panel efficiencies and transparent conducting oxides which find usage in a plethora of applications, from dye sensitised solar cells to flat screen televisions.[1–3] One particular area of discourse which has pursued this concept of ambient energy utilisation is the field of photo-catalysis.

The sun is known to provide the earth with more energy, through irradiance, in a singular day than mankind is currently capable of using within an entire year.[4] It represents an underutilised and powerful energy source which can be captured and used in many ways. The main usage that first comes to mind is for powering the everyday lives of mankind. With a growing population this need for energy becomes an imperative. In many ways this energy is used to create products which eventually contribute pollution to the environment. This includes small organic molecules as well as bacteria and viruses.[5]

One of the major goals of the photo-catalysis community is to create materials which can utilise ambient energy, given from the sun, to remove and destroy these pollutants. In this way mankind can begin to take responsibility for the environmental damage its pursuit of growth has resulted in.[6,7]

The process of photo-catalysis involves a medium whose band gap (the energy difference between a materials valence and conduction band) is attuned to the energy of ambient light. The medium then uses this energy to create charge carriers which

travel to the surface to undergo surface redox reactions and effect chemical change upon the environment in the immediate vicinity of the medium.[8]

In this work a particular medium, composite and doped TiO_2 thin films, is explored and characterised to achieve greater understanding of their ability to fulfil the role outlined.

Before a material can be assessed for its suitability to solve a problem, the problem must be first defined. One particular role TiO_2 is touted to fulfil is the light induced sterilisation of compromised water sources.

1.1 The Issue of Clean Water

Titanium dioxide is hypothesised for use in many applications, such as photo-catalysis of water for hydrogen production, and is used commercially as a self-cleaning coating for windows. However, this thesis is focused on the production of thin films based on TiO_2 for use in the purification of water. Before TiO_2 can be truly considered fit for purpose in solving the problems it is touted to be capable of, one must first identify the situations and reasons for pursuing such a line of research, only by doing so can the disadvantages TiO_2 exhibits be changed. As such it is necessary to quantify the problems posed so that TiO_2 can be assessed for its capability in cleaning water.

1.2 Water as a Source of Disease

Clean sources of water are an issue worldwide, for both first and third world nations. The degree of severity varies, however the necessity of clean non-toxic water sources for human consumption is a biological fact. The human body can survive for roughly a month without food, providing water is available. Without water the human body will perish within the space of several days.[9] Therefore obtaining and maintaining large bodies of clean water is an imperative. In Britain, as an example, we are one of the most

developed nations on the planet with an extensive and advanced infrastructure for the production and distribution of clean water.

For less developed regions in sub Saharan Africa, areas of Mexico, South East Asia and many more, this combination of infrastructure and access to healthcare is not as prevalent, if at all present. As a result, cases of diseases related to poor hygiene are numerous and account for the deaths of many children and adults alike on a yearly basis. Clean accessible and affordable drinking water is defined by the United Nations Committee on Economic, Social and Cultural Rights as a human right.[10] With this is mind, it is reported by the World Health Organisation that 39% of the world's population or 2.6 billion people still do not have access to improved sanitary conditions and 750 million lack access to clean drinking water altogether.[11] Open defecation, which presents a serious problem in terms of waterborne diseases and potential fouling of clean sources of water, is still prevalent in the developing world with 1.1 billion people or 15% of the world population having no other sanitary options.[12] Diarrhoea is a dangerous illness in the third world and a symptom of many water borne diseases. It is estimated that 2,300 people die each day of dehydration as a result of diarrhoea, this equates to 842,000 people a year. Unsurprisingly, 82% of those who lack access to sanitary water sources live in rural regions, with only 18% living in cities or towns.

This paints a stark picture and has serious ramifications for everyone involved. Many families in third world countries rely on their children to provide an income for the whole family. If family members become ill, not only does the family lack an important source of income, they also have to misappropriate resources looking after the ill family member. Sickness therefore very quickly becomes a barrier to prosperity as the family

slowly sinks further into poverty whilst trying to care for their family members. Access to clean drinking water is therefore of interest for the eradication of poverty. As instances of water borne infection would decrease as a direct result of clean drinking water, people in the affected regions would lead healthier lives and live longer to provide incomes for themselves and their families, helping to elevate the economic standing of themselves, their family and everyone around them.

1.3 The Issue of Small Organic Molecules

Water can also be a source for small organic molecules, which can be detrimental to health. This issue has continued to increase proportionally with the prevalence of plastics and medicines, associated with the modern world, which create specific metabolites and by-products upon interaction with the human body and livestock.

1.3.1 Water Borne Estrogens

Estradiol is a class of estrogens, themselves natural hormones found in the human body (Figure 1.1). They are responsible for driving specific hormonal pathways in the body and are essential for maintaining the reproductive cycle in both female and male human beings. They are also vital to maintaining correct bone structure amongst many other functions. However, extra-cellular sources of oestrogens can pose a serious problem in human physiology. It is regularly associated with lower sperm counts in males and has been linked to an observed global reduction in worldwide sperm counts in men.[13]

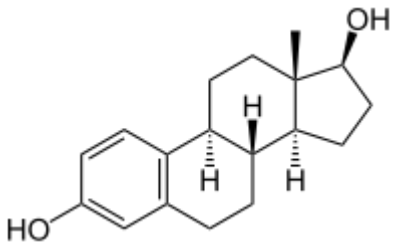

Figure 1.1: The structure of Estradiol, specifically 17B-Estradiol

In the 1980s the first evidence of synthetic estrogens exerting adverse health effects upon an environmental population was published. The authors reported that elevated levels of estrogens found in UK natural fresh water sources, such as rivers and lakes, were consistent with sexual abnormalities found in many different freshwater fish populations. The degree of abnormalities ranged from low levels of androgyny to some specimens exhibiting both male and female sex organs.[14] Subsequent studies on populations of breeding zebrafish found that even low levels of environmental estrogen exposure resulted in decreased breeding success in the overall population.[15]

With this in mind, rivers were mapped to assess the concentrations of estrogens present in the water. In the British rivers Lea and Nene, levels of estrone (another estrogen) and estradiol were found to vary between 0.4 to 12.2ng/l and 0.4 to 4.3ng/l respectively. Further studies found that exposure at these levels over the course of seven years is sufficient to decimate the entire fish population of a lake, as the male population is slowly feminised resulting in less procreation.[16]

Recent studies carried out at the University of Montreal have found that sewage treatment plants, which possess no facilities to treat water for estrogens, transfer 90 times the critical amount of estrogen back in the environment. The critical amount is the amount required for adverse effects to take place and is set at 1ng/l.[17] This massive

increase is attributed to a concurrent increase in the amount of people consuming oral contraceptives which accumulates high concentrations of unprocessed estrogens within the body and are then expelled via urine or faeces. The estrogens then continue to enter natural and fresh water sources.

Studies have also established that elevated levels of estrogens can negatively influence the immune system in humans.[18]

1.3.2 Bisphenol A

Bis-Phenol A (BPA) (Figure 1.2) is a molecule employed for use in the synthesis of many modern day plastics and epoxy resins. The plastics are tough and transparent, thus a favourable material for the production of plastic bottles and the like. It is also prevalent in canned food containers and is used to line the inside of water pipes. With this in mind; the leaching of unreacted monomer units present in these products and the subsequent transferral into the human body via consumption of food and water, is of concern in the light of increasing evidence that BPA poses several developmental and health risks to the human body. BPA is commonly found in potable water sources using in drinking water.[19]

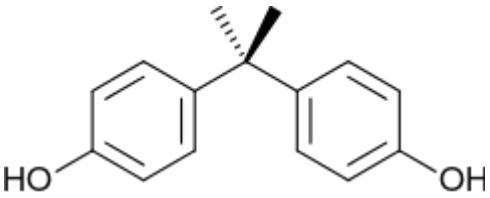

Figure 1.2: The skeletal structure of Bisphenol A (BPA).

The use of BPA in the synthesis of plastics is widespread, as the chemistry is easily accessible and well documented.

As a result, world production was 1 million tons in the 1980s,[20] which grew to more than 2.2 million tons in 2009.[21] It is therefore classed as a high volume production chemical.[22] Not surprisingly US consumption in 2003 was recorded at 856,000 tons, of which 72% was used to make polycarbonate plastic and 21% for the synthesis of epoxy resins.[23] At present however, less than 5% of the BPA produced in the US is used in food contact applications,[24] but remains highly prevalent in the canned food industry and in printing applications, such as sales receipts. [25]

Many Environmental and food safety organisations that currently assert that BPA is safe in low concentrations, recognise that uncertainties still exist and thus further study is currently being pursued.[26]

Bisphenol A is a xenoestrogen, which means, despite displaying little chemical similarity to estradiol or natural estrogens produced by the human endocrine system, it is able to bind and interact with estrogen receptors found within the human body. It was first discovered in 1891 by Aleksandr Dianin[27] but little work was done until the 1930s when it was proposed as a synthetic estrogen replacement by Charles Dodds.[28] Subsequent work found that it bound to estrogen receptors 37,000 worse compared to estradiol itself.[29]

However in 2007, reports suggested that as a xenoestrogen it activated an alternative endocrine pathway than estrodiol, whilst still effecting similar physiological phenomena within the body as estrodiol,[30] hence explaining why BPA still represents a problem in water sources. It was not until 2009 that BPA was linked with adverse side effects at low dosages.[31] Since then it has been linked with increasing levels of obesity, sexual dysfunction,[32] propagation of genetic mutations in children,[33] stunting of testicle

growth[34] and in some cases cancer.[35] A telling example is of chemical factory workers in china exposed to BPA on a daily basis reporting many of the expected symptoms of endocrine manipulation such as sexual dysfunction, lower libido and weight gain.[32]

The role of BPA is still under investigation but recent evidence suggests that constant low level exposure present in the modern world is contributing, in the same manner as estradiol, to a global reduction in sperm count in human males.[36]

1.3.3 Antidepressants

Another prevalent class of organic molecules regularly found in drinking water throughout the first world are antidepressants. Many of the antidepressant molecules administered are left untouched by the body and excreted and thus end up in waste water sources. A study conducted in 2011 identified a link between exposure to serotonin uptake inhibitor (SSRI) antidepressants during pregnancy and an increase in observed autism spectrum disorders (ASDs) in the children who were subsequently born.[37] Another study has also linked long term low level exposure of antidepressants, consistent with expected levels found in environmental conditions, to the activation of genes associated with autism in the brain cells of fathead minnows.[38] Whilst this does not equate to a causal link for antidepressants elevating the likelihood of autism in humans it does demonstrate that even in small concentrations antidepressants can alter the brain chemistry of vertebrates.

1.3.4 The Need for Removal

It is abundantly clear that a method for removing these contaminants is required, which does not discriminate between bacterium, virus, plasticiser or antidepressant. Even if evidence for detrimental health effects are not concrete, for the sake of posterity,

developing techniques and technologies capable of permanently removing such contaminants from water sources is highly desirable from a health care, poverty and environmental perspective. The chemicals and bacteria described previously all detrimentally effect the natural world which we inhabit, whether it is nano-gram per litre concentrations of BPA in lakes, which are capable of devastating entire fish populations, or water borne diseases which tax the resources of already struggling families and healthcare infrastructure in the third world. Clean water for both consumption and the natural world is an imperative to ensure the flourishing of the planet and humanity in a positive manner. Thus the positives far outweigh the negatives in the need for developing such a technology. Such a technology would also have advantages in applications that are not as immediate in urgency but still a vital requirement such as in spaceflight, where water must be reused and maintained as no external sources exist.

1.3.5 Conventional Methods for the Purification of Water – UV Irradiation

In many areas of the world such as Africa and Asia bottled water is the only source of clean drinking water, although sewer systems and piped water systems exist, water sources that supply these populations still contain bacteria and natural fauna that can cause mild diarrhoea and sickness. [39] A large proportion of bottled water is irradiated with ultra violet light to prevent any potential bacteria or pathogen from being able to enter into the human body. This method works by causing mutations in the DNA of the bacteria and preventing a bacterium to carry out its normal cellular functions and hence cause disease.[40] The method is limited only by the fact that the water must be clear as possible to achieve maximum exposure to the ultraviolet light source as contact with the bacteria and the ultraviolet rays must occur to cause the DNA mutations which

eventually inactivate or kill the bacteria. It is also not suitable for the sterilisation of heavily soiled water, which often contains decaying organic matter and soil as well as faecal matter which stops the effectiveness of UV irradiation due to attenuation of the intensity of the UV rays used to irradiate the water. It also fails to remove small organic molecules which are largely unaffected by UV irradiation, with higher energy wavelengths sometimes required.

Thus for a better method of water purification, a material or technology is required that indiscriminately distributes energy throughout the water that is capable of effecting significant chemical change upon its target to render it inactive or destroyed.

1.4 Semiconductor Photo-catalysis for the Removal of Waterborne Agents

One method explored within the literature for the photon induced sterilisation of water is the use of metal oxide semiconductors, and in this instance TiO_2, for the photon-induced production of hydroxyl radicals at the TiO_2/ water phase boundary, which are capable of destroying and inactivating bacteria, viruses and small organic molecules alike.

1.5 What is a Semiconductor?

Semiconductors are the basis of the modern world; without them the transistor is impossible and the computer age, which has enabled such great levels of human prosperity in the past 70 years, would not have happened. This success can be attributed to advances in quantum theory; specifically the work of Schrodinger, Dirac, Fermi and Einstein, which helped explain the physical properties of these materials.[41–46] This is further compounded by the ability to synthesise very pure materials of which a high level of control exists in creating specific elemental compositions. The most common

semiconductors in use today are silicon and germanium and this is for their use in the fabrication of transistors for use in computing, which pervades society. There are however many compounds which are semiconductors too, such as metal oxides and sulfides.[47,48]

Semiconductors exhibit conductivities between a metal and an insulator. They also exhibit an increase in conductivity as temperature increases, contrary to what is observed in metals. To explain these phenomena, an understanding of the electronic structure and how it compares with metals and insulators is necessary.

1.6 Band Theory and Semiconductor Electronic Structure

In an individual atom, electrons occupy discrete energy levels or orbitals, described by quantum mechanics, and upon excitation can be promoted between these levels (Figure 1.3).

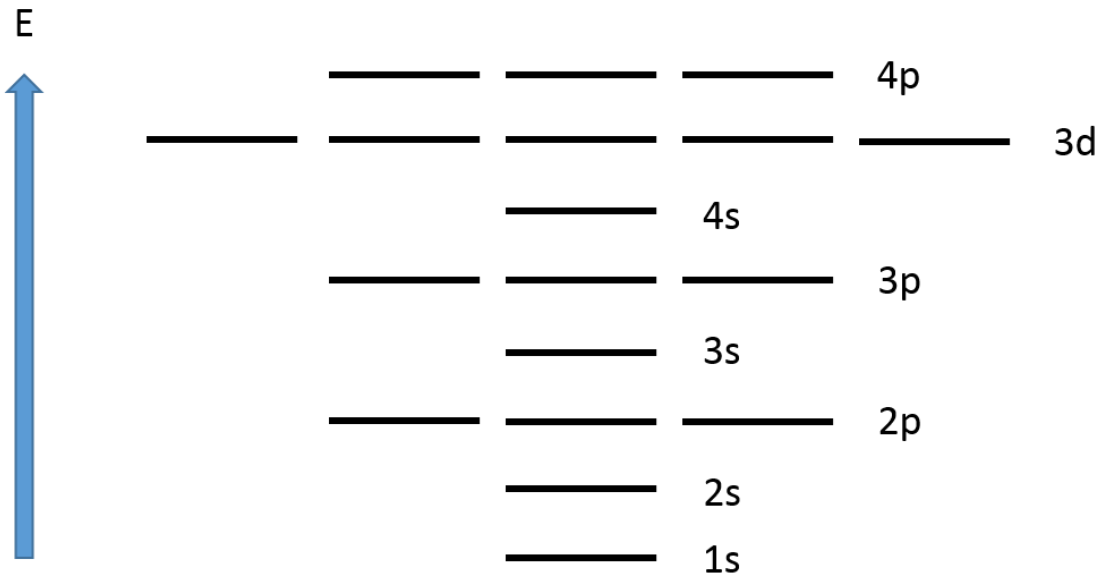

Figure 1.3: A schematic showing the distribution of atomic energy levels relative to each other as a function of energy.

The same can be said for molecules which exhibit molecular orbitals which are the product of the addition of the atomic orbitals of the constituent atoms. As the number of constituent atoms increases the amount of atomic orbitals which contribute to the formation of the molecular orbitals also increases all occupying discrete energy levels, as the molecule increases in size towards a solid, which is in essence a large molecule, the population of these energy levels becomes so dense that they form a continuum (Figure 1.4).

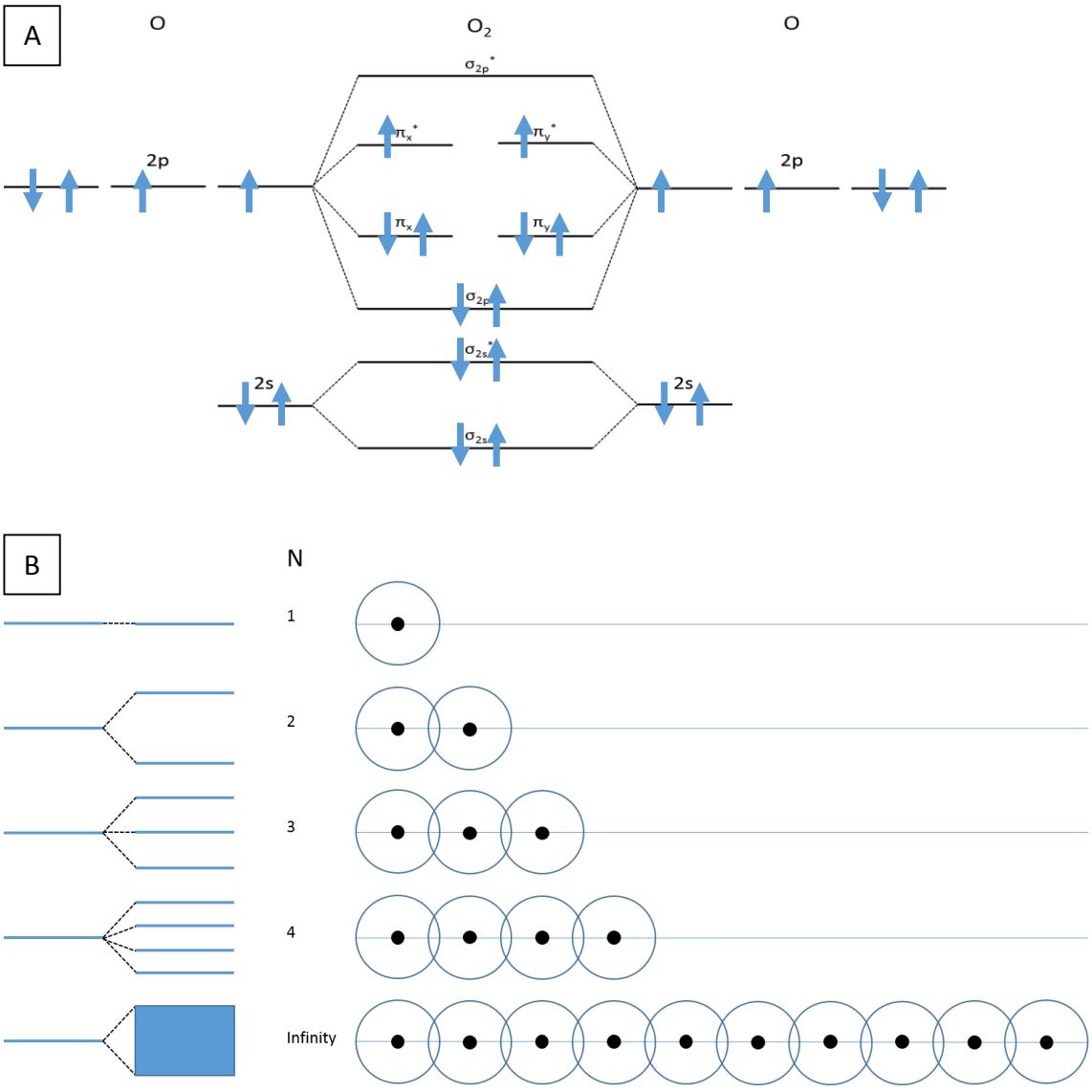

Figure 1.4: A. A schematic showing the overlay of two sets of the 2s and 2p atomic orbitals, in this case from oxygen, to produce the molecular orbitals that define the molecule O_2's electronic structure. B. A schematic showing that many

atomic orbitals can overlap to produce band structure observed in large solid materials as the amount of orbitals (N) moves from 1 to infinity.

This is specific to the material in question and is known as the band structure. Solid materials can thus be classed in three groups dependent upon their band structure -

- **Insulators** exhibit a band gap too large for electrons to cross the bandgap via thermal excitation. Thus they are typically insulating and exhibit low electrical conductivities (Figure 1.5 A).
- **Semiconductors** exhibit a small gap between the valence and conduction band. A band gap is essentially the energy window, which is not occupied by the summation of large numbers of molecular orbitals. Electrons from the valence band (equivalent to the HOMO in a molecule) can cross the bandgap to the conduction band (equivalent to the LUMO in a molecule) upon thermal or photo excitation (Figure 1.5 B).
- **Metals** display no gaps in their continuum of orbitals between the valence and conduction bands. The position of the Fermi level relative to the conduction band ensures metals are conductive (Figure 1.5 C).

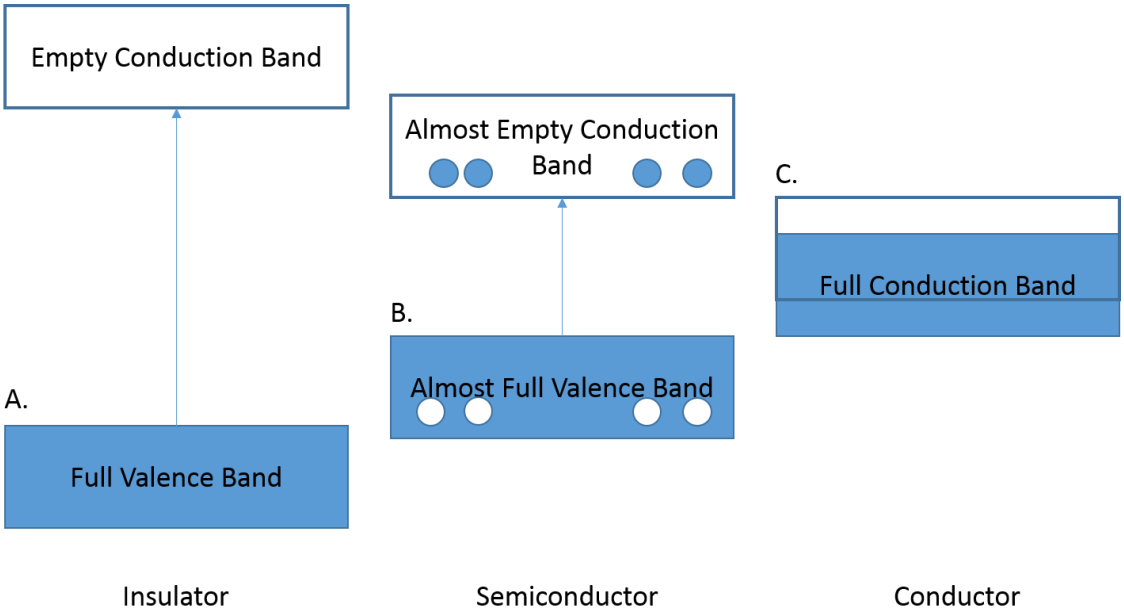

Figure 1.5: A) Insulators exhibit a bandgap too large for light or thermal energy to promote electrons from the valence band to the conduction band. B) Semiconductors exhibit a small band gap between the valence and conduction band, which electrons can be promoted across give sufficient energy via thermal or photonic sources. C) Metals or conductors exhibit overlap of the valence and conduction band, thus electrons are readily available to conduct electricity.

An important feature of band structure is the 'Fermi level' which is a result of Fermi-Dirac statistics. The Pauli Exclusion Principle states that fermions, such as electrons, cannot occupy identical energy states and as such pair up differentiated only by spin and proceed to fill up the empty energy levels sequentially in increasing energy. The Fermi level is the energy at the summit of this set of electrons at absolute zero (Figure 1.6). At temperatures above zero kelvin, such as room temperature (274 K) there exists a distribution of electron energies that span the Fermi level (E_f). Typically electrons can be promoted above the Fermi energy with an input of heat energy, and thus in a metal electrons are capable of conducting as they exist above the Fermi energy into the conduction band. In semiconductors the Fermi energy also plays an important role. In semiconductors the Fermi level exists somewhere between the valence and conduction band, the exact position being dependent upon the material in question and its band

gap value. Thus methods of altering the Fermi level, such as doping, are of significant interest in transparent conducting oxides and photo-catalysts. An un-doped semiconductor is known as an intrinsic semiconductor and with a doped one known as extrinsic. Semiconductors are also classified by the identity of the dominant charge carrier; n type semiconductors are electron dominant whilst p type semiconductors are electron hole dominant.

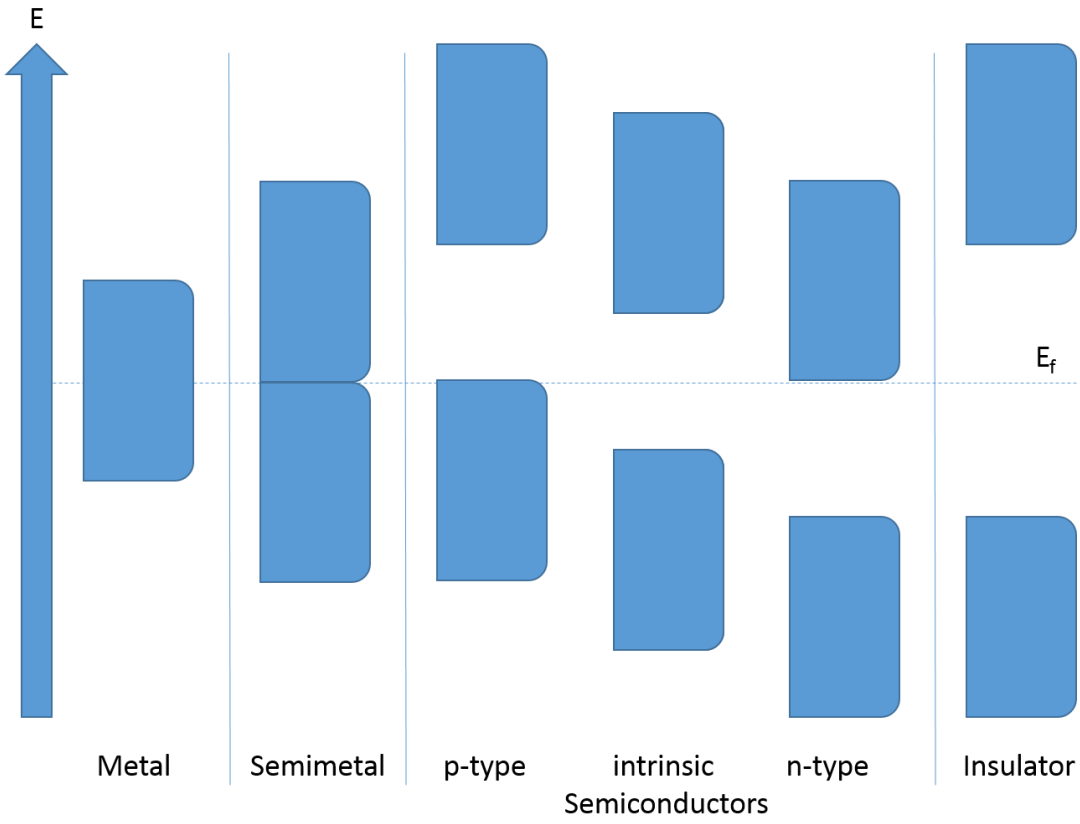

Figure 1.6: A schematic showing the positions of band structure in metals, semiconductors and insulators relative to the Fermi level. As the Fermi level coincides with the band structure of the metal, electrons can contribute to electric current. Semiconductors at zero kelvin have no electrons capable of crossing the band gap, however at room temperature the Fermi level exhibits a range of values and electrons can be found in the conduction band. The position of the Fermi level also dictates whether the semiconductor is n-type or p-type. Semimetals exhibit an overlap between the conduction and valence bands but exhibit negligible density of states at E_F.

1.7 Electrons and Holes as Charge Carriers

Titanium dioxide is able to absorb light in the UVA region of the electromagnetic spectrum as its band gap for the anatase crystal structure is 3.2 eV. The absorption of light allows the promotion of an electron from the valence band to the conduction band leaving in its place an electron 'hole'. The electron and hole can then form an exciton, which is a bound state between the electron and hole, facilitated by the Coulomb force. At room temperature these are then thermalized into separate electrons and holes

The concept of an exciton was first proposed in 1931 by Frenkel.[49,50] Excitons are of interest as they are able to transport energy without transporting net electric charge through condensed matter, particularly in materials where the interaction of electrons between atoms or ions is small compared with the forces holding electrons within atoms or ions, such as ionic solids. This stability is attributed to the interaction of the electron with the hole and the electrons surrounding the hole, which apply a repulsive force, thus stabilising the bound state. As a result an exciton can exhibit lifetimes on the order of microseconds. The bound state is able to move from atom to atom as it progresses through the material, as electric charge is conserved. For semiconductors a model proposed in 1936 was found to better describe the identity of the exciton, known as a 'Mott-Wannier' exciton. The new model accounted for the increased interaction between covalent materials and that the electrons found in the valence band are usually found occupying the gaps between atoms in the form of bonds.[51] It is found that the observed effective radius of a Mott-Wannier exciton can cover tens to hundreds of atomic sites. This is found to be larger in magnitude than traditional 'Frenkel' excitons. As the exciton exists as a bound state consisting of a negatively charged electron and a

similarly charged positive region, it exhibits behaviour similar to that of a hydrogen atom. It can thus be described assuming a constant dielectric by quantum mechanics and is said to be 'hydrogenic' (Equation 1.1).

$E_n = E_{inf} - R/n^2$ (Equation 1.1)

Where E_{inf} is a series constant, R is the Rydberg constant and n is a quantum number.

1.8 Surface Reactions

Once an exciton has reached the phase boundary between a semiconductor, e.g. TiO_2, and whatever medium it is in contact with it is capable of undergoing a wide range of surface redox reactions involving both the electron and hole. These surface reactions are of particular interest in the purification of water. Water will react with the hole of an exciton to produce a hydroxyl radical and in the process of doing so neutralise the hole:

$h^+ + H_2O \rightarrow H^+ + \bullet OH$
$2\ h^+ + 2\ H_2O \rightarrow 2\ H^+ + H_2O_2$
$H_2O_2 \rightarrow HO\bullet + \bullet OH$

The electron can react with dissolved molecular oxygen to form a superoxide ion.

$e^- + O_2 \rightarrow \bullet O_2^-$
$\bullet O_2^- + 2H^+ \rightarrow H_2O_2 + O_2$
$HOOH \rightarrow HO\bullet + \bullet OH$

These two charged species now exist within the water. Energy has thus crossed the boundary between the semiconductor whilst charge within the semiconductor is conserved as the formation of a hydroxyl radical and superoxide ion neutralises the exciton created within the TiO_2. The charged species in the water can now migrate and

react with anything that it comes into contact with. It is these species which are interesting for the use of water purification. Hydroxyl radicals are the second most potent oxidiser found in nature after fluorine, with an oxidative potential of +3.06 V, relative to the standard hydrogen electrode,[52] and superoxide is a potent reducing agent.[53] They can therefore indiscriminately react with carbon-carbon bonds and eventually break them. This process is called mineralisation as the overall products are H_2O, CO_2 and mineral acids. Mineralisation is a well-studied process with the kinetics and thermodynamics featuring in the scientific literature often.[54,55]

It does not matter if the carbon-carbon bonds exist as a bacterial cell wall, outer protein shell of a virus or as carbon-carbon bonds in small organic molecules. The hydroxyl radical is capable of reacting with them all. The kinetic and mechanistic details of hydroxyl radical formation at the TiO_2/ water phase boundary under UV irradiation have been reported on extensively. As such the mechanism of hydroxyl radical and superoxide formation is well understood for a TiO_2 – water interface.

1.9 Semiconductor Photo-catalysis - Titanium Dioxide

One specific semiconductor of interest is titanium dioxide. It has been pursued as a material for use in photo-catalytic applications because of many advantageous properties. These include its low toxicity; which is demonstrated by its prevalent use in commercial food products such as toothpaste, bread and sweets because of its brilliant white colour, its low cost, the depth of technical knowledge already accrued in the scientific literature over the past sixty years, and most importantly its role as a near visible light band gap semiconductor.

1.10 Energy sources

The production of UV Light is energy intensive and without the correct safety equipment can be dangerous. This as a risk is mediated in industry, via shielding and adequate eye protection, but the ability to use visible light wavelengths (400 – 800 nm) present in sunlight to purify water would present a considerable advantage. Visible light is however not harmful to bacteria because it does not cause mutations in DNA helices. A way to combine the freely available energy of the sun (43% of sun's light in visible region) and a material capable of channelling this energy into a medium capable of inactivating bacteria and viruses in water would be highly valuable and this can be achieved through the use of doping of TiO_2 to bring its solar absorption regime into the visible range. This would eliminate the need for energy intensive ultra violet lighting and utilise freely available energy from the sun (Figure 1.7).

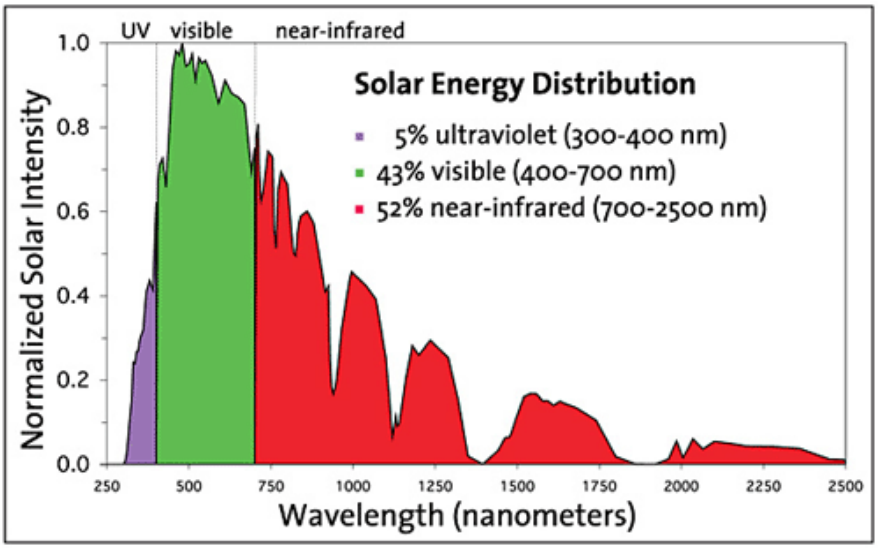

Figure 1.7: The above graph demonstrates the relative intensity and percentage of Visible and UV light present within day to day Solar Irradiation. Image credit: Berkeley Lab Heat Island Group.

1.11 The Ultraviolet Activity of TiO_2 and the role of Dopants

Doping, as explained earlier is a versatile method to engineer a change, depending on the identity of the dopant, to the material's band structure. Whether this is altering the position of the Fermi level or shifting the value of the bandgap permitting it to utilise wavelengths of light which it would normally not interact with.[56] It should be noted that this decrease in the energy of the band gap also makes recombination a more prevalent phenomenon as de-excitation of the promoted electron is a more energetically favourable process. In high dopant concentrations (>2-3%) mixing of orbitals changes the energy of the valence band relative to the conduction band, yielding a change in the band gap energy. This is due to the formation of a coherent Bloch function within the material representative of the new electronic states from the dopants.

In cases where dopant concentration is low (<3%) it is more often found that inter band localised states, formed from oxygen vacancies, exist and the transition seen in the visible region can be attributed to these, with the valence band not changing in energy relative to the conduction band. Hence systems with this doping regime should exhibit increased photo activity in the visible region but also retain their UV photo activity. It should be noted that this is observed for TiO_2 doped with both anionic and cationic dopants, thus it is suggested that the cause for this phenomenon is the creation of oxygen vacancies and the substitution of new electronic states into the existing framework of TiO_2.

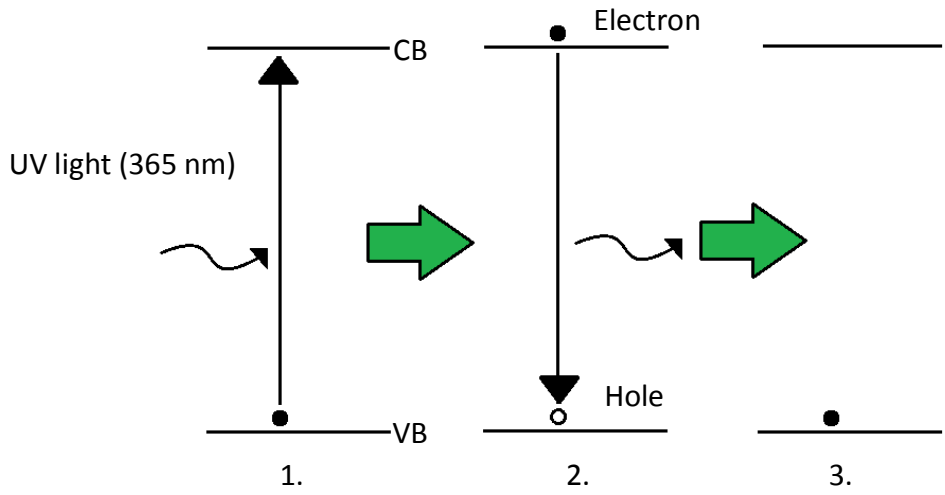

Figure 1.8: 1. Promotion of an Electron to the CB from the VB upon exposure to UV light (365 nm) 2. Recombination of these charged species occurs resulting in re-emission of UV light. 3. The electron is found in the state it started at in the VB and cannot undertake any surface redox reactions.

Recombination limits titanium dioxide's usefulness as an agent for environmental remediation of pollution. Recombination occurs when the photo excited electron in the conduction band de-excites and recombines with the hole created by its promotion into the conduction band (Figure 1.8). Therefore it is vital, if titanium dioxide is ever to live up to its hype of being an environmentally relevant photo-catalyst, to address the issue of this increased possibility of recombination. This can be done in two ways, firstly by using dopants that sequester photo-excited electrons away from electron holes the lifetime of the active species can be extended and overall the rate of electrons and holes performing surface reactions can be increased (Figure 1.9).

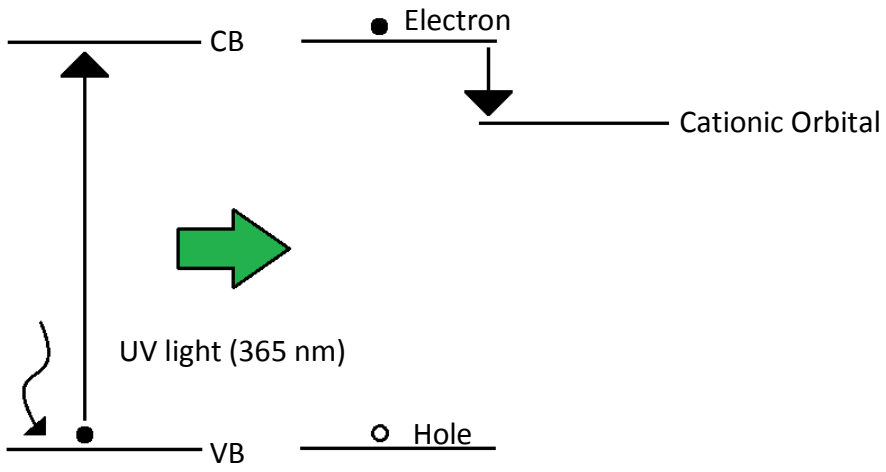

Figure 1.9: Promotion of an electron upon exposure to UV light (365nm), instead of de-exciting back to the valence band the electron is sequestered onto the orbital of a cationic dopant

Therefore this thesis will explore two specific strands of research:

1. The creation of more efficient ultraviolet photo-catalysts by doping or utilising co-catalysts to promote exciton lifetimes
2. The doping of TiO_2 to shift its bandgap towards the visible region of the electromagnetic spectrum to create photo-catalysts that can utilise a higher proportion of energy available from sunlight.

An extensive review of already published literature must be conducted so that the experiments discussed in later chapters can be considered to stand alone in originality, whilst contributing something to literature. Three main approaches are investigated within this body of work:

- TiO_2/ SnO_2 composites
- Nitrogen doped TiO_2
- Nitrogen and niobium co-doped TiO_2

As a result the following review examines these specifically.

1.12 Titanium Dioxide Literature Review

Titanium dioxide has been discussed frequently already in this chapter, however basic physical properties are important in understanding how the techniques used in this thesis will enable the production and synthesis of better functional properties.

Much of the literature regarding TiO_2 concerns two particular crystal structures, rutile and anatase. Rutile is the thermodynamically most favourable structure for TiO_2 to adopt, however at lower temperatures (300 ^oC – 600 ^oC) a metastable crystal structure forms, known as anatase. As a product of the typical synthetic conditions employed in this thesis anatase is the crystal structure of interest. The synthetic method employed is discussed at length in Chapter II.

Titanium dioxide rose to prominence for photo-catalytic applications with the publication of TiO_2's ability to carry out electrochemical water splitting for the production of H_2 by Fujishima *et al* in 1972. This paper, whilst not reporting levels of hydrogen production seen in subsequent reports decades later, was one of the first to show how visible and UV light irradiation may one day be utilised to effect chemical change upon molecules, in this case water for the eventual benefit of mankind.

Hydrogen fuel cells themselves had existed for many years prior to this discovery.[57,58] The classical issue that faced the technology, so that it could be adopted in mainstream society is that producing hydrogen sustainably requires a significant amount of energy and H_2 as a molecule is scare in the atmosphere because, due to its density, leaches from the atmosphere into space. Thus the utilisation of ambient and freely available energy

to drive processes capable of creating H_2 from water became of great interest. Water could now add the accolade of fuel to its roster of important functions.

This research provided the stepping stone to using TiO_2 for photo-catalytic applications for the remediation of environmental pollutants. This connection was first made and summarised by Heller in reporting that solid liquid heterojunctions (composite structures of different materials) formed when semiconductor electrodes placed in solution made a better basis for solar cells for power and H_2 production.[59]

Given that the liquid-solid semiconductor-water interface was now well characterised researchers turned to TiO_2 and the production of hydroxyl radicals to see if these, which exhibit a high oxidative potential, could be used to destroy environmental pollutants. Interest was seeded in 1977 by Frank and Bard in using TiO_2 to remove and destroy cyanide and sulfite ions, themselves common industrial pollutants, from water.[60,61]

Once this was successfully demonstrated this paved the way in subsequent years for many researchers from around the world to explore other inorganic and organic water borne pollutants. Phenols present a serious problem for the environment and often find their way into the environment via phenolic resins used in the production of plywood and in construction and automotive industries. It is also used in the synthesis of BPA whose detrimental effects have been discussed previously. Therefore much time and research has focused on the mineralisation of phenol solutions using irradiated TiO_2. The first report of the photo-assisted decomposition of phenol using TiO_2 comes from Okamoto *et al*.[62] The kinetics of the mineralisation were also reported by Okamoto *et al* shortly after.[63] Since then the mechanism of phenol destruction using photo-generated holes and hydroxyl radicals has become so well understood[64–67] it is now an accepted

standard method for the characterisation of TiO_2 based photo-catalysts.[54,68–71] The decomposition process involves the addition of hydroxyl species at the aromatic carbon sites of the phenol before the breaking of carbon bonds leads to the eventual production of CO_2 and H_2O.

Dyes are another organic based pollutant frequently found in compromised water sources. They originate mostly from textile industries and whilst there exist many technologies capable of combating the issue of removing dye effluent from water sources each have disadvantages, as demonstrated by Robinson *et* al.[72] As governmental regulations around the world start to place higher importance of environmental issues, the quality of liquid industrial effluent is being driven up. The decomposition of dyes is tricky as they exhibit a varied and wide range of chemistries. Thus a non-selective and general route to destroying them is required. As hydroxyl radicals and holes exhibit oxidative potentials high enough to break carbon-carbon bonds[73] decomposition of textile dyes using TiO_2 under UV irradiation has garnered significant interest within the scientific community. The eventual use of TiO_2 in the removal of dyes from water was aided by the publication of the removal of dyes using hydroxyl radicals generated from Fentons reagent.[74] The next logical step involved using UV irradiated TiO_2 in water for the production of hydroxyl radicals. The first report of TiO_2 assisted decomposition of a dye solution came from Vinodgopal *et al.*[75] Since then it has remained a busy niche of research within the TiO_2 community.[52,76–81]

The bactericidal properties of TiO_2, via the photo-catalytic production of hydroxyl radicals have also been investigated. The first instance of this, and an example of particular interest, was reported by Fujishima *et al.* With E. Coli suspensions they

demonstrated that TiO_2 has a bactericidal effect and also removes the endotoxins which can cause bodily harm if ingested or exposed to.[82,83]

In 2000, Fujishima *et al* published a review of TiO_2 summarising the fruits of 30 years' worth of intense research. The field had grown from focusing on the photo-catalytic production of H_2 from water to many applications where electrons and holes were used to create hydroxyl radicals for the destruction of organic contaminants, killing of water borne bacterial agents, viruses, toxins and cyanide to name a few. Self-cleaning surfaces, and anti-fogging surfaces were discussed and featured heavily in the literature.[47]

In many regards, TiO_2 could almost be considered the ideal photo-catalyst. It is cheap to produce, non-toxic (indeed it is found in many household products as a whitener in bread and toothpaste) and easy to handle being a metal oxide. There however existed final hurdles to be conquered before TiO_2 could start being used in the solar power driven environmental remediation strategies discussed by Fujishima *et al*.

1. The bandgap of TiO_2 lies in the ultraviolet region, meaning that the available ambient energy from the sun accounts for only 5-6% of total solar irradiance on any given day, with cloud cover attenuating this further.
2. TiO_2 suffers from efficient recombination processes whereby the photo-generated charge carriers (e^- and h^+) recombine before they, in exciton form, reach the surface and undergo surface redox reactions to effect the desired chemical change.

To combat these problems and enhance the photo-catalytic ability of TiO_2 further strategies were pursued to promote the separation of electron and holes, via doping

and composite materials, so that they recombined less or on slower time scales, allowing larger proportions of excitons to carry out surface redox reactions upon pollutants.

The field started in a new direction to achieve these goals by doping TiO_2 with impurity states to engineer changes in the bandgap towards lower energies congruent with the visible region of the electromagnetic spectrum. This was also investigated so that the charge carrier generation and recombination kinetics might be made more favourable in TiO_2. Heterojunction composite structures involving other metal oxides and metallic substrates were also employed as a mechanism in which electrons could be sequestered from TiO_2 into another material to promote the lifetime of charge carriers.

The work contained within this thesis concerns this particular area of TiO_2 research in exploring and characterising methods to enhance the photo-catalytic ability of TiO_2. First composite TiO_2 / SnO_2 films are explored with the aim of allowing the photo excited electron in TiO_2 to be sequestered into the conduction band of SnO_2. Next nitrogen doped TiO_2, itself a visible light photo-catalyst, is investigated with the hope of providing extra insight into this material of which a lot is already known, however there remain questions still to be answered. Finally N / Nb co-doped TiO_2 is investigated so that optimal doping concentrations may be identified for specific functional properties.

First the literature concerning these respective areas of discourse in the field of engineered TiO_2 must be considered so as not to repeat experiments and also to help identify where the research should head.

1.12.1 TiO_2/SnO_2 Composites

TiO_2 and SnO_2 have co-featured in the literature since 1928 with many studies focusing on the basic physical characteristics of the two metal oxides, such as gas adsorption

studies, XRD measurements and the kinetics of phase separation in these materials.[84–86]

TiO_2 and SnO_2 are both well characterised materials. TiO_2 has received much attention as a photo-catalyst, as previously discussed. SnO_2 has received as much attention but in a different application. SnO_2 exhibits very low energy requirements for the creation of defects and exhibits uncharacteristically low resistivity values for a metal oxide semiconductor. Thus for transparent conducting oxide (TCO) applications it is and has been of significant interest. There has been much work in the literature detailing doping SnO_2 with a wide array of elements to affect its band structure and Fermi level so that resistivity values are low enough to facilitate the conduction of electrons for applications such as flat screen TVs and dye sensitised solar cells.[87,88] Whilst not SnO_2, many industry standards such as Indium tin oxide (ITO) and fluorine doped tin oxide (FTO) are based on tin.[2,89]

Potential applications that TiO_2/ SnO_2 composites may impact upon are wide and varied from photo-catalysis to gas sensing.[90–93] TiO_2/ SnO_2 composites have even been considered a suitable material to act as an electrode for the industrial electrolysis of aluminium.[94]

The use of TiO_2/ SnO_2 composites in photo-catalytic applications was first explored by Vinodgopal *et al* by electrophoto-catalytic studies using an SnO_2 electrode doped with varying levels of TiO_2.[76] It was found that the composite films, which were synthesised by mixing two colloidal solutions of TiO_2 and SnO_2, after application to a conducting membrane and calcination at 673K, were found to exhibit slightly enhanced rates of photo-catalysis compared to pristine TiO_2 and SnO_2 respectively. This was attributed to

enhanced charge separation between the photo-excited electron and the hole generated upon absorption of energy congruent with the bandgap of TiO_2. Specifically the electron was sequestered into the band structure of SnO_2, enhancing the lifetime of the hole so that it can contribute to surface redox reactions for the destruction of an example pollutant, which in this case was an azo dye.

This phenomenon was furthered by Shi *et al* who synthesised ultrafine TiO_2 / SnO_2 composites and measured the photo-catalytic degradation of another azo dye. They corroborated that the TiO_2 / SnO_2 composites exhibited enhanced rates of photo-catalysis compared to pristine TiO_2 and SnO_2.[95]

Since then there have been innumerable reports reporting this advantageous physical characteristic of TiO_2 / SnO_2.

This has been utilised for use in dye sensitised solar cells because of this enhanced charge separation by many authors who report enhanced charge injection and solar efficiencies for such systems.[96–99]

There also exists many reports published within the past 15 years which focus purely on photo-catalytic applications which have successfully destroyed an array of potential pollutants.[100–106]

The work previously published by Ponja *et al* differs from these studies. In previous work performed, TiO_2 and SnO_2 morphologies were joined in a physical sense, with no covalent attachment between them. Ponja *et al* observed a transition from anatase TiO_2 in the bulk to a surface segregated rutile cassiterite SnO_2 structure in a singular material with the two metal oxides covalently bonded to each other. Specifically the TiO_2 phase

exhibited high levels of Sn^{4+} substituting Ti^{4+} within the bulk whilst the SnO_2 layer exhibited a high amount of Ti^{4+} substituting Sn^{4+}. The exact mechanism for the formation of this composite film is unknown. However, that a transition from one metal oxide to another occurs hints at a complex reaction profile. To try and recreate this a combinatorial deposition is explored in Chapter III to recreate the transition from one metal oxide to another across the width of the film.[107] Further insight into the growth of this material is afforded in Chapter IV utilising a new technique, known as time resolved AACVD (TR-AACVD) to create samples which vary as a function of deposition time, allowing changes in elemental ratio, surface morphology and crystal structure to be related to changes in functional properties. This provides insight for the first time into the growth profile of metal oxide materials in AACVD.[108]

1.12.2 Nitrogen Doped Titanium Dioxide

1.12.2.1 Inception

In 2001 Asahi *et al* published work detailing the doping of TiO_2 with nitrogen which heralded a shift in the band gap towards the visible region of the electromagnetic spectrum. This was achieved by sputtering a TiO_2 sample in a nitrogen atmosphere before annealing at 550 ^oC. The films and powders created exhibited a bandgap value between 390-500 nm. This made the photo-catalyst capable of interacting with the majority of solar irradiation the earth receives (390-420 nm). Its ability to carry out visible light induced photo-catalysis for the destruction of MB in solution and gaseous acetaldehyde was documented proving the concept.[109] The nitrogen content was shown to be between 1-1.6% with a mix of substitutional and interstitial doping. This had been identified previously by Saha *et al* whilst characterising surface oxidised titanium nitride

films.[110] The lowering of the bandgap energy is attributed to substitutional nitrogen, whose 2p orbitals mixed with the 2p orbitals of oxygen to form a valence band higher in energy, whilst the conduction band remained unchanged, lessening the energy of the overall bandgap. This was predicted by a joint experimental and computational study published by Morikawa *et al* a month before Asahi's experimental verification of nitrogen doped TiO_2 visible light photo-catalytic properties. In this study the bandgap change that occurs between TiO_2 and oxidised TiN films which represent nitrogen doped TiO_2 was invesitgated.[111] Since these publications two distinct directions within the literature have evolved. The first involves research from an application point of view, demonstrating the possible pollutants nitrogen doped TiO_2 is capable of destroying under visible light irradiation. The second involves probing the facets of nitrogen doped TiO_2 showing how important the role of defects, substitutional and interstitial doping and surface species have upon the observed functional properties of nitrogen doped TiO_2. This aspect of the literature is of particular interest given the work of Cabrera *et al.*[112]

1.12.2.2 Physical characteristics

Because of its ability to absorb lower energy wavelengths congruent with the visible light section of the electromagnetic spectrum nitrogen doped TiO_2 has become one of the most widely explored and characterised materials of the 21st century, a literature search of 'Nitrogen doped TiO_2' yields over 5000 publications since 2001. This fervent attention can be attributed to its ease of synthesis and favourable functional properties for use in visible light photo-catalytic applications. The materials bandgap was first characterised by Akira *et al* when they first published on the subject. Subsequent studies have shown

a range of reported values varying from 2.1 eV to 2.5 eV corroborating this bandgap reduction.[109,112–116]

1.12.2.3 Substitutional

Substitutional doping of nitrogen into a TiO_2 lattice involves the substitution of nitrogen for oxygen within the lattice (Figure 1.10). It can be described using Kroger-Vink notation as N'''_o. Thus the nitrogen takes the place of an oxygen site in the TiO_2 lattice and exhibits a triple negative charge. This is where the property of visible light induced photo-catalysis is hypothesised to originate from. This is because 'Marriot-Wannier' excitons originate from electrons found in covalent bonds.[49] Thus the contribution of 2p orbitals from nitrogen titanium bonds found when nitrogen is substitutionally doped into a TiO_2 lattice should be the source of visible light activity in nitrogen doped TiO_2. This has been confirmed by many researchers within the literature.

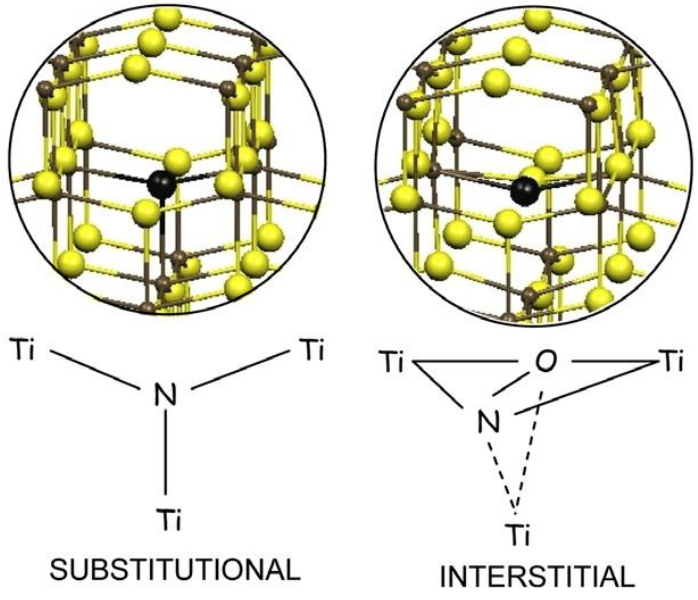

Figure 1.10: Substitutional and Interstitial nitrogen sites in TiO_2. With Substitutional nitrogen the N^{3-} ion occupies an oxygen site. With Interstitial doping N^o occupies the sites between bonding atoms whilst co-ordinating with a lattice oxygen.[115]

1.12.2.4 Interstitial

Nitrogen can also adopt an interstitial position in the TiO_2 lattice. This is where nitrogen sits in the empty space created in between the TiO_2 lattice created by bonding atoms (Figure 1.10). Using Kroger-Vink notation it is described as N'''_i. Many EPR studies show nitrogen dopants that occupy oxygen sites (N_s) and interstitial sites (N_i) to be paramagnetic, meaning they have unpaired electrons. It was originally thought that interstitial nitrogen occupied an identical charge to substitutional nitrogen (3-) and existed as monatomic nitrogen. However over the past ten years the field of theoretical chemistry has shown that nitrogen most likely exists as molecular NO.[117,118] Regarding the charge of the NO species, current thinking, in line with experimental EPR measurements,[115] shows that the NO state exists with a double negative charge, as the oxygen exists as O^{2-} and thus the N exists as N^{o}.[119] There is debate within the literature as to the functional manifestations that the physical presence of interstitial nitrogen in TiO_2 result in. Many claim that nitrogen doping is responsible for an enhanced rate of UV photo-catalysis. Whether this is because of interstitial or substitutional nitrogen is unknown. The role of interstitial nitrogen is hinted at by Sotelo-Vasquez *et al.*[120]

1.12.2.5 Surface species

The role of surface species has been little considered in both visible and UV induced photo-catalysis in nitrogen doped TiO_2, yet it is logical that surface species will strongly dictate and influence perceived rates of photo-catalysis. This has been highlighted by Cabrera *et al* in showing that the perceived rate of ultraviolet induced photo-catalysis in nitrogen doped TiO_2 correlates positively with nitrogen surface species concentrations, which are seen in XPS to reside at ~400 eV.[113,121–123] This nitrogen peak has been

characterised by many as a combination of surface nitrogen intersititial states, NH_x, chemisorbed N_2 and NO species. Given that nitrogen is rarely adsorbed to a surface at room temperature this can be discounted leaving NH_x, NO and interstitial nitrogen. NH_x species are only logical in studies that use ammonia as the nitrogen source so this can be discounted. Thus the position at 400 eV could be considered a mix of NO and interstitial N species. Cabrera *et al* also observed a loss of nitrogen concentration over prolonged periods of UV irradiation. As the nitrogen concentration decreased, so did the rate of UV photo-activity (Figure 1.11).

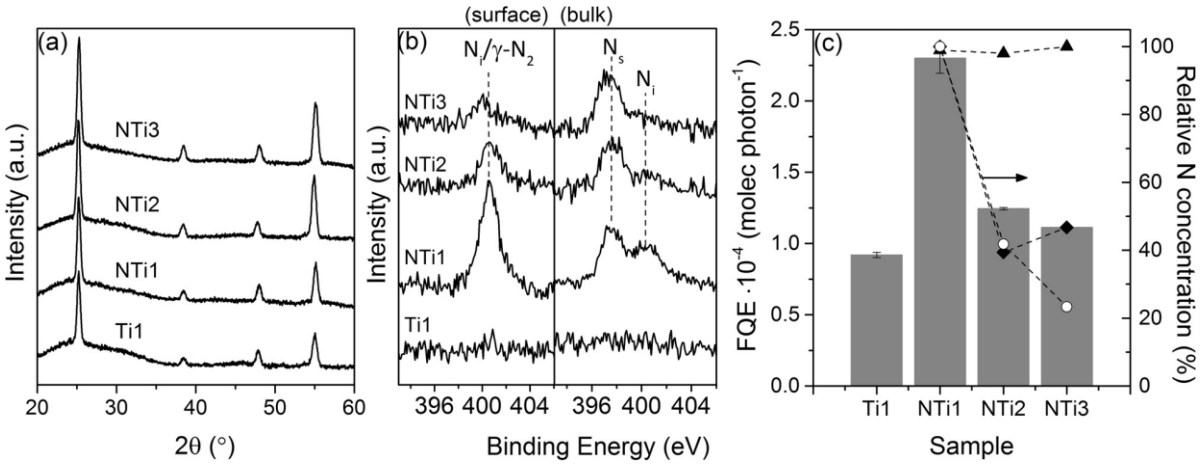

Figure 1.11: a) XRD of nitrogen doped TiO_2 after repeated amounts of irradiation. Little change in crystal structure is observed as a result. b) XPS spectrum of N1s showing how interstitial and substitutional concentrations of nitrogen decrease as a result of prolonged periods of irradiation. c) This is seen to positively correlate with the observed photo-activity for the destruction of stearic acid with lower nitrogen concentrations creating lower rates of photo-catalysis. Once nitrogen concentrations at the surface are seen to all but disappear the rate of photo-activity is seen to roughly equal that of un-doped TiO_2. [112]

1.12.3 Niobium / Nitrogen Co-doped TiO2

Co-doping had been a popular phenomenon within the literature for many years. The concept of co-doping being that a singularly doped photo-catalyst may exhibit a favourable property, such as a shifted bandgap, but lack proficiency in other areas such

as reduced rates of photo-catalysis. By adding a second dopant the deficiency can be overcome. It is also used to instil a multitude of functional properties into the material such as a high photo-catalytic rate and good conductivity.

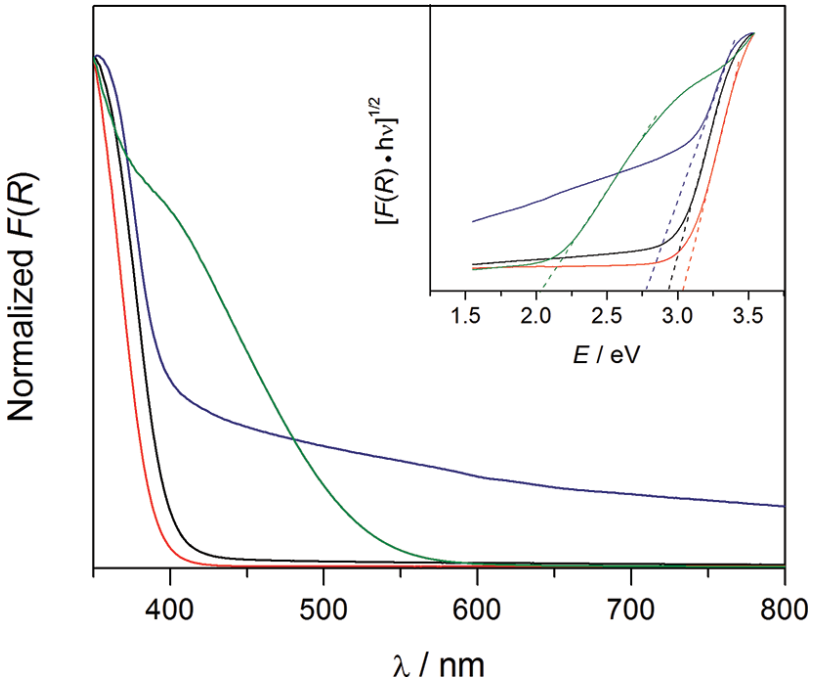

Figure 1.12: diffuse reflectance spectra of TiO_2 (black), TiO_2:Nb (red), TiO_2:N (blue), and TiO_2:(Nb,N)1 (green). Inset: Tauc plots for each compound showing indirect band gaps. Bandgaps are seen to decrease from TiO_2 > TiO_2: Nb > TiO_2: N > TiO_2 (Nb,N).[124]

The first instance in the literature of niobium and nitrogen co-doping in TiO_2 was by Breault *et al* who synthesised nitrogen doped, niobium doped and niobium and nitrogen co-doped TiO_2 and demonstrated that the co-doped powders were more efficient photo-catalysts for the destruction of methylene blue under visible irradiation compared to TiO_2 and the singularly doped N or Nb doped titanium dioxides (Figure 1.12). This enhanced rate of photo-catalysis was determined to originate from the formation of Ti^{3+} and F^- (where F^- represents a colour centre, itself an electron occupying an oxygen vacancy) defect centres which populate states in between the valence and

conduction band of normal TiO_2. To distinguish this they treated created two samples, one which had been synthesised normally and thus contained the original amount of defects. Another sample was created by calcining in oxygen to oxidise Ti^{3+} to Ti^{4+} and repopulate oxygen vacancies. The authors reported a significant drop in the visible light induced rate of photo-catalysis. Thus proving the hypothesis that defect states formed in the process of doping with nitrogen and niobium are responsible for the enhanced rate of visible light photo-catalysis (Figure 1.13).[124]

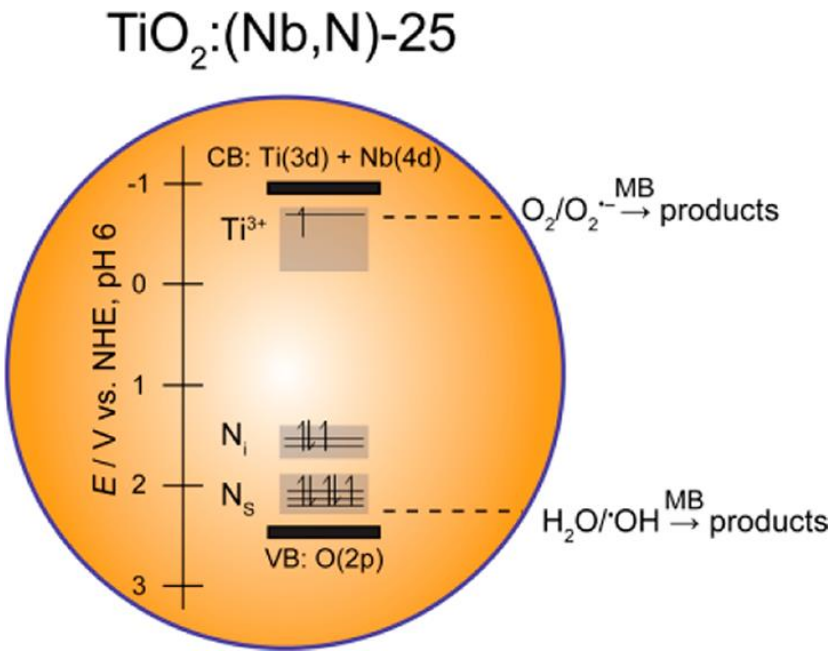

Figure 1.13: Schematic showing the band structure and electron population of nitrogen and niobium doped TiO_2. The schematic also demonstrates how the bandgap band structure is adapted to the production of hydroxyl radicals and superoxide ions for the destruction of pollutants, which in this case is methylene blue. Ti^{3+} states produced by the oxidation of Nb^{4+} to Nb^{5+} and oxygen vacancies in the form of N_i and N_s dopants populate the region in between the valence and conduction band providing energy transitions congruent with visible light.[125]

Further work was done by Breault *et al* in order to characterise the importance of Nb and N concentration in determining the rate of methylene blue destruction in

solution.[125] This was done by increasing the amount of niobium relative to nitrogen in the co-doped powders. The authors reported that increasing the amount of niobium within the co-doped powders yielded an increase in photo-catalytic rate. Interestingly the incorporation of substitutional nitrogen increasing proportionally with increasing niobium incorporation. Thus the niobium increases the solubility of substitutional nitrogen within a TiO_2 matrix. This is attributed to N^{3-} compensating for the introduction of excess positive charges by Nb^{5+} incorporation instead of Ti^{4+}. The authors also identified that N/ Nb co-doped TiO_2 could be used as potential water oxidation photo-catalyst clearing the way for further work within the literature. Since then there have been several reports documenting nitrogen and niobium co-doped TiO_2's favourable visible light based applications.[126]

Nitrogen and niobium co-doped TiO_2 has received little attention compared to their respective singularly doped counterparts and other co-doped titanium dioxides. Nitrogen doped TiO_2 has received much attention over a period of almost 15 years, as discussed previously. Likewise niobium doped TiO_2 has received much attention for transparent conducting oxide applications. This is due to Nb^{4+} oxidising to Nb^{5+} in the process of substituting Ti^{4+} in the lattice and forming Ti^{3+} and contributing electrons to the Fermi level. Thus a higher proportion of electrons at room temperature are present in the conduction band. This changes TiO_2s resistivity from the mega ohm region to the ohm region, achieving a drop in resistivity six orders of magnitude lower.[127]

The relationship between niobium doping and the phase of TiO_2 observed has been an area of intense research because rutile and anatase exhibit differing bandgaps, by understanding the underlying guiding principles, the engineering of specific bandgaps

can be achieved in niobium doped TiO_2's. Arbiol *et al* undertook extensive investigative work into the role of both niobium content and grain size on the anatase to rutile phase transformation that occurs upon heating.[128] Originally this was done with the design of better gas sensors in mind, the study however provides key insights in the physical characteristics of niobium doped TiO_2. It is found that low concentrations of niobium inhibit the phase transition and that grain size also plays an important part in determining the rate and temperature at which the phase transition occurs. They found that the inclusion of niobium in the TiO_2 lattice as a substitutional dopant is found to delay the onset of the anatase rutile transformation as niobium concentration increases. The highest concentration of doping investigated (24.5%) was found to shift the temperature at which each polymorph represents 50% of the whole material by ~150 ^oC from 700 ^oC to ~850 ^oC. This work provides insight crucial to the design of TiO_2 based materials which exhibit a desired crystal phase for functional properties.

Niobium doped TiO_2 has been characterised extensively with XPS being a particularly good method for providing unequivocal identification of the Nb^{5+} dopant state in TiO_2.[129] The Nb^{5+} state has been discussed previously as the reason that conductivity in Nb doped TiO_2 is seen to increase. This was first identified by Furubayashi *et al* in synthesising Nb doped TiO_2 thin films synthesised by Pulsed Layer Deposition (PLD) typically 40 nm thick.[130] The conductivity of these films was found to be comparable to industry standards such as ITO ($In_{2-x}Sn_xO_3$) and ZnO making Nb-TiO_2 a competitive TCO material [131–134]

Because of these favourable conductivity properties Nb-TiO_2 has been investigated extensively as an electron injection medium for dye sensitised solar cells,[135] first

proposed by Grätzel *et al*.[1] because of Nb-TiO_2's ability to efficiently carry and conduct charge it is of interest in multifunctional materials, that is materials which are capable of fulfilling roles in different functional applications, such as gas sensing, photo-catalysis or as a TCO.[127,136–138]

Work done by Emeline *et al* demonstrated that Nb doped TiO_2 for use in photo-catalytic applications suffers as a result of the presence of Nb in TiO_2 photo-electrochemical electrodes.[138] It was found that as Nb concentration increased photo-activity, specifically photocurrent, was seen to decrease (Figure 1.14). Doping levels as low as $Ti_{1-x}Nb_xO_2$ where x = 0.1 was seen to significantly decrease the photocurrent. This was attributed to Nb^{5+} centres acting as recombination centres, thus lessening the lifetime of exciton charge carriers. Another consideration is that higher levels of Nb^{5+} doping are seen to shift the bandgap upwards in energy, thus utilisation of energy congruent with the bandgap of lesser doped Nb-TiO_2's is utilised less.

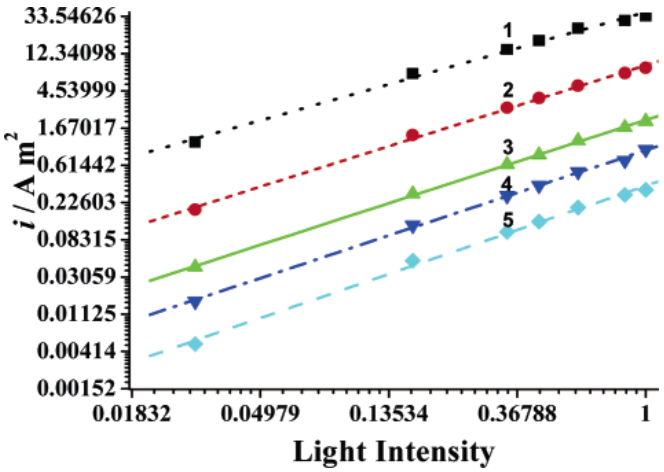

Figure 1.14: At a specific light intensity samples exhibit varying levels of photocurrent (i/ A m²). The dependencies of stationary photocurrent on light intensity (relative intensity for a 150W Xe laser) for $Ti_{1-x}Nb_xO_2$ grown on LAO electrodes is shown for the following Nb ratios: (1) x = 0; (2) x = 0.01; (3) x = 0.03; (4) x = 0.06; and (5) x = 0.1 at 0.5 V applied voltage. It is observed that as Nb content increases photocurrent is seen to decrease. Thus high Nb concentrations decrease photo-catalytic activity. [138]

This is an important consideration when making multifunctional materials such as N/Nb doped TiO_2. As discussed previously increasing nitrogen content is seen to confer favourable photo-catalytic properties upon TiO_2, both in the ultraviolet and visible region of the electromagnetic spectrum. That niobium concentration correlates inversely with photo-activity but positively with TCO properties insinuates that there is a compromise which must be reached where sufficient levels of Nb are present to not hinder photo-activity whilst imbuing favourable TCO properties. Concurrently, nitrogen levels must be high enough to counteract any possible reduction in photo-activity that Nb doping may incur. In Chapter VI this relationship is explored using a combinatorial deposition regime in aerosol assisted chemical vapour deposition (AACVD)[107,139–146] to create a film which graduates from N-doped TiO_2 through to Nb doped TiO_2 with the creation of N/Nb doped TiO_2 materials in between. The intention being to relate changes in physical characteristics such as surface morphology and elemental composition to changes in functional properties such as TCO properties and photo-activity.

2 Chapter II: Methods

The work described in this thesis was achieved via a variety of synthetic and characterisation methods. This chapter provides an overview of these methods.

2.1 Synthetic Methods:

Many variants on aerosol assisted chemical vapour deposition (AACVD) are used in this thesis for the production of TiO_2 based materials. By altering the deposition process insight into the growth process of the doped TiO_2 films grown can be achieved that allows changes in crystal structure, composition and the functional properties that arise from those changes to be mapped and understood. This is proposed to be important as AACVD garners increasing industrial support, as mechanisms for creating materials which can be tailored towards specific applications will become highly sought after.

2.1.1 Aerosol Assisted Chemical Vapour Deposition (AACVD)

Aerosol Assisted Chemical Vapour Deposition (AACVD) relies on the solvation of a precursor in a suitable solvent, the solution is subsequently aerosolised and passed under an inert gas flow into a deposition chamber (Figure 2.1). The deposition chamber is heated up to a maximum of 600 ^{o}C via an electronic control box. The method conveys the advantage of an increased range of available precursors for thin film growth, compared to conventional CVD techniques, which are often limited by requiring precursors that exhibit a vapour pressure low enough so that a gas or vapour can be created upon heating. In AACVD as long as the precursor can be dissolved in a suitable solvent, it is suitable for deposition. This has facilitated the use of titanium alkoxides as precursors for the growth of TiO_2 thin films. As such they form an integral part of all depositions reported in this body of work.[147]

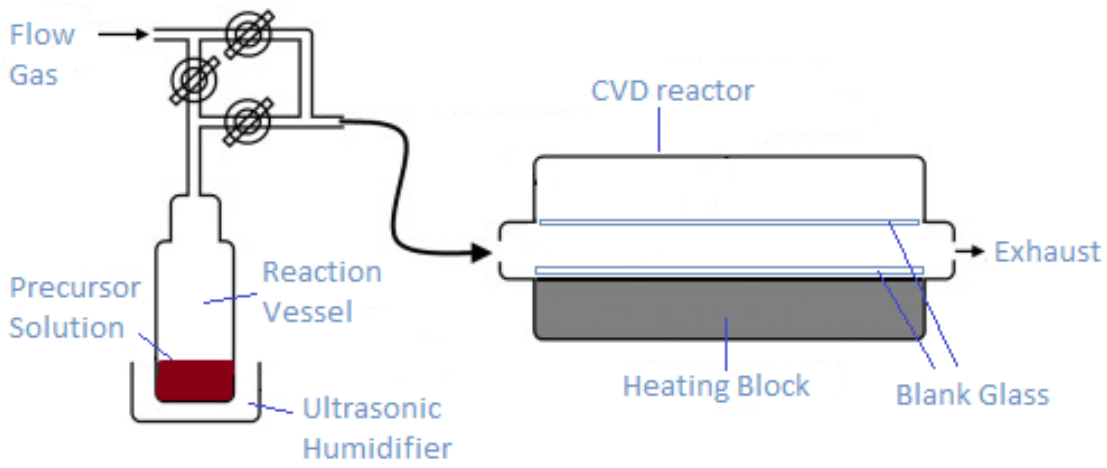

Figure 2.1: A typical AACVD setup. A solution containing the desired precursor is aerosolised and passed into the CVD reactor via inert gas flow. There are two planes of glass which ensure laminar flow so that the deposition process is even upon the glass surface.

The degradation pathway of the precursor is important. The aerosol droplet can undergo homogeneous or heterogeneous reactions in the process of deposition and this can affect the overall morphology of the resultant film.[148] In a homogeneous reaction the aerosol droplet evaporates and the precursor undergoes gas phase degradation which results in nucleation in the gas phase before the precursor has had a chance to reach the substrate surface. This results in the production of fine particulate matter which range from the nm to µm range in size. These particles can either move to the substrate surface and become incorporated into the film, which results in highly porous films, or form powders which line the sides of the reactor. This deposition regime is usually a result of depositing at higher temperatures than necessary. In heterogeneous reactions the aerosol droplet evaporates and the precursor migrates to the substrate surface and undergoes the process of degradation. This results in the synthesis of dense films.

There also exist many variables which can affect the growth of the film:

- Flow rate of the carrier gas – The rate of aerosol movement into the deposition chamber can determine the coverage and quality of the film, it can also have a large impact on the morphology of the material formed.
- Solvent – The solvent, under inert gas conditions can act as an oxygen source or a reducing agent. Thus it can exert a large effect upon the outcome of the film. Its evaporation temperature can also determine whether the precursor follows a heterogeneous or homogeneous pathway.
- The precursor – As the precursor undergoes a degradation pathway specific to its structure the inherent chemical structure can itself affect the film formed.
- Deposition temperature – As temperature increases evaporation of the aerosol droplet before it hits the surface of the glass substrate is more likely to occur. Cooler temperatures thus tend to facilitate one pathway over another. Higher temperature is also associated with a higher degree of crystallinity in the final product, although this depends on the material itself as materials crystallise at different temperatures.

2.1.2 Combinatorial Aerosol Assisted Chemical Vapour Deposition (C-AACVD)

Combinatorial AACVD is a variant of AACVD which allows the creation of many individual samples in a single deposition.[149] It involves the use of two separate precursor streams which only mix within the deposition chamber. Thus a graduated film is created which changes from one material to another gradually across the width of the film, perpendicular to the direction of the aerosol source (Figure 2.2).

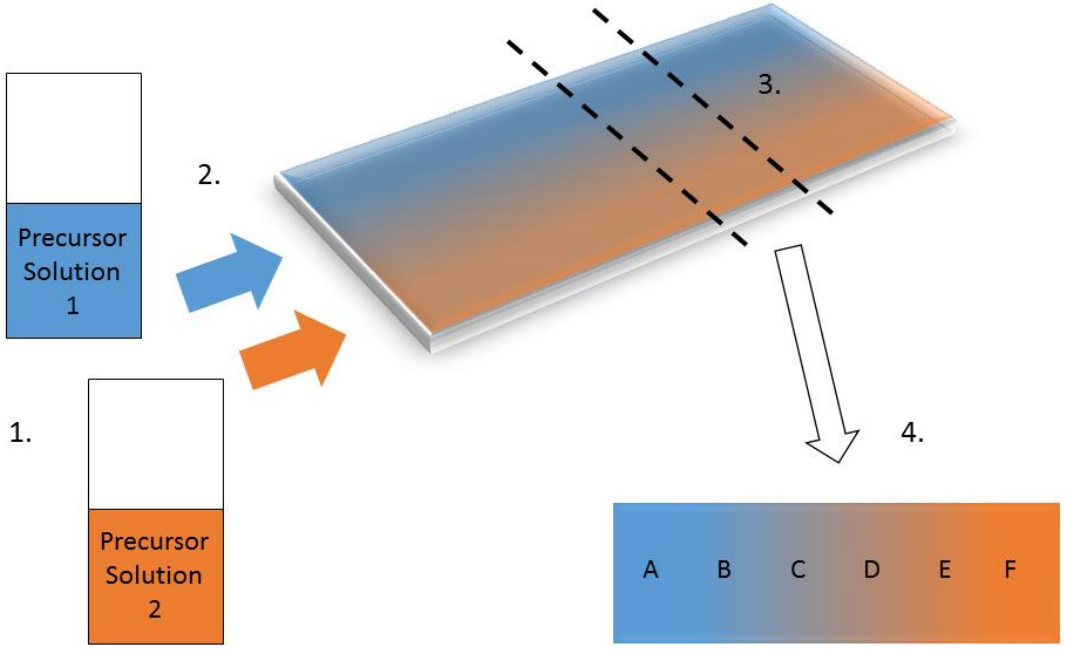

Figure 2.2: Two different precursors for the growth of two different oxides are dissolved (1.). The solutions are aerosolised and passed into the deposition chamber and only mix when in the chamber (2.) whereby a film is created which graduates from one material to another across its width (3.). A grid can be applied so that each position can be characterised and thus the gradual change in composition can be mapped. Each grid position represents a material with a specific level of doping thus the method is excellent at creating several doped oxides at once (4.).

This permits the mapping of changes in crystallinity, elemental composition and morphology with concurrent changes in functional properties which is of great interest for the fine tuning and optimisation of materials for use in a variety of applications.[139,140,144]

2.1.3 Time-Resolved Aerosol Assisted Chemical Vapour Deposition (TR-AACVD)

Time resolved AACVD (TR-AACVD) is a new variant of AACVD which allows the growth profile of a thin film to be mapped as a function of time.[108] Thus changes in crystallinity, elemental composition and resultant functional properties can be charted as a function of deposition time. The technique is capable of generating up to eight samples, which

represent eight individual depositions, in a single deposition thus also saving time in the process of mapping changes in film formation as a result of time. The convention in traditional AACVD is to exhaust the aerosol source before ending the deposition process, resulting in a single film. This does not allow for analysis of the deposition process itself. In doped materials and composites this is important as it may allow fine tuning of the material itself toward a specific application. By creating samples representing differing deposition times the change in film formation can thus be mapped. The optimal conditions for growth can then be elucidated and applied for the growth of a material tailored specifically to an application (Figure 2.3).

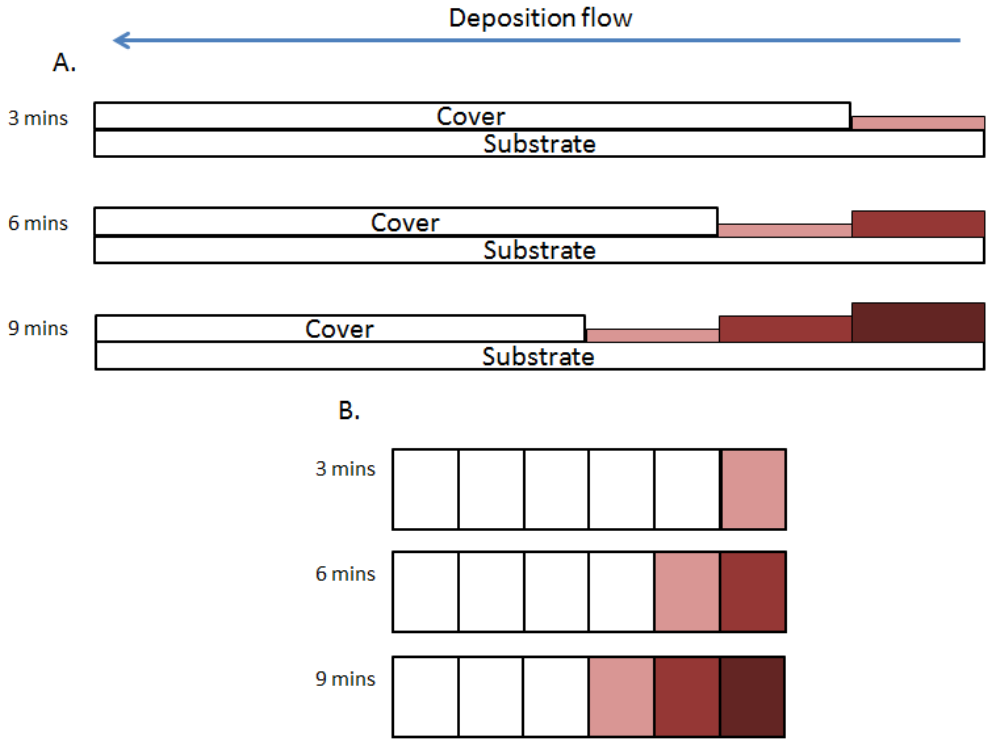

Figure 2.3: A. a schematic demonstrating how time resolved AACVD is carried out. For a deposition of 9 minutes in total a cover initially exposes a small area of the deposition substrate. After 3 minutes the cover is retracted a specific distance to reveal a fresh un-deposited area of substrate. This process is repeated until the deposition process is finished. As time progresses the thin film in each region develop at the same rate but differing times. The films are seen to increase in thickness and deepen in colour to represent this B. A top down view of the resultant films showing how they develop over time. As the colour red darkens the film is more developed. The final product is a film with distinct areas representing differing deposition times on a single substrate. The changes in crystal structure, elemental composition and functional properties between these regions can be mapped and mechanistic understanding of the deposition process obtained as a result.

2.2 Characterisation Methods:

A variety of characterisation techniques have been used in this body of work to track and quantify many differing aspects of the films produced whilst also providing complementary evidence on which analysis is carried out.

2.2.1 X-ray Diffraction (XRD)

X-ray Diffraction (XRD) is a process for analysing the crystallinity of a material. The process involves the irradiation of the sample with an X-ray source of specific energy and wavelength with the subsequent detection of the interference pattern this produces. The general technique is shown in Figure 2.4 along with a sample XRD pattern.

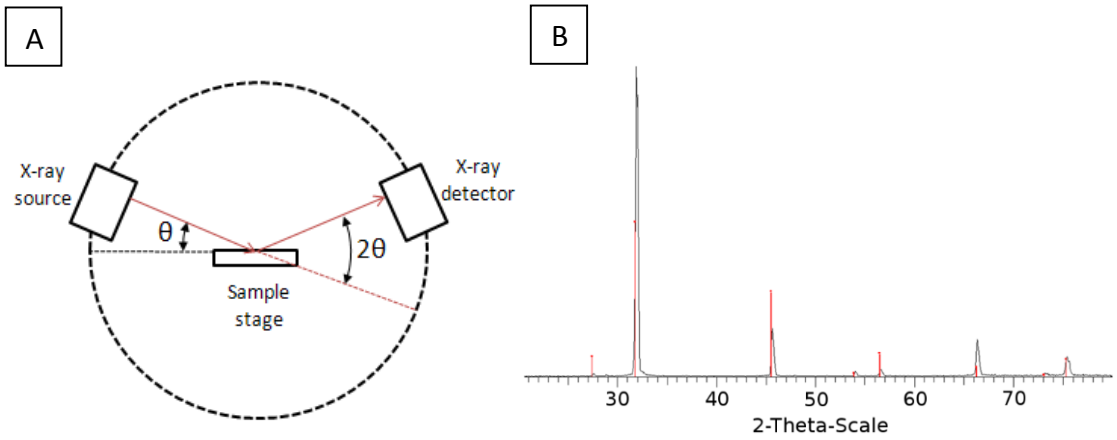

Figure 2.4: A. Schematic showing the general technique by which XRD is carried out. An X-ray source at a specific angle Θ irradiates a sample with X-rays of specific energy. The sample interacts with the incident X-rays which results in diffraction of the x-rays at particular angles (2Θ). B. This can be plotted as a diffraction pattern. A sample XRD pattern is shown above for NaCl which exhibits a rock salt structure. Images taken from http://chemwiki.ucdavis.edu/Analytical_Chemistry/Instrumental_Analysis/Diffraction/Powder_X-ray_Diffraction and [150]

The origin of the diffraction pattern is a result of the wavelength of the X-rays being smaller than the distance between atoms, and dependent upon the spacing between rows of atoms within the crystal, the diffracted X-rays can constructively and destructively interfere with each other upon interaction with the sample (Figure 2.5).[151,152] This interference is dependent upon the crystal structure of the material and as such constructive interference will only occur at angles specific to the material as this is a product of the orientation and prevalence of atoms relative to each other.

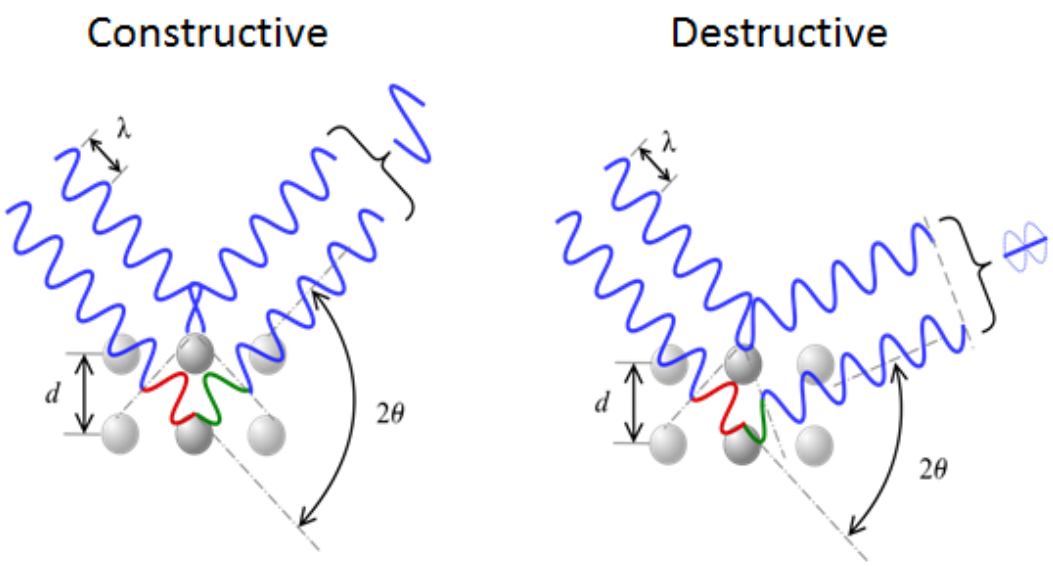

Figure 2.5: Schematic showing the process of diffraction of an incident X-ray and the role that atomic orientation plays in creating constructive and destructive interference of the incident X-ray. Only constructive interference is measured and as such a signal will show at specific 2Θ values. It is this process by which crystal identity and structure can be elucidated, as each material has a different crystal structure which produces a specific set of constructive interferences at differing 2Θ values. Schematic taken from http://www.ammrf.org.au/myscope/xrd/background/concepts/diffraction/.

The process of X-ray diffraction within a crystal obeys the Bragg law (equation 2.1).

$$n\lambda = 2d \sin\Theta \qquad \text{(equation 2.1)}$$

where n is an integer, λ is the wavelength of the incident X-rays, d is the spacing between the atoms which amounts to constructive interference and Θ is the angle between the incident ray and the scattering planes.

2.2.2 X-ray Photoelectron Spectroscopy (XPS)

X-ray Photoelectron Spectroscopy is a technique which allows analysis of elemental oxidation state and elemental composition of a sample. It relies on the process of photon or electron emission from surface elements following irradiation with X-rays of

a specific wavelength (Figure 2.6). This known as the photoelectric effect, which was explained by Albert Einstein in 1905 and was subsequently awarded the Nobel prize in 1921 for his work.[153] The resulting electrons or photons have a specific kinetic energy which is used to identify the oxidation state and element in question. This results from the specific electronic configuration of the electrons within the atom (1s, 2s, 2p, 3s, 3p, 3d, etc.)[154] thus, giving a mechanism for distinguishing between elements. The energy of the X-ray source is kept constant and the difference between the input of energy and the kinetic energy of the emitted electrons determines the energy absorbed by the atoms at the surface of the sample, thus providing the binding energy and identifying both the element itself and its oxidation state by comparison with previous data (Equation 2.2). The binding energy values are plotted as a function of intensity across a wide range of possible values.

$$\mathbf{BE = h\upsilon - KE} \quad \text{(Equation 2.2)}$$

Where BE is the binding energy, hυ is the energy of the incident X-rays and KE is the kinetic energy of the electrons detected after irradiation with the X-ray source.

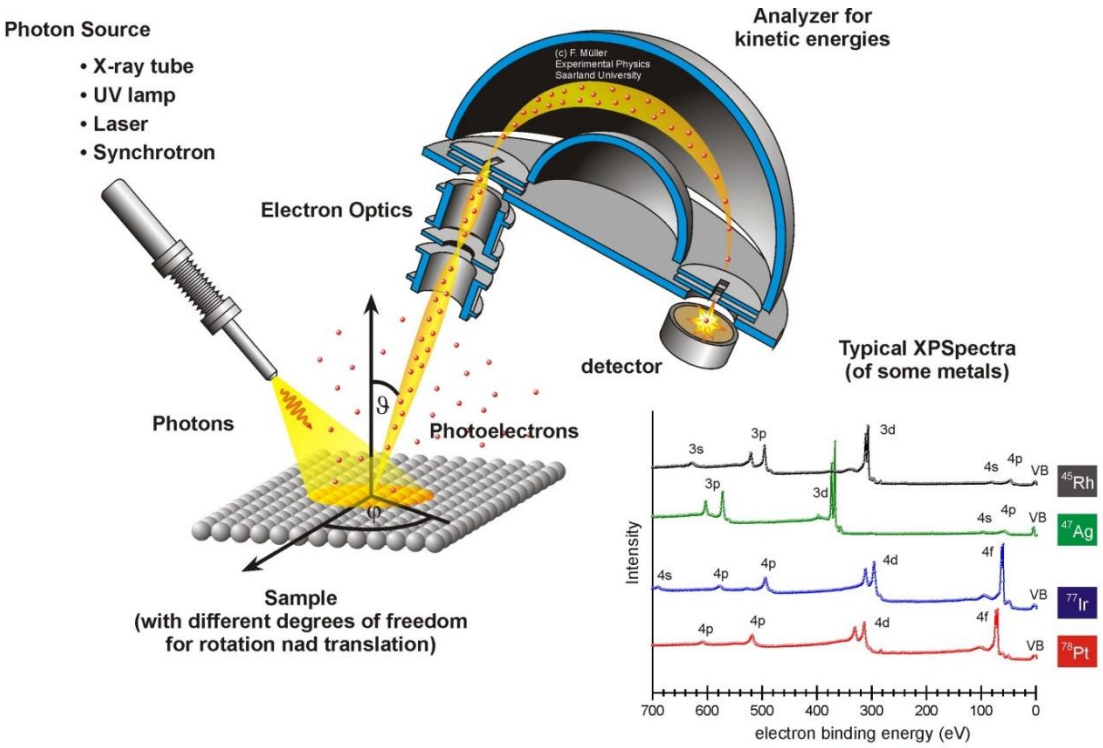

Figure 2.6: A typical XPS setup demonstrating the process of sample irradiation with an X-ray photon source, creation of photoelectrons of differing energies and the subsequent detection of the electrons, the intensity of the photoelectrons is plotted as a function of binding energy. The binding energy gives information on the identity of the elements present and their oxidation state, whilst comparison of the intensity between two peaks can give information on relative elemental composition. Image taken from http://jacobs.physik.uni-saarland.de/english/instrumentation/uhvl.htm.

XPS is a surface sensitive technique with information available about the first 20 nm of depth of the sample. It can also be used to probe the bulk of a material by coupling with an electron beam which sputters down through the sample for a specified time or distance and then taking scans of the resulting surface. By this, changes in oxidation state and elemental composition can be mapped as focus transitions from the surface through to the bulk. It is therefore a powerful technique for understanding how changes in elemental structure may affect functional properties.

2.2.3 Scanning Electron Microscopy (SEM)

Scanning Electron Microscopy (SEM) is a microscopy technique that can be used to probe surface morphology with a resolution of up to 1 nm. It is used to image a variety of things from nanomaterials to insects and pollen grains.[155,156] It is also therefore a relevant technique for thin film characterisation because morphology plays an important role in functional properties. The physical principle involves subjecting the sample to an electron beam and measuring secondary electrons emitted upon exposure to the electron beam. This comes in many forms such as secondary electrons, back scattered electrons and X-rays (Figure 2.7). The signals measured originate from atoms at the surface of the specimen, and due to a narrow electron beam the images obtained have a large depth of field, which provides information about the 3D structure of the specimen in question. This therefore provides useful information about the structure and morphology of the sample.[157]

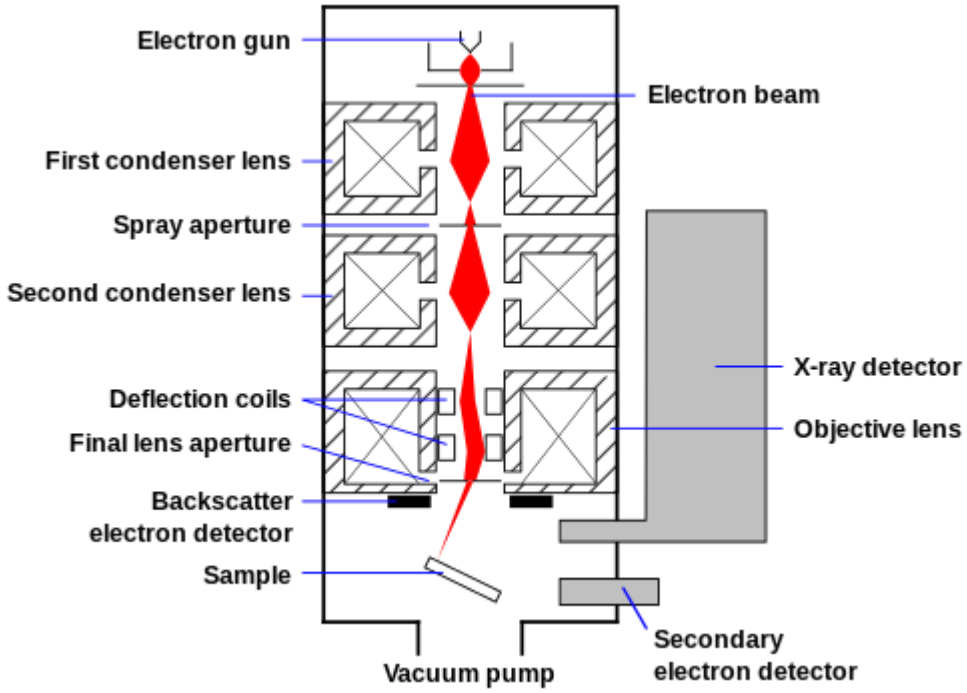

Figure 2.7: A typical SEM setup showing the exposure of samples to a narrow electron beam and the subsequent generation of secondary electrons which are used to create an image of the sample. Image used under a creative commons license. Image taken from https://commons.wikimedia.org/wiki/File:Schema_MEB_(en).svg

2.2.4 Ultraviolet-Visible Transmission Spectroscopy (UV/Vis)

Ultraviolet – Visible transmission spectroscopy is a spectroscopic method which probes the absorption, transmission and reflection properties of thin films in the ultraviolet-visible region of the electromagnetic spectrum. The method measures the difference in the input signal and the signal that is measured upon transmission through the thin film as the probe signal scans from the near Infrared to the ultraviolet region (1500 – 250 nm). The method is useful for the determination of transmission, for use in window coatings, the determination of thin film thickness via the swanepoel method[158] and the calculation of bandgaps using tauc plots.[159] Tauc plots involves the plotting of photon energy (eV) against the square (indirect transition) or square root (direct transition) of

the absorption coefficient of a material at that particular photon energy. The steepest part of the graph is extrapolated to the baseline to infer the bandgap of the material.

2.2.5 Transient Absorption Spectroscopy (TAS)

Transient absorption spectroscopy is an advanced spectroscopic method capable of charting the lifetime of excitons and free charge carriers in semiconductors and a wide range of other materials.[160–163] Upon exposure to irradiation of the correct energy, electrons can be excited from the valence band to the conduction band generating a photo-electron and an electron hole. Once formed the electron and hole form a separate entity within the semiconductor matrix known as an exciton, which displays molecular characteristics. As a result it displays a HOMO and LUMO. The lifetime of these states can be measured using a pump-probe method and plotted to provide the exciton lifetime co-efficient. The process of the pump probe methodology is explained in Figure 2.8.

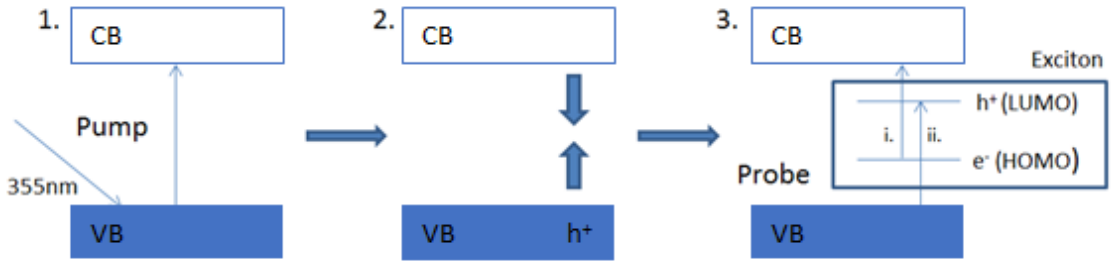

Figure 2.8: A Schematic demonstrating the pump probe method in which TAS is carried out. 1. The material is subjected to a probe laser at energy of 355nm which lasts 6ns. 2 The formation of a photoelectron and hole results in the conduction and valence band. 3. The exciton forms and takes on molecular structure and a HOMO and LUMO results. A probe laser at specific wavelengths is used to probe the lifetime of the electron and hole that forms the exciton.

After probing at several different wavelengths a graph of lifetime against wavelength can be plotted and the role of electrons and holes can be measured by resolving the

peak area as two Gaussian peaks which represents each charged species. The rate of decay of these two constituents over time is plotted to determine the lifetime co-efficients of the electron and hole.

2.2.6 Resazurin Ink Test

The resazurin Ink test is a method for quantitatively measuring the photo-catalytic rate of a material. The method involves the application of an ink by spray coating and the subsequent irradiation of the sample. The dye contains resazurin which is reduced by a glycerol intermediate (itself a constituent of the ink), which acts as a relay for surface electrons which originate from the material as a result of irradiation, to resorufin, which is pink (Figure 2.9). The contrast from resazurin, which exhibits a royal blue colour can be charted by UV/Vis and as such the samples are irradiated for a set amount of time, the change in UV/Vis measured and the process is repeated. The kinetics of resazurin destruction, and thus the overall photo-catalytic rate can be inferred and calculated by plotting the data as a function of time. In concordance with formal quantum yield and formal quantum efficiency these data can then be put into context.

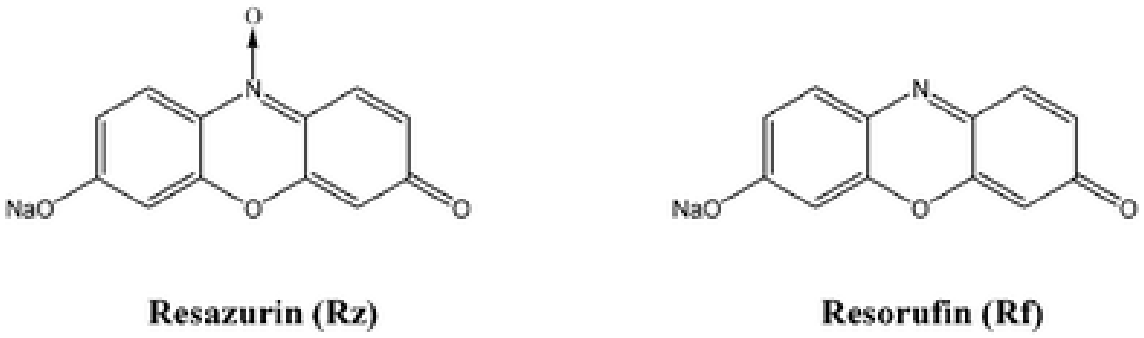

Figure 2.9: A schematic showing the difference between resazurin and its reduced form resorufin. This is accompanied by a change in colour from a royal blue (resazurin) to pink (resorufin). This change can quantitatively be charted via simple transmission UV/Visible spectroscopy.[149]

2.2.7 Stearic Acid

Stearic Acid is another method for the quantification of a material's photo-catalytic rate. The preparation of the sample pre irradiation involves dip coating the sample into a stock solution of stearic acid in chloroform (0.05 M) at a specific rate (120 cm/ min). This ensures that the layer of stearic acid deposited after the chloroform evaporates is always of the same thickness. The samples are measured via Infrared spectroscopy and irradiated for a set amount of time. The IR spectrum for stearic acid is repeated and the difference allows the photo-catalytic rate to be inferred through calculation of the change in area under the peaks associated with stearic acid.[164]

2.2.8 Water Contact Angles

Water contact angles give an idea as to whether a surface exhibits hydrophilicity or hydrophobicity. These are important functional properties which can determine whether a material will excel at cleaning water or windows etc. Photo induced wettability testing measures the difference in water contact angle after irradiation. The contact angle itself is the angle between the droplet and the substrate (Figure 2.10).

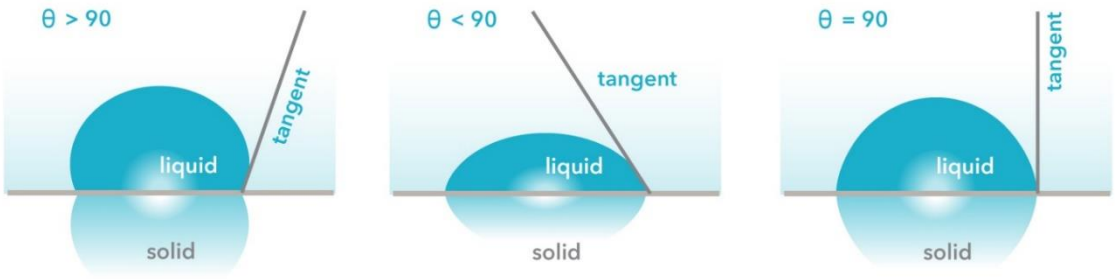

Figure 2.10: Schematic showing the water contact angle ranges for a variety of liquid droplets that result as an interaction with a solid flat surface. Image taken from http://www.biolinscientific.com/attension/applications/.

A specific set of apparatus is used to drop a water droplet of specific volume (3 µl) onto the surface in a controlled way, utilising a high definition camera, images and videos can be captured that allow the analysis of the water contact angles of the droplets to be calculated using analysis software.

2.2.9 Resistivity Measurements

Resistivity measurements give an indication into the conductivity of a material. The lower the resistivity the better the material is as a transparent conducting oxide. The four point probe method for measuring resistivity in semiconductors employs two outer probes which pass current through the sample, which induces a voltage between the two inner probes (Figure 2.11). Using Equation 2.3 the sheet resistivity can then be calculated.[165,166]

$$\rho_{\square}\left(\frac{\Omega}{\square}\right) = \frac{\pi}{ln\,(2)}\frac{V}{I} \qquad \text{(Equation 2.3)}$$

Where:

$$\frac{\pi}{ln2} = 4.53$$

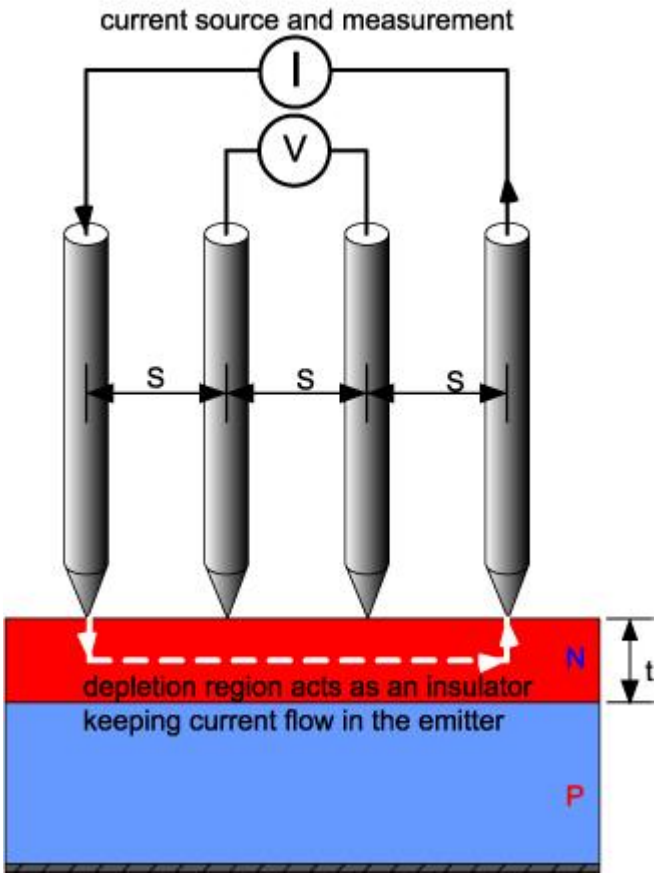

Figure 2.11: A typical Four point probe setup for the measuring the sheet resistivity of a semiconductor. Current is passed through the outer probes, which induces a voltage in the inner probes. Utilising the resulting voltage and current values the sheet resistivity can then be calculated. Image taken from http://pveducation.org/pvcdrom/characterisation/four-point-probe-resistivity-measurements.

Two point resistivity measurements are collected using a multi-meter connected to two conductive needles. The needles are placed in contact with the surface and the reading recorded. Many factors can affect the readings given using this method, such as distance between the probe needles, which can vary. Once accounted for however the method allows for quick data collection and subsequent identification of areas of low resistivity.

2.2.10 Hall Effect Measurements

Hall Effect measurements were made to ascertain levels of resistivity and charge carrier concentration and mobility. The Hall Effect was first documented by Edwin Hall in 1879.

Specifically it is the observation of a voltage difference transverse to electrical current and perpendicular to an external magnetic field. The voltage difference depends upon the nature of the charge carriers, which in doped semiconductors involves hole and electrons. Square 1 cm^2 coupons where prepared and placed into a calibrated external magnetic field of 0.58 T with a transverse input current of 1 mA. From this, sheet resistance, charge carrier concentration and charge carrier mobility was calculated. These are important metrics for evaluating the materials ability to be used in TCO applications.

3 Chapter III: Combinatorial Aerosol Assisted Chemical Vapour Deposition of a Photo-Catalytic Mixed SnO_2/ TiO_2 Thin Film

3.1 Introduction

Previous work in the Carmalt group described the synthesis of a highly photo-catalytic, hydrophobic TiO_2 and SnO_2 composite thin film via AACVD.[167] This involved the mixing of titanium (IV) isopropoxide and tin (IV) butyl trichloride in a single bubbler in ethyl acetate. Photo-catalysis was found to be enhanced compared to an industry standard, Pilkington Activ^{TM}, by an order of magnitude. The composite exhibits surface segregation of SnO_2 relative to the bulk which was found to be TiO_2 dominant whilst exhibiting relatively extreme levels of doping (~60%) within the bulk. It was hypothesised that surface cassiterite SnO_2 acted as an electron sink for photo-generated electrons created in titanium dioxide hence promoting the lifetime of electron holes. Therefore the natural formation of a metal oxide heterojunction was observed which created a synergism between TiO_2 and SnO_2 resulting in enhanced photo-activity compared to TiO_2 and SnO_2 separately. The novel microstructure and change in water contact angles after UV irradiation is demonstrated in Figure 3.1 (a-e).

Prisitine anatase TiO_2 (f) and cassiterite SnO_2 (g) morphology is also demonstrated in Figure 3.1 showing the drastic difference between the morphology of these three films. The monolithic morphology of the TiO_2/SnO_2 composite is also hypothesised to contribute to the increased rate of photo-catalysis.

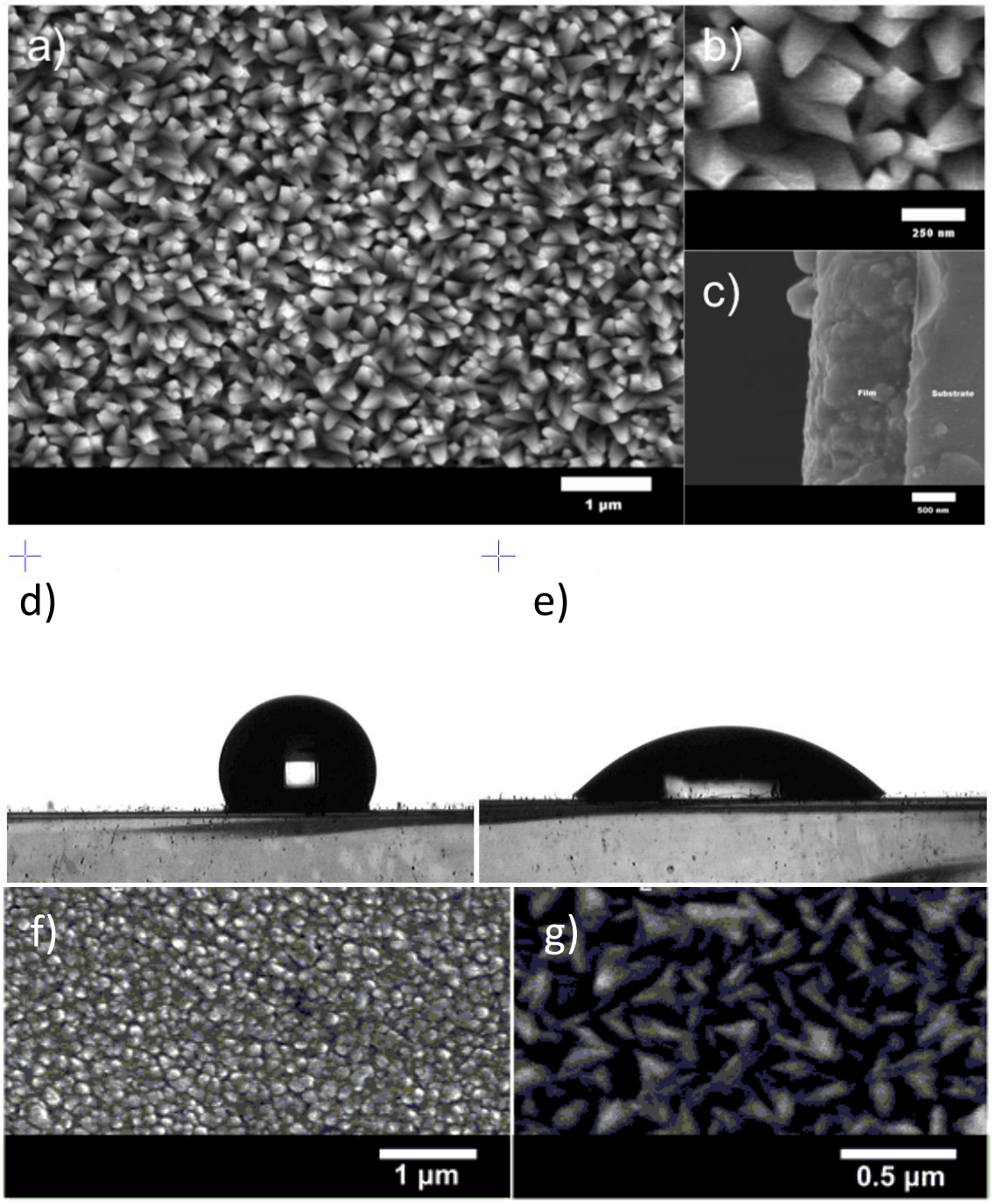

Figure 3.1: a) the overall novel microstructure exhibited by the TiO_2/SnO_2 composite film first grown by Ponja et al. b) a close up of the microstructure showing the square pyramidal growths. c) Side on SEM demonstrating the thickness of the film. d) the water contact angle for the composite film pre UV irradiation e) the water contact angle for the composite film post UV irradiation.[167] *f-g) shows standard TiO_2 and SnO_2 morphology respectively.*

The novel formation of a heterojunction system, which manifests simply as a product of a materials synthesis, without prior design of such a system is therefore of interest. By

understanding this process new ways to create advanced functional materials may be achieved.

A way to further probe the mechanism of growth of this composite is therefore of significant interest. Whilst characterisation techniques may elucidate and quantify the overall layout and structure of the film it cannot provide mechanistic information about the materials formation. Combinatorial aerosol assisted chemical vapour deposition (C-AACVD) is a relatively new and novel form of AACVD which conveys many advantages in this area. By conducting the deposition in a combinatorial manner, which involves mixing two independent precursor steams within the reactor itself, a film of graded composition can be conveniently grown. This allows investigation of differences in microstructure, crystal structure and any resultant functional properties that occur as a result of changes in dopant concentration, relative to the host material, across the width and length of the film.[146]

To thus try to understand the key reasons for this observed synergism a C-AACVD study was undertaken to grow a film which transitions from TiO_2 to SnO_2 across its width and in turn the composition, with the intention of reproducing the composite material first grown by Ponja *et al* whilst also providing mechanistic insight into the growth of the film.[167]

3.2 Experimental

3.2.1 Thin film Preparation using AACVD

Nitrogen (99.99%) (BOC) was used as supplied. Depositions were obtained on SiO_2 coated float-glass. Prior to use the glass substrates were cleaned using water, isopropanol and acetone and dried in air. Glass substrates of ca. 90 mm x 45 mm x 4 mm

were used. The precursors, titanium (IV) tetra-iso-propoxide (99%) and tin (IV) butyl tri-chloride (99%) were obtained from Sigma-Aldrich Chemical Co. and used as supplied. Aerosols were generated in ethyl acetate (99%) and carried into the reactor in a stream of nitrogen gas through a brass baffle to obtain a laminar flow. A graphite block, containing a Whatmann cartridge heater, was used to heat the glass substrate. The temperature of the substrate was monitored using a Pt–Rh thermocouple. Depositions were carried out by heating the horizontal bed reactor to the required temperature of 450 ^{o}C before diverting the nitrogen line through the aerosol and hence to the reactor. The total time for the deposition process took between 20 and 25 minutes. At the end of the deposition, under the nitrogen flow, the glass substrate was left to cool to room temperature with the graphite block before it was removed. To synthesise the combinatorial TiO_2/ SnO_2 film titanium tetra-iso-propoxide (0.5 g) was dissolved in ethyl acetate (20 ml) and added to a flask. In a separate flask was added tin butyl trichloride (0.5 g) dissolved in ethyl acetate (20 ml) and the separate flasks connected to a split nitrogen line with the aerosol feed leading from the individual flasks to a specially constructed baffle ensuring mixing of titanium and tin precursors happened in the reactor under nitrogen flow. AACVD was carried out at 450 ^{o}C until both aerosol solutions were exhausted; effort was made to, by eye, match the intensity of the aerosol so that this happened at roughly the same time.

3.2.2 Sample Characterisation

X-ray diffraction (XRD) was carried out using a Lynx-Eye Bruker X-ray diffractometer with a mono-chromated Cu Kα (1.5406 Å) source. X-ray photoelectron spectroscopy (XPS) was carried out using a Thermo Scientific K-Alpha instrument with monochromatic Al-Kα source to identify the oxidation state and chemical constituents. High resolution

scans were done for the Ti (3d), Sn (3d), O (1s) and C (1s) at a pass energy of 40 eV. The peaks were modelled using Casa XPS software with binding energies adjusted to adventitious carbon (284.5 eV). SEM images were taken on a JEOL JSM-6301F Field Emission instrument with acceleration voltage of 5 kV. Images were captured using SEMAfore software. Samples were cut into coupons representing the locations on the grid and coated with a fine layer of gold to avoid charging. The optical transmission was measured over 350–1500 nm range using a Lamda 950 UV/Vis spectrometer.

3.2.3 Functional Property Testing

Photo-catalytic activity was assessed using an established method based on a resazurin 'intelligent ink' first developed by Mills *et al.* [168] Photo induced wettability was tested by placing the samples under a UVC lamp for 2 hours then measuring the water contact angle by placing a 5 µL droplet onto the surface of the films. The film was then irradiated overnight for 16 hours and water contact angles were re-measured. Water droplet contact angles were measured using a First Ten angstroms 1000 device with a side mounted rapid fire camera after casting a 5 µL droplet from a fixed height onto the surface. To assess the photo-catalytic activity of the film at sites marked at specific grid positions the whole sample was first washed with water, rinsed with isopropanol and irradiated for 30 minutes to clean and activate the sample. A resazurin based ink was then evenly applied using a spray gun and the photo-induced degradation of the resazurin ink monitored by scanning whole images of the film and calculating the photo-activity by measuring the change in the red component of the pixels of the scanned images at specific grid positions. Formal quantum efficiency and the formal quantum yield was then calculated. Formal quantum efficiency was calculated by dividing the rate of dye molecules destroyed per s per cm^2 by the photon flux (4.53×10^{14} photons per

cm^2 per s). The formal quantum yield (FQY) was calculated by dividing the rate of dye molecules destroyed per s per cm^2 by the number of photons absorbed by the films. The photon flux and photon absorption for each film was determined using a UVX digital radiometer with a detector for 365 nm radiation attached.

3.2.4 Preparation of 'intelligent ink' solution

Glycerol (99.6%), hydroxy ethyl cellulose [average Mv ¼ 90 000], Resazurin (92%) were all purchased from Sigma-Aldrich Chemical Co. and used as supplied. The 'intelligent' ink consisted of Resazurin (40 mg) redox dye in an aqueous solution (40 mL) with glycerol (3 g) and hydroxylethyl cellulose (0.45 g) that was aged for 24 hours at 3–5 ^{0}C. The solution was mixed thoroughly before use.

3.3 Results

A mixed phase TiO_2/ SnO_2 thin film was grown by C-AACVD. The film was achieved by the deposition of titanium dioxide and tin dioxide in ethyl acetate, which acted both as an oxygen source and a carrier medium, using different flasks ensuring that mixing of the two separate aerosol precursor streams occurred only once inside the reactor. The purpose of this was to provide a film whose composition graduated from pure SnO_2 to mixed SnO_2/ TiO_2 phases in the middle through to pure TiO_2 on the other side. The film was then characterised by a range of physical techniques including XRD, XPS, SEM, EDX and UV-Vis spectroscopy. A 4 x 5 grid was overlaid on the film to quantise and define specific positions on the film which allowed the mapping of the entire film, shown in Figure 3.2. Functional property testing, specifically photo-catalysis, water contact angle measurement and resistivity measurements were carried out to map concurrent

changes in functional properties across the film as the composition of TiO_2 and SnO_2 changed across the width and length of the film.

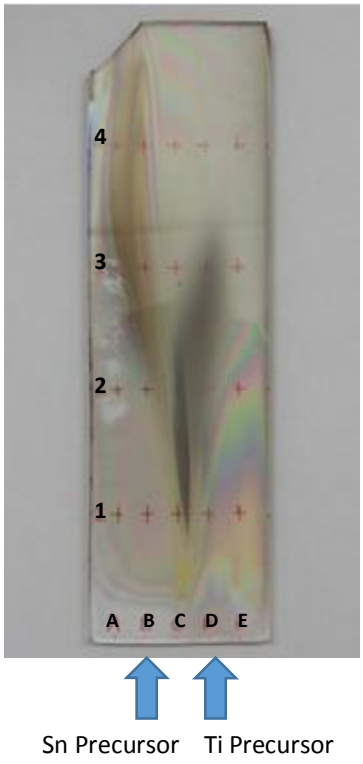

Figure 3.2: The film with grid position over lay. The tin precursor entered the reactor from the left hand side and the titanium precursor from the right hand side where they mixed once in the reactor. A clear divide along the C column shows the boundary that appears to form as a result of this mixing process. Interference patterns either side of the central C column indicate the formation of transparent thin films.

3.3.1 Characterisation

3.3.1.1 X-ray Diffraction (XRD)

X-ray diffraction patterns for all samples were obtained. Diffraction patterns for cassiterite SnO_2 and anatase TiO_2 only were found at all positions on the films with anatase TiO_2 found generally to the right and cassiterite SnO_2 generally to the left of the film. This is expected considering the entry points of the aerosol streams. Upon analysis

of these patterns and their relative positions on the film a selection of individual spots present on the grid, shown in Figure 3.3, were focused on.

The combinatorial nature of the film is evident throughout the rest of the XRD patterns as areas of cassiterite SnO_2 change to anatase TiO_2 from the left of the film to the right of the film, with mixed areas apparent in the central region. Figure 3.3 shows the crystal structure transitions to these composite phases from the tin dioxide and titanium dioxide regions respectively.

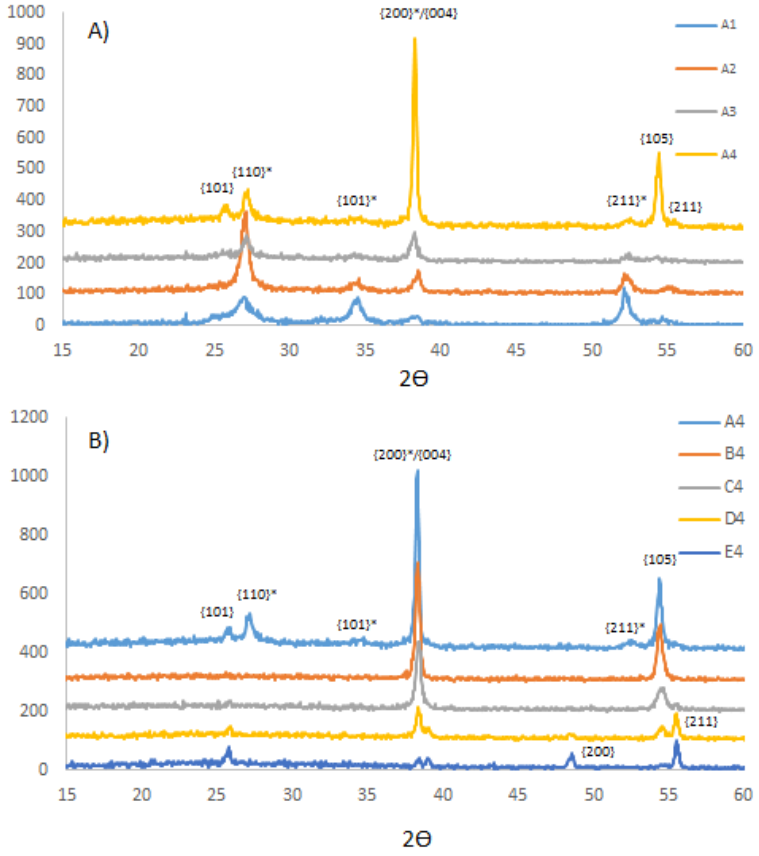

*Figure 3.3: crystal phases denoted * correspond to cassiterite SnO_2 all others are anatase TiO_2. A) Moving from row one to four in column A the phase transitions from cassiterite to a mixed phase. B) As focus changes from left to right along row 4 a transition from the mixed phase to E4 is observed with suspected anatase phases with specific preferred orientation present at the B and C positions, and standard anatase at the D and E positions.*

It became evident that two particular areas of interest existed. Firstly, from A1 through to A4 (Figure 3.3 A), along the length of the film where the tin precursor is introduced into the reactor through to the exhaust, the XRD patterns change from cassiterite SnO_2 to a composite TiO_2/ SnO_2 phase similar to the one reported by Ponja et al.[167] A1 exhibits characteristic {110}, {101}, {200}, {211} and {220} crystal planes associated with cassiterite SnO_2. From A1 through to A4 the {110} and {211} planes are still observed but not the {101}. In addition crystal planes associated with anatase TiO_2, specifically the {101} and {105} planes are then observed. The {200} plane also increases in intensity in A4 compared to A1 and this is thought to be due to overlap with the {004} plane observed in anatase TiO_2 XRD patterns in other grid positions as shown in Figure 3.3 B. The mixed TiO_2/ SnO_2 phases identified as A2 – A4 correlate well with the composite TiO_2/ SnO_2 films previously reported.

The top row of the film from left to right changes from A4 to E4 (as shown in Figure 3.3 B), the XRD pattern changes from the mixed phase described above through to another mixed phase present at B4 and C4 which exhibit the {200} and {105} planes of both cassiterite and anatase respectively. However, It is because these XRD patterns are part of the transition from E4, which is anatase TiO_2, through to A4 that it is hypothesised the {004} anatase plane and the {200} cassiterite plane overlap to give the enhanced intensity of the peak observed in B4 and C4.

A Le Bail refined model was used to model the degree of lattice expansion exhibited by the mixed phase areas found at A4, B4, C4, D4 and E4 respectively shown in Table 3.1. This row was chosen specifically as the composite material reported by Ponja *et al* is

majority TiO_2 with a surface segregated layer of SnO_2. Hence understanding how the crystal structure changes from TiO_2 is of importance.

Table 3.1: Le Bail refinement of XRD patterns for row 4 shows overall an increase in the anatase unit cell volume and the cassiterite unit cell volume concordantly decreases as the film progresses from E4 to A4.

Sample	Dep. Temp./ ^oC	Phase(s)	a/Å	c/Å	Unit cell Volume/$Å^3$	Volume Expansion/ %
TiO_2	-	anatase	3.784	9.514	136.268	-
SnO_2	-	cassiterite	4.738	3.187	71.552	-
A4	450	anatase	3.834	9.413	138.423	1.58
		cassiterite	4.662	3.145	68.366	-4.44
B4	450	anatase	3.782	9.557	136.756	0.35
		cassiterite	4.749	3.180	71.762	0.29
C4	450	anatase	3.775	9.588	136.639	0.25
		cassiterite	4.793	3.144	72.241	0.96
D4	450	anatase	3.769	9.603	136.436	0.12
		cassiterite	4.749	3.183	71.799	0.34
E4	450	anatase	Amorphous			
		cassiterite	Amorphous			

It is evident that overall the anatase unit cell volume increases from position E4 to A4 suggesting a change from standard titanium dioxide to a doped titanium dioxide phase at A4. The cassiterite unit cell volume decreases overall from E4 through to A4 which suggests a transition from cassiterite SnO_2 to tin atoms acting as a dopant within TiO_2. Compared to the previously reported TiO_2/ SnO_2 composite films it appears that A4 exhibits a marked increase in unit cell volume for anatase but, contrastingly, a large decrease in cassiterite unit cell volume (see Table 3.1). This suggests interstitial doping of Sn^{4+} (ionic radii 0.69 Å) into the TiO_2 lattice and substitutional doping of Ti (crystal

radii 0.75 Å) for Sn atoms (crystal radii 0.83 Å) in the SnO_2 lattice causing an increase and decrease in volume respectively.

X-ray diffraction of the grid position immediately next to A4, specifically B4, exhibits a mixed SnO_2/ TiO_2 region with preferred orientation in the {200} and {105} planes for SnO_2 and TiO_2 respectively. Le Bail refinement of this crystal phase shows that the TiO_2 crystal plane {004} overlaps the SnO_2 {200} plane. As attention transitions from B4 to A4 the insertion of the {101} and {110} cassiterite planes can be seen, with the diffraction pattern largely remaining unchanged otherwise in comparison to A4.

3.3.1.2 X-ray Photoelectron Spectroscopy (XPS)

An X-ray Photoelectron Spectroscopy (XPS) depth profiling study was carried out for all 20 grid positions. At each spot a surface scan was taken and then the film sputtered for 100s after which another scan was taken. This process was repeated four times to provide a concentration profile of titanium relative to tin that represented both the surface of the film and the material in the bulk. In this way reproduction of the composite material could be confirmed and the changing elemental ratios that exist across the film could be mapped.

Peaks representing TiO_2 at 458.3 eV (Ti^{4+} $2p_{3/2}$) and 463.9 (Ti^{4+} $2p_{1/2}$) eV were found in all samples. Peaks representing tin match previous literature reports for SnO_2 and are observed at 486.5 eV (Sn^{4+} $3d_{5/2}$) and 494.9 eV (Sn^{4+} $3d_{3/2}$) (Figure 3.4).

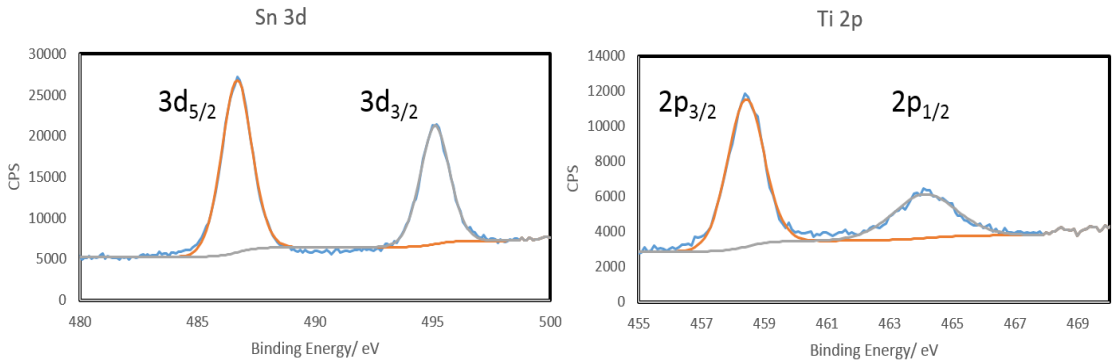

Figure 3.4: Sample tin and titanium XPS spectra showing the peaks characteristic of Sn^{4+} and Ti^{4+} in the TiO_2 / SnO_2 composite material.

The surface was observed to be tin rich at positions lying to the left of the centre of the film (positions A1-2 and B1-2), which is where the tin precursor aerosol enters the reactor as expected (Table 3.2). A similar situation arose to the right of the centre of the film with the surface being titanium rich, as this is where the titanium precursor aerosol enters the reactor as expected. One thing of note is that the A4 position exhibits a slightly lower % Sn compared to its surroundings. Overall the surface is relatively tin rich but the % Sn decreases as focus transitions from left to right across the width of the film, demonstrating again the combinatorial nature of the film.

Table 3.2: %Sn for all grid position from the surface through to 200s of sputtering time.

% Sn Across All Grid Positions					
0 s	**A**	**B**	**C**	**D**	**E**
4	78.69515	87.04548	82.87369	75.77996	83.98906
3	98.43462	91.09069	76.03223	73.11862	74.37096
2	98.81087	94.31136	75.05159	65.09297	51.78369
1	100	100	82.20524	44.47182	39.94859
100 s	**A**	**B**	**C**	**D**	**E**
4	45.00042	30.36635	7.185715	18.65229	20.90817
3	63.72057	64.85189	26.35833	35.27986	28.95965
2	99.62587	97.71658	48.49034	42.34377	21.78533
1	100	100	88.44185	29.64672	14.42356
200 s	**A**	**B**	**C**	**D**	**E**
4	30.10007	11.53568	4.269478	4.604354	6.192926
3	28.4167	41.39982	8.884463	20.19749	8.402891
2	98.43646	93.88356	30.48776	25.14834	7.927608
1	100	100	83.4553	13.96891	8.312611

After 100 s of sputtering (Table 3.2) the left hand side of the film remains tin rich, however positions A4 and B4 now have % Sn < 50 % indicating they are now titanium dominant. Overall the % Sn to the right hand side decreases indicating that Ti^{4+} is more prevalent in the bulk. Anomalously, C4 exhibits, relative to the other grid positions, a relatively low % Sn. Only positions A-C1 and A-B2 exhibit % Sn values > 50 % indicating that the positions which are tin rich in nature decrease as the focus starts to transition towards the bulk. That these positions are immediately next to the entry point of the SnO_2 precursor stream and that they all exhibit cassiterite SnO_2 diffractions patterns is unsurprising.

After 200 s of sputtering the % Sn to the right of centre (columns C-E) continues to decrease relative to the left hand side which remains tin rich in the same positions discussed previously (Table 3.2). The % Sn at positions A4 and B4 continues to decrease,

indicating TiO_2 is now the dominant material within the bulk. Following 300 s of sputtering the % Sn continues to decrease for all grid positions bar A-C1 and A-B2, which still retain % Sn > 50 %. Post 400 s of sputtering the majority of the film exhibits a % Sn of less than 50 % sparing grid positions at A-B1 and A-B2, this is not surprising as these sites are situated in the immediate vicinity of where the tin precursor is introduced into the reactor.

Generally it is apparent that TiO_2 appears to dominate in the bulk but that the surface is tin rich.

3.3.1.3 Energy Dispersive X-ray Spectrscopy (EDX)

To corroborate the elemental ratio observed in XPS, energy dispersive X-ray (EDX) spectroscopy was undertaken to attain values for the relative ratio of titanium to tin found throughout the film at specific grid positions. It was observed that titanium dioxide was the dominant phase throughout the majority of the film except in the immediate vicinity of the entry point of the tin precursor at A1 and B1 (Table 3.3). This corroborates our findings in XPS, in that titanium dioxide is dominant in the bulk in all grid positions sparing those found in the immediate vicinity of where the tin precursor enters the reactor specifically A1 and B1. It is noted that XPS profiled a small portion of all samples and did not profile all the way through the film, which is why there exists a disparity between the dominance of Ti relative to Sn between the methods.

Table 3.3: Surface % Ti for all grid position for EDX measurements.

	A	B	C	D	E
4	81.46	96.88	95.9	100	100
3	39.71	96.21	96.52	100	100
2	7.3	87.09	94.23	100	100
1	1.33	2.07	86.93	100	100

3.3.1.4 Scanning Electron Microscopy (SEM)

Scanning Electron microscopy was undertaken at all grid positions. As surface morphology plays an important role in a materials' observed functional properties, such as photo-catalysis and conductivity, mapping and understanding how morphology changes relative to dopant concentrations is integral.

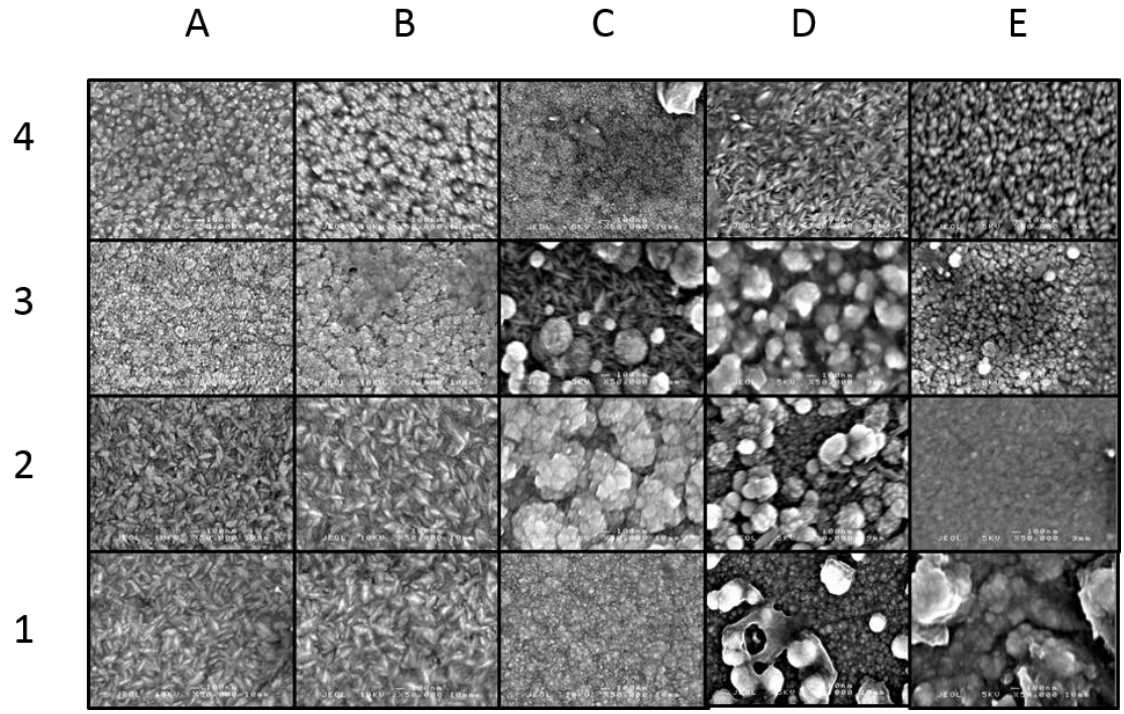

Figure 3.5: A composite image of all 20 SEMs arranged in a grid. Cassiterite morphology is seen in columns A and B and anatase morphology seen in columns D and E, intermediate morphology is seen in column C. Of particular interest is the morphology found at A4 which exhibit monolithic growths.

Figure 3.5 details the changes in surface morphology that occurred across the length and breadth of the entire combinatorial film, using the grid previously mentioned. The expected cassiterite SnO_2 morphology was observed in the correct place (A1-3 and B1-2).[169] Sparing position A4, where the composite XRD pattern was observed the rest of the positions are shown to be anatase TiO_2[170] and exhibit characteristic but varied surface morphologies. Particulates found at C2-3 and D1-3 could be a result of homogenous degradation pathways which result in the gas phase formation of materials before they come into contact with the glass substrate. Focusing specifically on column A and row 4, as discussed specifically in XRD, the transition from the composite TiO_2/ SnO_2 material at position A4 to cassiterite SnO_2 and anatase TiO_2 morphologies, respectively, was evident.

Importantly the morphology seen at position A4 (Figure 3.6) was observed to be identical in nature to that reported by Ponja *et al*.[167] It is therefore evident that the use of combinatorial AACVD to investigate and reproduce a material of interest has been a success thus far.

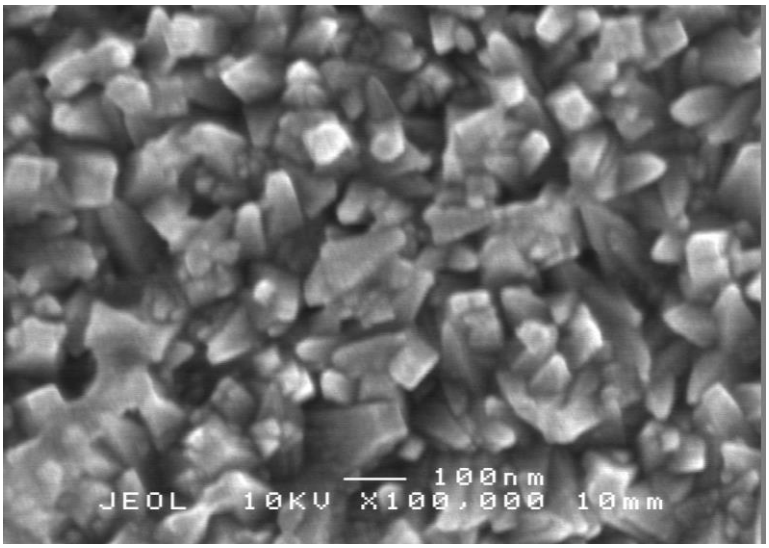

Figure 3.6: A close up of grid position A4 displaying the monolithic nature of the surface morphology

3.3.1.5 UV/Vis Reflectance Data

UV-Visible spectroscopy was carried out at all grid positions and thin film thickness calculated from the data using the Swanepoel method.[158] No overall trend in film thickness can be deduced as a result of the transition from SnO_2 to TiO_2 across the width of the film but all grid positions exhibit film thicknesses between 90-300 nm which are in line with expected values for previously reported thin films of these materials (Table 3.4).[171,172]

Table 3.4: Thin Film Thickness values for all grid positions. Calculated using the Swanepoel method.

	A	**B**	**C**	**D**	**E**
4	287.58	223.12	281.885	118.435	80.13
3	277.625	316.81	191.005	251.2	207.855
2	234.36	252.785	260.46	276.155	248.1
1	235.045	92.93	324.02	259.01	260.75

3.3.1.6 Band Gap

Utilising tauc plots (Figure 3.7 C) (photon energy plotted against a function of the absorption co-efficient) obtained from UV/Vis absorption data band gaps for all positions were calculated to chart changes in bandgap across the film that may result from the formation of the composite or heavily doped phases, identified by XPS. It also acts as another diagnostic tool for identifying areas where cassiterite SnO_2 or anatase TiO_2 is present. Because the (direct) band gap for SnO_2 is 3.6 eV[173] and the (indirect) band gap for TiO_2 is 3.2 eV[174] a difference can be observed to empirically determine and corroborate other analysis techniques in asserting which areas of the film are predominantly SnO_2 and which ones are TiO_2. It can be seen from both indirect (3.12 eV) and direct (3.42 eV) band gap measurements that grid position A4 shows exhibits a band gap lower in energy than its surroundings (Figure 3.7 A-B).

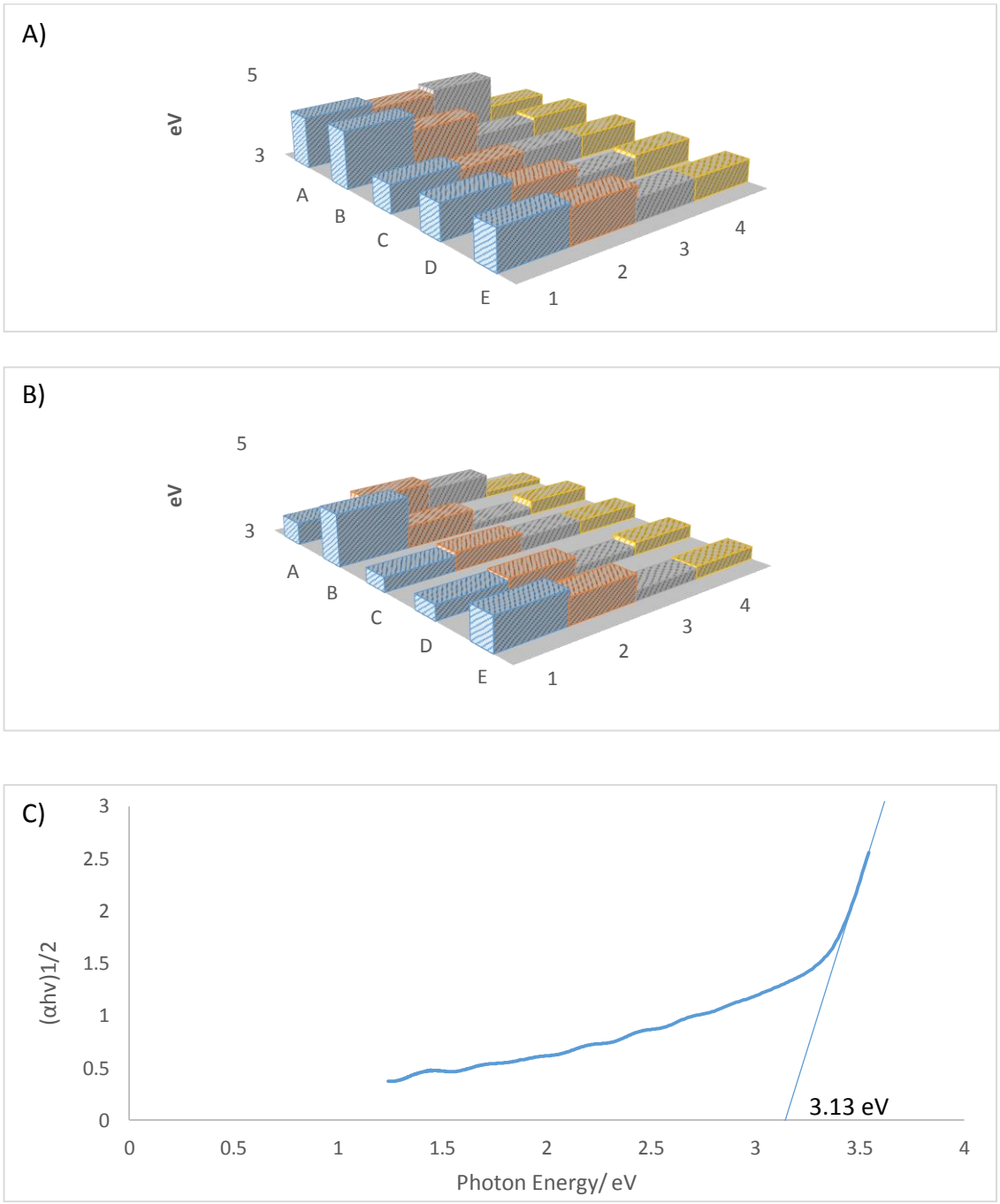

Figure 3.7: A) Direct band gap values for all 20 grid positions. B) Indirect band gap values for all 20 grid positions. Across both plots a band gap decrease is seen at A4 relative to its surroundings. Direct bandgaps are simply from the valence to conduction band and are symmetrically aligned in K space. Indirect bandgaps require a 3 body interaction between a photon, electron and a phonon to counteract the difference in crystal momentum between the valence and conduction band. C) A standard tauc plot demonstrating how bandgaps are extrapolated from absorption coefficients.

3.3.2 Functional testing

3.3.2.1 Photo-catalysis

The combinatorial film was spray coated with an even layer of “Intelligent Ink” first utilised by Mills *et al* to facilitate the quantification of the photo-catalytic rate of all grid positions. The photo-reduction reaction of resazurin (royal blue) to resorufin (pink) was induced by irradiation with UVA light (365 nm, flux = 4.53 x 10^{14} photons per cm^2 per s) and monitored by scanning images of the film throughout the irradiation process at specific time intervals representing different stages in the degradation process. A time-line of the film and the changes induced by increasing levels irradiation is shown in Figure 3.8.

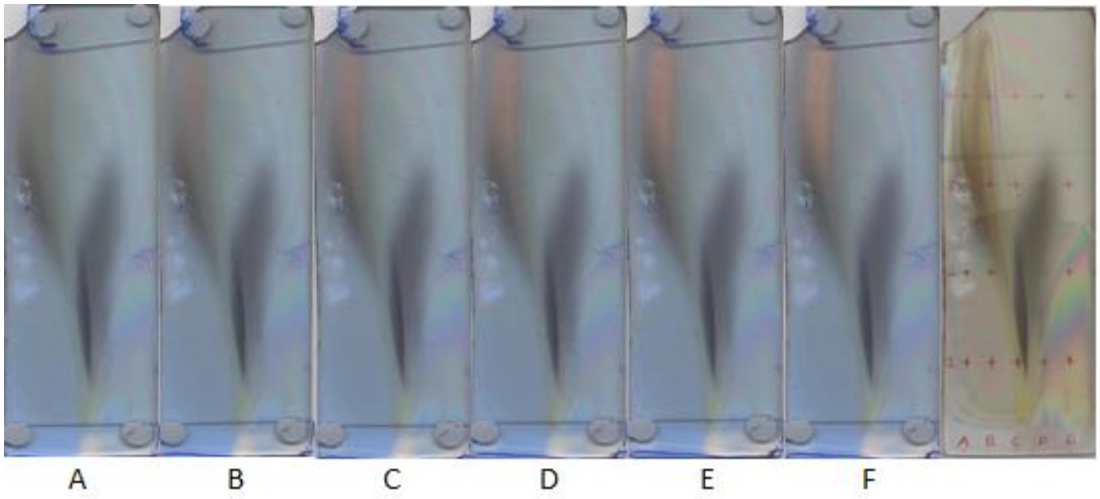

Figure 3.8: Images A, B, C, D, E and F are scans taken at 0, 5, 10, 15, 20 and 35 minutes respectively, only the grid position A4 exhibits any photo-activity of merit, shown by the transition from blue to a pink/colourless shades at this particular grid position in images A-F.

The photo degradation of the resazurin dye to its pink resorufin intermediate occurred fully after roughly 35 minutes at the area of A4 (Figure 3.8). It became evident that grid position A4 was the only grid position which exhibited any quantifiable or meaningful

level of photo-catalytic activity. The photo-catalytic rate for this particular point was determined by measuring the increase in the red component of the digital image pixel, with respect to irradiation time, that makes up the image at grid position A4 by using a previously proven and published method.[149] The photo-catalytic rate at position A4 was calculated to be 1.37×10^{12} molecules destroyed per cm^2 per second. Compared to the activity reported for the composite material reported by Ponja *et al* it is roughly a third slower. The formal quantum yield (FQY) and formal quantum efficiency (FQE) for position A4 was calculated to be 3.6×10^{-3} molecules destroyed per absorbed photon and 3.02×10^{-3} molecules destroyed per incident photon respectively.

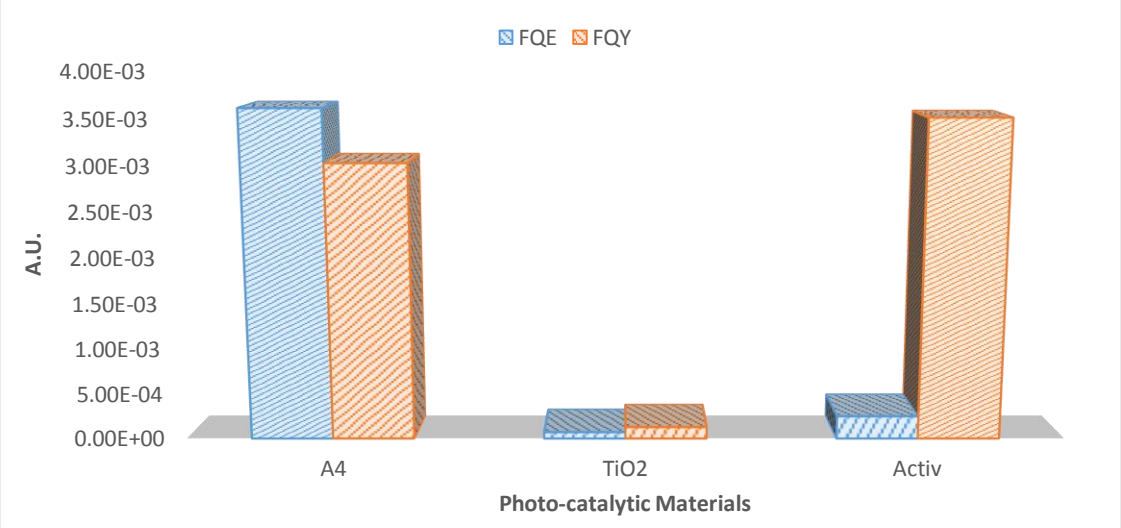

Figure 3.9: A comparison of FQE and FQY between; grid position A4, a TiO_2 sample grown by AACVD in ethyl acetate using identical deposition conditions to the combinatorial experiment discussed here and the Industry standard, Pilkington Activ™.

Figure 3.9 compares the observed FQE and FQY for grid position A4, TiO_2 (grown by AACVD in ethyl acetate at 450 °C using titanium (IV) isopropoxide) and commercial glass (Pilkington Activ™). Compared to Pilkington Activ™ the FQE is an order of magnitude higher but is on par with the FQY for A4. When FQE and FQY values are roughly equal it

indicates that a high percentage of the absorbed photons go on to be used in photo-catalytic surface reactions. This indicates that the material at A4 efficiently uses incident photons for surface redox reactions.

3.3.2.2 Water Contact Angles

Water contact angles were obtained for all grid positions. The entire film was then irradiated for 16 hours under UVA light (365 nm) and the water contact angles were re-measured (Table 3.5). The percentage change in water contact angle was calculated for all positions. The highest degree of angle change and thus photo-induced wettability was observed to be grid position A4 which corroborates photo-catalytic measurements. The composite materials previously reported pre-irradiation hydrophobic surface properties were not observed at A4. This could be due to poor uniformity across the surface morphology.

Table 3.5: Percentage change in water contact angle for all 20 grid locations.

	A	**B**	**C**	**D**	**E**
1	8.7	16.4	-6.2	19.2	-25.9
2	-17.6	9.1	-34.1	-6.1	-42.6
3	-57.4	-67.2	-54.2	-20.1	-29.7
4	-73.1	-70.7	-51.8	-19.8	-32.4

3.3.2.3 Two Point Resistivity

Two point resistivity measurements were taken to provide an empirical idea of relative tin and titanium areas as both pure TiO_2 and SnO_2 are classical intrinsic semiconductors and are thus bad conductors as the Fermi level lies directly between the valence band and conduction band, thus electrons can only migrate through the material once

promoted into the conduction band by photons of the correct energy or by thermal excitation. Doping of these materials is known to populate the Fermi level such that it lies very close to the conduction band and thus at room temperature (274 K) the conduction band of these materials will be populated by some electrons due to thermal excitation. As shown in XPS, both TiO_2 and SnO_2 phases are shown to exhibit varying levels of Sn^{4+} and Ti^{4+} doping. However, as the valence of these dopants is the same it cannot be expected that extra electrons have been added to the conduction band of TiO_2 and SnO_2 respectively. Another important aspect of resistivity measurements is that whilst a material might be intrinsically conductive, poor contact between crystallites will inhibit the movement of current through an area larger than the crystallites that fill that space. With this in mind the resistivity values found in Table 3.6 cannot be said to represent directly the materials at the corresponding grid positions as all exhibit differing surface morphologies, as seen in SEM. Whilst Ponja *et al* did not comment on the resistivity of the composite film subsequent measurements found that average values for the composite were found to be between $10^3 – 10^4$ Ω/□. Characteristically TiO_2 exhibits resistivity values inhibitive for use in applications where good conductivity is paramount.[175] SnO_2 as a pure intrinsic semiconductor should exhibit little in the way of conductivity and thus exhibit high resistivity values, however much literature has shown that oxygen vacancies form easily within the SnO_2 lattice, permitting the movement of charge and thus causing SnO_2 exhibit low resistivity values.[176–178] Distinguishing areas of titanium dioxide and tin dioxide should thus be readily evident compared to the composite material. As shown in Table 3.6, the right hand side of the film exhibits characteristic resistivity values for TiO_2. The bottom left hand corner of the film which is seen by XRD and XPS to be cassiterite SnO_2, is seen to exhibit characteristic

resistivity values expected for SnO_2. Specifically at A4 and B4 resistivity values are seen to mirror the expected values for TiO_2. These materials are majority TiO_2 but contradict values obtained for the original TiO_2/ SnO_2 composite reported by Ponja *et al*. This could be accounted for by considering that the morphology at A4 is not as pristine compared to that previously reported for the TiO_2/ SnO_2 composite. At B4 the morphology is seen to consist of small non-connected crystallites, explaining the lack of conductivity.

*Table 3.6: Two point resistivity measurements (*in Ω/□*) provide an insight into areas of titanium dioxide and tin dioxide due to the differing degree to which they conduct. High resistivity values indicate TiO_2 whereas low resistivity values suggest SnO_2.*

	A	**B**	**C**	**D**	**E**
1	5.94×10^2	4.70×10^2	5.13×10^4	5.00×10^6	5.00×10^6
2	3.60×10^3	1.54×10^4	3.38×10^4	1.10×10^6	5.00×10^6
3	1.76×10^5	1.31×10^5	6.64×10^4	1.10×10^6	1.20×10^6
4	1.09×10^6	1.80×10^4	6.57×10^4	1.10×10^6	1.30×10^6

3.4 Discussion

A thin film which graduated from SnO_2 to TiO_2 across its width was created using combinatorial aerosol assisted chemical vapour deposition (C-AACVD). The precursors were introduced into the reactor separately using a specially designed baffle, ensuring the individual aerosol sources mixed only once within the confines of the reactor. By utilising a simple grid overlay many samples could be 'created' and analysed. This also allowed the fast and efficient mapping of changes in functional properties that arise from differing elemental ratios across the surface of the film. By performing a

combinatorial experiment many intermediate states between cassiterite SnO_2 and anatase TiO_2 were also created in one experiment.

Characterisation methods such as XRD, XPS, EDX, UV-visible spectroscopy and SEM have allowed changes in crystal structure, titanium to tin ratio and resultant morphology across the films width and length that occur as a result of the combinatorial approach to be compared to changes in observed functional properties such as photo-catalysis and photo-induced wettability. Generally, progressing from left to right the dominant crystal phase changes from cassiterite SnO_2 to anatase TiO_2, with mixed phases found to exist in between.

X-ray photoelectron spectroscopy corroborated this observation. The observed ratio of titanium to tin was observed to increase as focus progressed from left to right regardless of whether the focus is the surface of the film or in the bulk. It appears, sparing A1 and B1, all grid positions are tin rich at the surface but TiO_2 becomes the dominant phase in the bulk. EDX has shown that titanium dioxide is the dominant phase across the majority of the film except where the tin precursor enters the reactor and corroborates what is concurrently found in XPS. This phenomenon of phase segregation of SnO_2 relative to TiO_2 has been reported previously in the literature.[179,180] SEM largely shows the expected morphologies for respective tin dioxide and titanium dioxide areas found in XRD but square based pyramidal monolithic growths similar to those reported previously for the composite TiO_2/ SnO_2 composite were also observed. The quality and density of the crystallites was lower however. Film thickness was found to be of the expected magnitude.

Functional testing was also undertaken at all grid positions to map the change in functional properties across the length and width of the film. Photo-catalysis studies using a resazurin based 'intelligent ink' showed that only A4 exhibited photo-catalysis of merit. The photo-catalytic rate was calculated to be 1.37 x 10^{12} molecules destroyed per cm^2 per second with a FQY and FQE of 3.02 x 10^{-3} and 3.6 x 10^{-3} respectively. Whilst the photo-catalytic rate is comparable to that reported previously for a TiO_2-SnO_2 composite thin film the FQY and FQE are an order of magnitude lower, this is attributed to the lower quality and density of the monolithic growths seen in SEM compared with those reported by Ponja *et al*.

Photo-induced wettability was found to be as expected. Areas that experienced the greatest degree of water contact angle change were those of photo-catalytic interest, A4 experienced the greatest change with surrounding areas showing large changes. A change in water contact angle was observed at the TiO_2 grid positions but the change was not as high as at A4. Resistivity values were of expected magnitude and confirmed the combinatorial nature of the film.

The use of combinatorial AACVD has succeeded in replicating the TiO_2 / SnO_2 composite first reported by Ponja *et al*. and the mechanistic insight achieved by utilising C-AACVD has demonstrated that the composite does not form simply as a result of a specific elemental composition. If this were the case it would be expected that the composite would form (assuming equal aerosol flow) somewhere in the middle or to the right of the grid positions where titanium concentration is highest, this is because in the bulk or at the surface, although it may vary, titanium is predominant and these positions reflect this dominance in concentration relative to tin. That the composite is observed in the

top left hand corner, where SnO_2 would be expected to form preferentially without TiO_2 being present suggests that the composite exhibits a complex growth profile which cannot be probed fully by considering simply the relative concentration of Sn relative to Ti. Further studies are therefore required to truly pinpoint the origin of the heterojunction structure seen in the composite.

3.5 Conclusions

Combinatorial AACVD has been used for the first time to replicate the growth of a mixed phase thin film of technological interest, specifically a TiO_2/ SnO_2 composite film. It is evident that the composite exhibits a growth profile which is too complex for considerations of elemental ratio to provide adequate answers. This is asserted as, assuming the film is a product solely of a specific elemental ratio, it should be seen in columns B, C or D. That it is found in column A, where the combinatorial regime should ensure that SnO_2 is the dominant and only phase at the position suggests there exists other factors important to the formation of the composite material. Regardless the technique has a proven track record of charting functional properties as a function of elemental ratio[139] and can now add the demonstrated ability to replicate complex advanced functional materials to its accomplishments. This will have implications in the future for predicting dopant concentrations responsible for the growth and formation of specific phases and will help tailor future experiments to enable the growth of higher quality films and the enhancement of previously reported functional properties as AACVD garners industrial acceptance.

4 Chapter IV: The Use of Time Resolved Aerosol Assisted Chemical Vapour Deposition in Mapping Thin Film Growth in a TiO_2 / SnO_2 Composite Film

4.1 Introduction

Following the combinatorial deposition and successful reproduction of the TiO_2/ SnO_2 composite in Chapter III, it was concluded that methods for further exploring the mechanism of formation of the composite were required. XPS depth profiling showed that the material displayed little in the way of elemental homogeneity with a high relative surface concentration of Sn to Ti. The observation that the material also formed in the top left hand corner of the combinatorial film, which should have been exclusively SnO_2, suggests that Sn plays an integral role in the formation of the composite. This suggested that the material must exhibit a specific growth profile, as the composite is not observed for films where a SnO_2 layer is deposited on top of an already deposited TiO_2 layer. Thus a method for probing the growth profile was sought that could also generate several samples representative of different periods throughout the deposition in a single deposition. The study could be completed by doing several depositions that vary by deposition time but this would be time consuming. In the same manner that combinatorial AACVD can be used to create many samples that vary with respect to elemental composition in a single deposition, a method of achieving many samples that vary as a function of deposition time was sought. This would allow two things:

- Study of the film's growth profile, so as to provide a mechanistic insight into the growth of thin films in AACVD, an aspect not yet addressed in the literature.

- Once changes in crystallinity, elemental composition and functional properties have been mapped as a function of time, fine tuning of the material functional properties, such as photo-catalysis or conductivity, could be selected by simply varying deposition time. Allowing the material deposited to be maximised in a specific application.

A method to achieve this was conceived which made use of the exhaust of the reactor. As AACVD is carried out at atmospheric pressure, the exhaust and by extension the deposition chamber are freely accessible given the proper safety considerations. The time resolved samples were generated by withdrawing a cover across the surface of the glass at specific time intervals revealing areas of uncoated glass throughout the deposition process (Figure 4.1). The samples were characterised and their functional properties mapped.

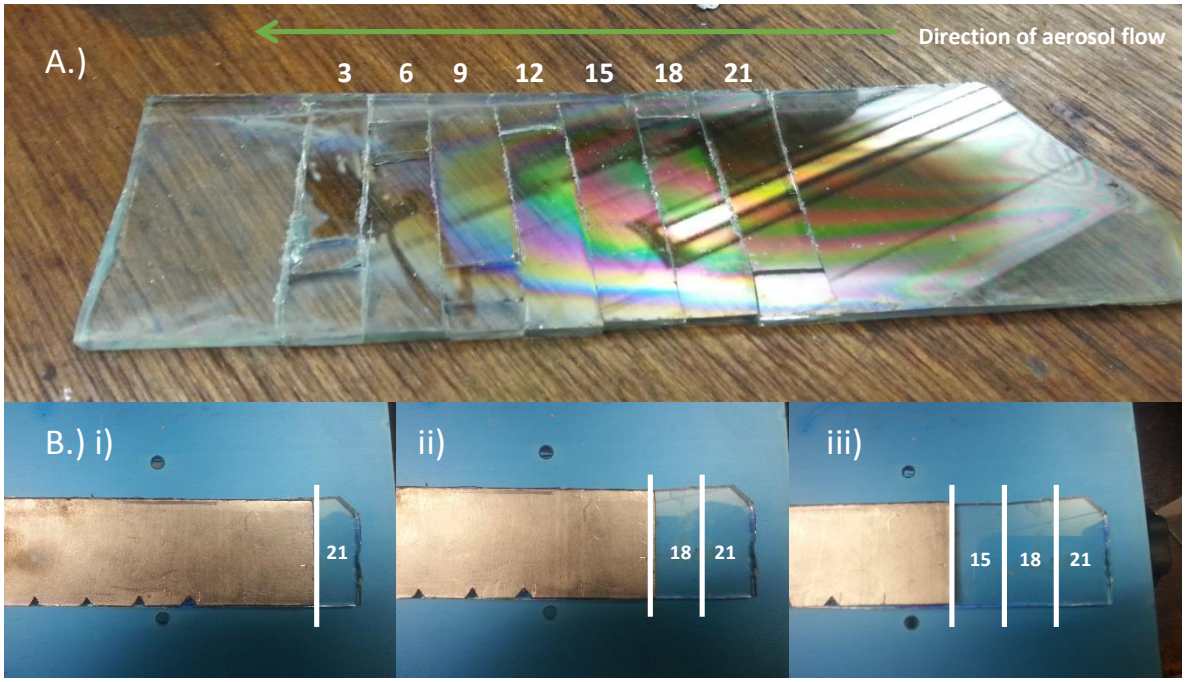

Figure 4.1: A.) Image of final deposited film with labelled timed segments cut into segments for characterisation. Films were deposited by AACVD at 450 °C under N_2 gas flow of 1 l/min using titanium (IV) isopropoxide and butyl tin trichloride dissolved in ethyl acetate in the same flask. The gradation of film thickness is apparent from the least deposited sample (3 minutes) to the most deposited sample (21 minutes) initially verifying on a visual level the principle of the experiment. B.) Images i), ii) and iii) demonstrate the process of how the cover is removed every 3 minutes to reveal fresh clear areas of glass upon which deposition can take place, creating sequential areas across the whole deposition. For example in image i) an initial area of glass is left to provide the sample with the longest deposition time. ii) After 3 minutes the cover is withdrawn a set distance via the exhaust to reveal the next sample and the process is repeated until the deposition is finished. The observance and continuation of an interference pattern, characteristic of the build-up of individual layers, throughout all samples despite the presence of a cover at varying points throughout the deposition indicates that the cover does not hamper or impinge on overall flow dynamics and film formation.

4.2 Experimental

4.2.1 Thin film Preparation using AACVD

Nitrogen (99.99%) (BOC) was used as supplied. Depositions were obtained on SiO_2 coated float-glass. Prior to use the glass substrates were cleaned using water, isopropanol and acetone and dried in air. Glass substrates of ca. 45 mm x 5 mm x 4 mm were used. The precursors, titanium (IV) isopropoxide (99%) and tin (IV) butyl tri-

chloride (99%) were obtained from Sigma-Aldrich Chemical Co. and used as supplied. Aerosols were generated in ethyl acetate (99%) and carried into the reactor in a stream of nitrogen gas through a brass baffle to obtain a laminar flow. A graphite block, containing a Whatmann cartridge heater, was used to heat the glass substrate. The temperature of the substrate was monitored using a Pt–Rh thermocouple. Depositions were carried out by heating the horizontal bed reactor to the required temperature of 450 ^{o}C before diverting the nitrogen line through the aerosol and hence to the reactor. The total time for the deposition process took 20- 25 minutes. At the end of the deposition, under the nitrogen flow, the glass substrates were left to cool to room temperature with the graphite block before it was removed. To modify the experiment to provide a time resolved study a chemically inert cover, a thin graphite foil was inserted via the exhaust into the reactor and withdrawn at specific time intervals to achieve areas of glass of differing deposition times. Initially the cover only revealed a small area of glass on which deposition can take place. By doing this eight samples can be generated in a single deposition.

4.2.2 Sample Characterisation

X-ray diffraction (XRD) was carried out using a Lynx-Eye Bruker X-ray diffractometer with a mono-chromated Cu Kα (1.5406 Å) source. X-ray photoelectron spectroscopy (XPS) was carried out using a Thermo Scientific K-Alpha instrument with monochromatic Al-Kα source to identify the oxidation state and chemical constituents. High resolution scans were done for the Ti (3d), Sn (3d), O (1s) and C (1s) at a pass energy of 40 eV. The peaks were modelled using Casa XPS software with binding energies adjusted to adventitious carbon (284.5 eV). SEM images were taken on a JEOL JSM-6301F Field Emission instrument with acceleration voltage of 5 kV. Images were captured using

SEMAfore software. Samples were cut into coupons representing the different timed samples and coated with a fine layer of gold to avoid charging. The optical transmission was measured over 320–800 nm range using a Lamda 950 UV/Vis spectrometer. Film thickness was calculated using a Filmetrics F20 thin-film analyser.

4.2.3 Functional Property Testing

Photo-catalytic activity was assessed using an established method based on a resazurin 'intelligent ink' first developed by Mills *et al.* [168] Photo induced wettability was tested by placing the samples under a UVC lamp for 2 hours then measuring the water contact angle by placing a 5 µL droplet onto the surface of the films. The film was then irradiated overnight for 24 hours and water contact angles were re-measured. Two point resistivity measurements were undertaken with a multimeter. Water droplet contact angles were measured using a First Ten angstroms 1000 device with a side mounted rapid fire camera after casting a 5 µL droplet from a fixed height onto the surface. To assess the photo-catalytic activity of the films the samples were washed with water, rinsed with isopropanol and irradiated for 30 minutes to clean and activate the sample. A resazurin based ink was then evenly applied using a spray gun and the photo-induced degradation of the resazurin ink monitored by UV-Vis spectroscopy. Formal quantum efficiency and the formal quantum yield was then calculated. Formal quantum efficiency was calculated by dividing the rate of dye molecules destroyed per s per cm^2 by the photon flux (4.53×10^{14} photons per cm^2 per s). The formal quantum yield (FQY) was calculated by dividing the rate of dye molecules destroyed per s per cm^2 by the number of photons absorbed by the films. The photon flux and photon absorption for each film was determined using a UVX digital radiometer with a detector for 365 nm radiation attached.

4.2.4 Preparation of 'intelligent ink' solution

Glycerol (99.6%), hydroxy ethyl cellulose [average MV ¼ 90 000], resazurin (92%) were all purchased from Sigma-Aldrich Chemical Co. and used as supplied. The 'intelligent' ink consisted of resazurin (40 mg) redox dye in an aqueous solution (40 mL) with glycerol (3 g) and hydroxylethyl cellulose (0.45 g) that was aged for 24 hours at 3–5 ^{0}C. The solution was mixed thoroughly before use.

4.3 Results

A 1:1 solution of titanium (IV) isopropoxide and butyl tin (IV) trichloride dissolved in ethyl acetate was used as the precursor solution to deposit the TiO_2/ SnO_2 composite material by AACVD in the manner described in the experimental. Utilising a novel setup involving a retractable cover slip, samples representing differing deposition times were easily generated.

4.3.1 Characterisation

The average time for a full deposition for 20 ml of ethyl acetate at a nitrogen flow of 1l/ min, until the aerosol source was fully exhausted, was shown to be between 20 and 25 minutes. The time interval for depositions was set at 3 minutes and in total seven different films were deposited which varied as a function of deposition time. The structural changes across these films were characterised using X-ray diffraction (XRD), X-ray photoelectron spectroscopy (XPS), scanning electron microscopy (SEM) and UV-Visible spectroscopy. Any changes in functional properties across the samples, that arise from corresponding structural changes, were followed by photo-activity measurements using a resazurin based 'intelligent ink' and photo-induced wettability studies.[168]

4.3.1.1 X-ray Diffraction (XRD)

An X-ray diffraction study was undertaken for all samples (Figure 4.2) to provide insight into the evolution of crystal structure growth as a function of time. Anatase TiO_2 and cassiterite SnO_2 phases were observed at different points in time throughout the deposition process. After nine minutes the formation of anatase TiO_2 was observed, which exhibits strong preferential orientation with complete suppression of the [200] plane and partial suppression of the [101] and [105] planes whilst exhibiting enhancement in the [004] plane. At this time anatase TiO_2 is the only crystal phase observed. This phase continues to grow in intensity throughout the deposition process. From 18 minutes onwards cassiterite SnO_2 phases appear, specifically the [101] and [211] planes.[167] It is evident that the process of modifying the deposition regime, to provide samples at different deposition times, did not hamper or inhibit the growth of the material under investigation in this study. This can be seen in the continuation of the contour thickness planes in Figure 4.1A. These are due to reflection from the film and glass producing an optical interference pattern due to minute (nm) variations in film thickness.[158]

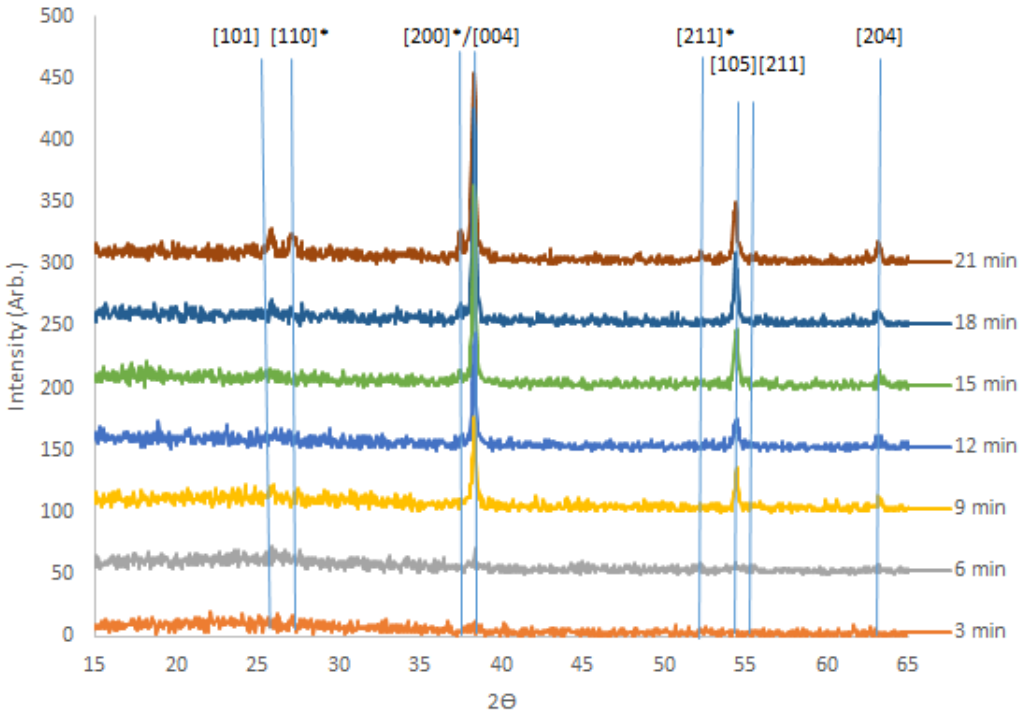

Figure 4.2: XRD patterns of films deposited at 450 °C by AACVD using titanium (IV) isopropoxide and butyl tin trichloride. Miller Indices denoted with correlate with cassiterite SnO_2 phases. All other Indices are anatase TiO_2. It is apparent that very little in the way of crystalline material exists at 3 minutes but crystalline material representing anatase TiO_2 appears after 6 minutes and continues to grow in prominence throughout the rest of the deposition. Cassiterite SnO_2 only appears after 15 minutes and continues to increase in peak intensity until at 21 minutes cassiterite SnO_2 peaks and anatase TiO_2 peaks exist concurrently.*

4.3.1.2 X-ray Photoelectron Spectroscopy (XPS)

X-ray photoelectron spectroscopy (XPS) was undertaken for samples representing all time intervals. This was to identify the elements present, relative elemental ratios and their respective oxidation states. Depth profiling was conducted to profile how the tin: titanium ratio changes from the surface to the bulk within a specific film.

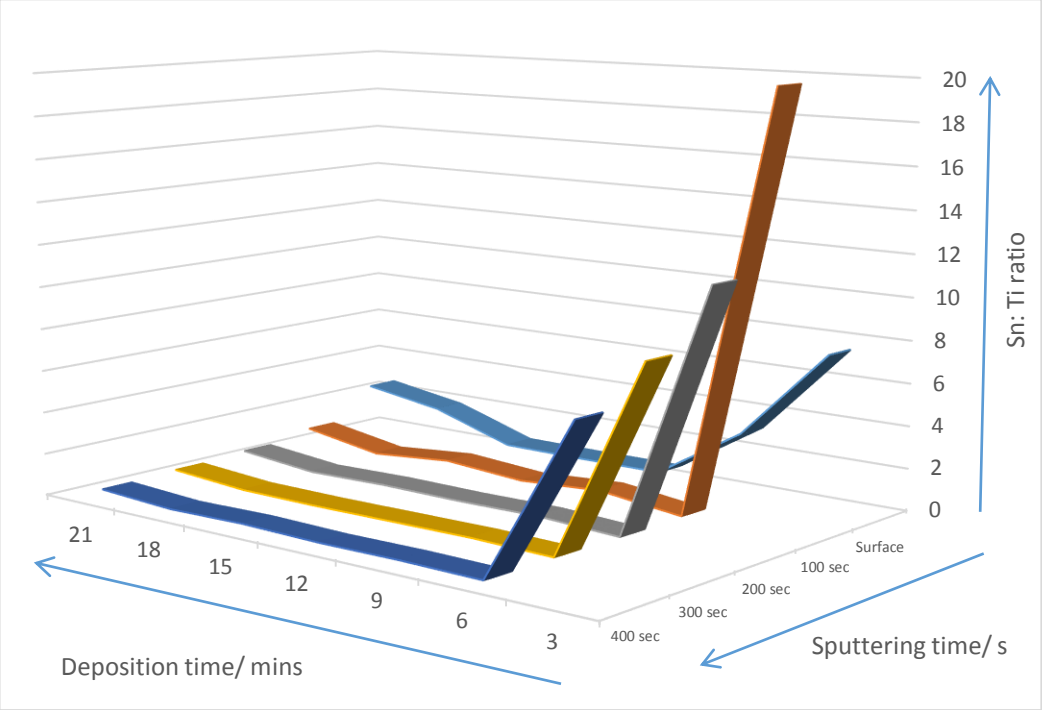

Figure 4.3: A graph comparing the Sn: Ti atomic ratio in XPS depth profiling across all timed samples formed from AACVD of titanium isopropoxide and butyl tin trichloride at 450 °C. All samples were etched for 100s, this was repeated 4 times to achieve 4 levels within the bulk. Across all samples; after 3 minutes tin concentration is high, averaging about 10 times more abundant than titanium. Six minutes into the deposition titanium levels start to increase relative to tin until after 9 minutes titanium becomes the dominant element with the ratio of Sn: Ti becoming <1. In general within the bulk Sn concentration increases relative to titanium but the ratio of Sn to Ti remains <1. After 18 minutes Sn becomes the dominant element at the surface with a Sn: Ti ratio >1.

Peaks representing TiO_2 at 458.3 eV (Ti^{4+} $2p_{3/2}$) and 463.9 (Ti^{4+} $2p_{1/2}$) eV were found in all samples. Tin peaks matching previous literature reports for SnO_2, are observed at 486.5 eV (Sn^{4+} $3d_{5/2}$) and 494.9 eV (Sn^{4+} $3d_{3/2}$).[173,180] After three minutes of deposition, tin 4+ was found to be the dominant element relative to titanium 4+ at both the surface and within the bulk (Figure 4.3). After six minutes of deposition time levels of tin relative to titanium decreased until after 9 minutes when the surface was now observed to be tin rich compared to the bulk but the ratio of tin to titanium remains <1, with the bulk material exhibiting less tin but in concentrations significantly higher than would be

expected if tin was present in a typical dopant regime. Twelve minutes of deposition time produced a very similar picture with a surface richer in tin, relative to titanium, compared to the bulk but still in minority to titanium. This general pattern was found after 15 minutes of deposition time. After 18 minutes of deposition time the surface exhibited a tin to titanium ratio >1 whilst the bulk continued to exhibit a Sn: Ti ratio <1. A full deposition time of 21 minutes exhibited a similar profile, with a surface Sn: Ti ratio >1 with a bulk ratio <1. When cross referenced with XRD it was observed that the cassiterite SnO_2 peaks coincided with the surface Sn: Ti ratio from XPS switching from <1 to >1. This indicates that SnO_2 formation occurs at the TiO_2 surface as a result of dynamic surface segregation[181] that causes Sn^{4+} to move to the surface from the bulk, when the Sn surface concentration becomes high enough (Sn: Ti >1) SnO_2 is produced at the surface (Figure 4.4). Shadowing earlier reports, oxygen 1s XPS spectra for samples representing 9 minutes onwards exhibit, within the bulk, characteristic lattice oxygen values at 530.1 eV characteristic of a Sn-O-Ti linkage. Standard oxygen values for standard TiO_2 and SnO_2 were also exhibited (Figure 4.5). This indicates that tin acts as a substitutional dopant within the TiO_2 matrix.[182,183]

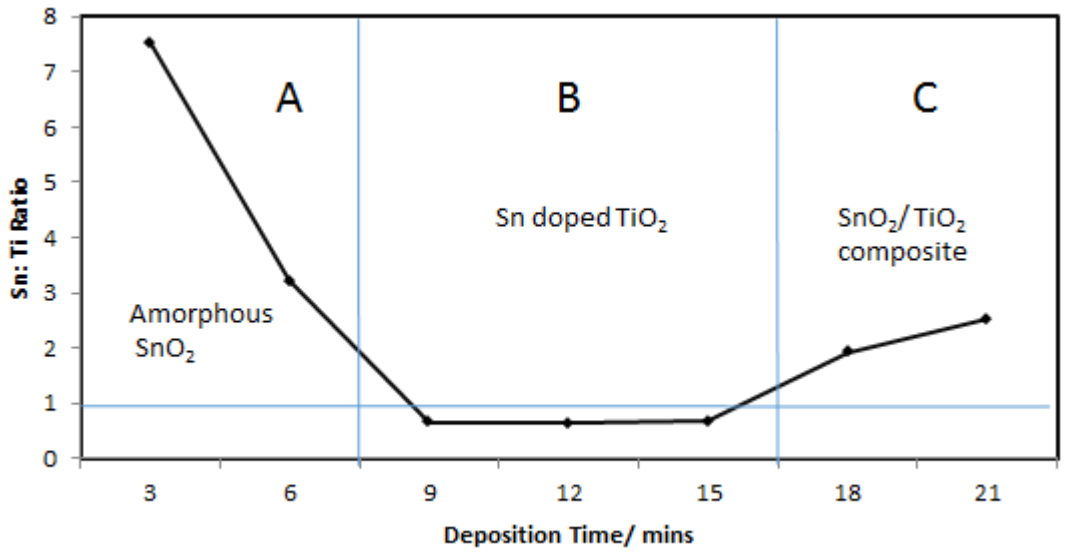

Figure 4.4: A graph displaying Sn: Ti ratio for the surface only. There are 3 distinct areas: A) 3-6 minutes: this represents a deposited amorphous solid solution of SnO_2 with traces of titanium 4+. B) 9-15 minutes: tin concentration decreases to become the minority element relative to titanium producing a solid solution of tin doped titanium dioxide. C) 18- 21 minutes: It is seen that after 18 minutes Sn becomes the majority element at the surface. This coincides with XRD which displays cassiterite SnO_2 after 18 minutes. This implies that first a seed layer of amorphous SnO_2 forms (A). This allows the growth of a solid solution of tin doped anatase TiO_2 as seen in XRD (B). It is from this solid solution that Sn surface concentration increases enough to become the majority element at the surface forcing the growth of cassiterite SnO_2 (C).

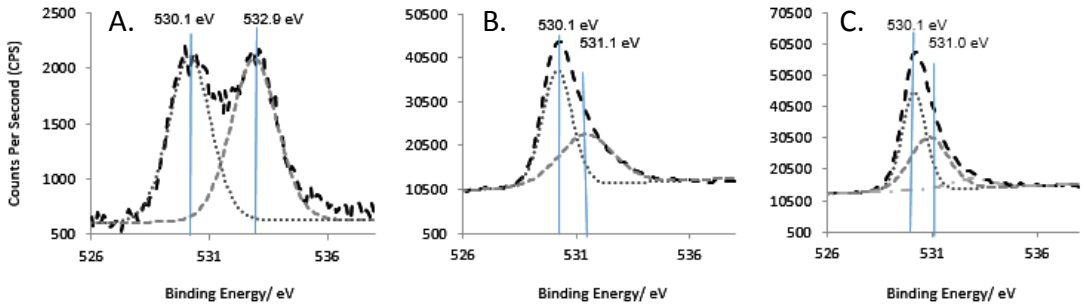

Figure 4.5: Modelled XPS peaks for 1s Oxygen peaks after 200 seconds of sputtering for 15 (A), 18 (B) and 21 minutes (C) worth of deposition time. The peak at 530.1 eV, representative of a Ti-O-Sn linkage within the TiO_2 matrix, is seen to increase in intensity as deposition time increases. This shows that 1. Sn exists as a substitutional dopant and 2. It increases in concentration within the bulk at the same depth, relative to the surface, with increasing deposition time.

4.3.1.3 Scanning Electron Microscopy (SEM)

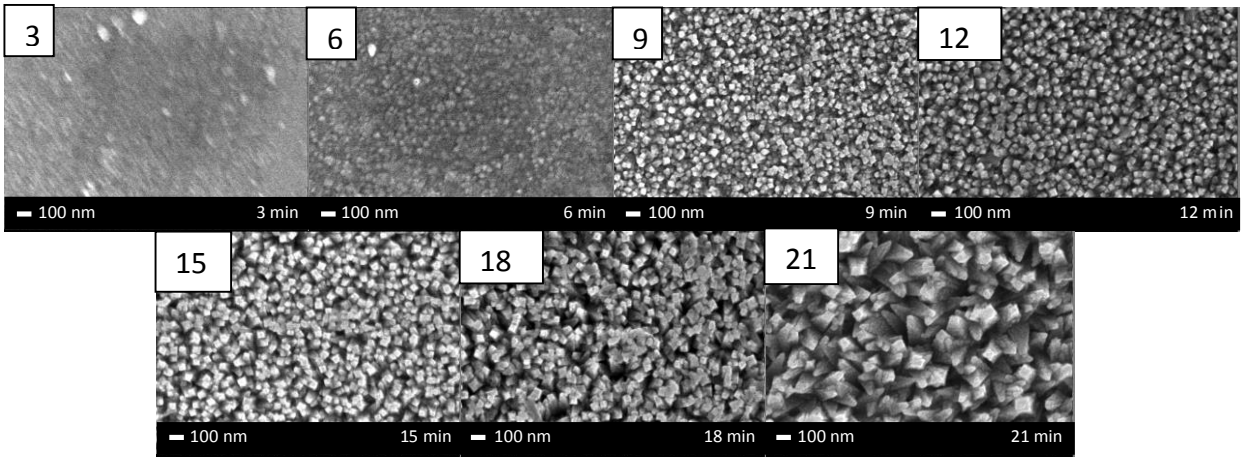

Figure 4.6: A time lapse of SEM images representing 3, 6, 9, 12, 15, 18 and 21 minutes of the deposition process. It is evident that film formation occurs after 3 minutes with evidence of granular particulate matter forming with no overall order. After 9 minutes square structures start to appear and become progressively larger as the deposition process continues in time. Eventually the morphology resembles large monolithic square based pyramids after 21 minutes.

Surface morphology was investigated by scanning electron microscopy (SEM) to give an insight into how the film grows over time whilst also providing additional information relevant to understanding how the photo-activity and water contact angles change over time. After three minutes of deposition particular material was observed which displayed no overall structure (Figure 4.6). After six minutes the particles appear to continue to nucleate and grow in size whilst still displaying little to no regular structure. Nine minutes into the deposition crystallites displaying an overall regular structure were observed, hinting that the growths were starting to adopt a 2-dimensional square-like geometry. The square geometry is emulated and repeated throughout depositions representing 12, 15 and 18 minutes. Overall, both crystallite size and porosity were noted to increase with deposition time. After 21 minutes of deposition time large crystallites around 100 nm in width with a square 2D profile and pyramidal 3D profile were observed whilst retaining the porosity of previous time intervals.

4.3.1.4 Ultraviolet-Visible Spectroscopy

Ultraviolet-visible absorption spectroscopy was undertaken to explore how absorption, transmission and band gap for individual samples, representing differing deposition times, vary over time. Transmission data were obtained from the absorption data. It is evident from Figures 4.7 and 4.8 that the observed transmission was inversely proportional to deposition time. On a simplistic level this corroborates the observation that the film increases in thickness with deposition time. Analysis of the band gap for each timed sample was calculated using tauc plots (Figure 4.9). It was evident that whilst initially the band gap was closer to the expected band gap value for cassiterite SnO_2 (3.6 eV) the values steadily decreased over time and stabilised at around 3.2 eV which is characteristic of anatase TiO_2 from 12 minutes onwards. Lack of cassiterite SnO_2 peaks in the XRD at these early time intervals (3-9 minutes) suggests that these high values are due to film thickness and the resulting limitations of tauc plot analysis for extremely thin films. This is highlighted in SEM where significantly altered film morphology was not seen to occur until 9 minutes into the deposition. By comparing band gap values with absorption and transmission data it is concluded that because band gap values do not change over time once stabilising at 3.2 eV the apparent red-shifting observed in the absorption data can be attributed to increasing film thickness.

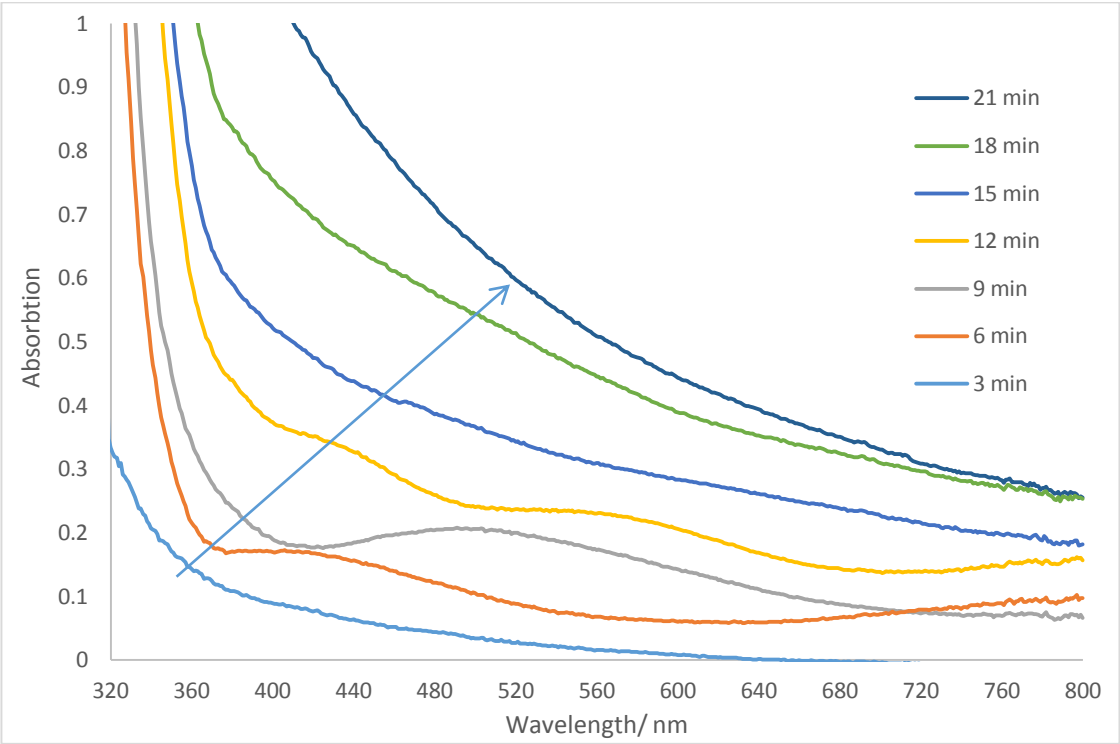

Figure 4.7: Absorption spectra for all time resolved samples deposited at 450 °C by AACVD. It is apparent that as respective deposition time increases samples permit less and less light to permeate through their structure.

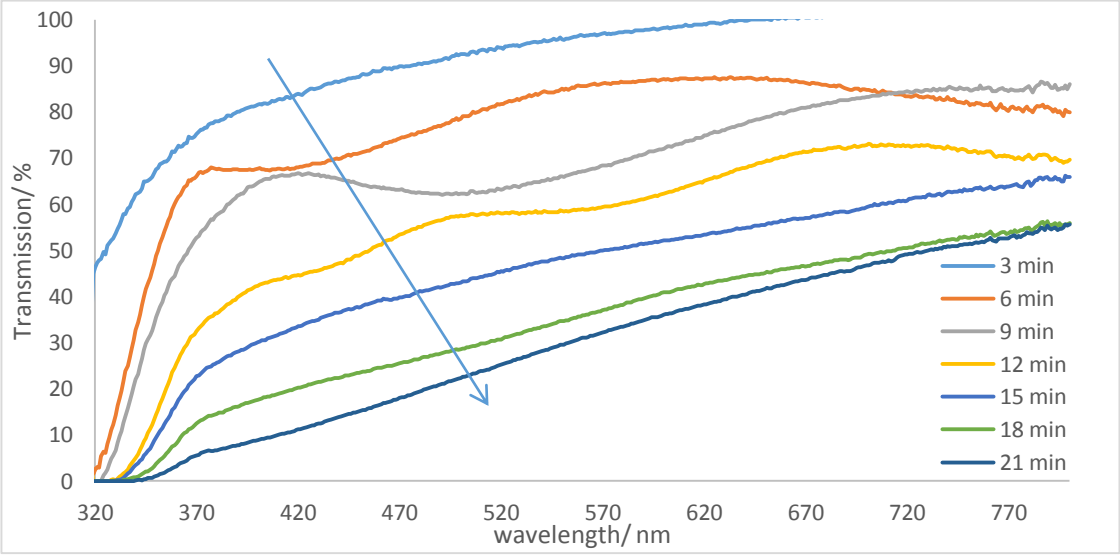

Figure 4.8: Transmission data for all time resolved samples deposited at 450 ° C by AACVD. Transmission appears to decreases as deposition time increases; verifying, on a qualitative level, that film thickness increases as deposition time increases.

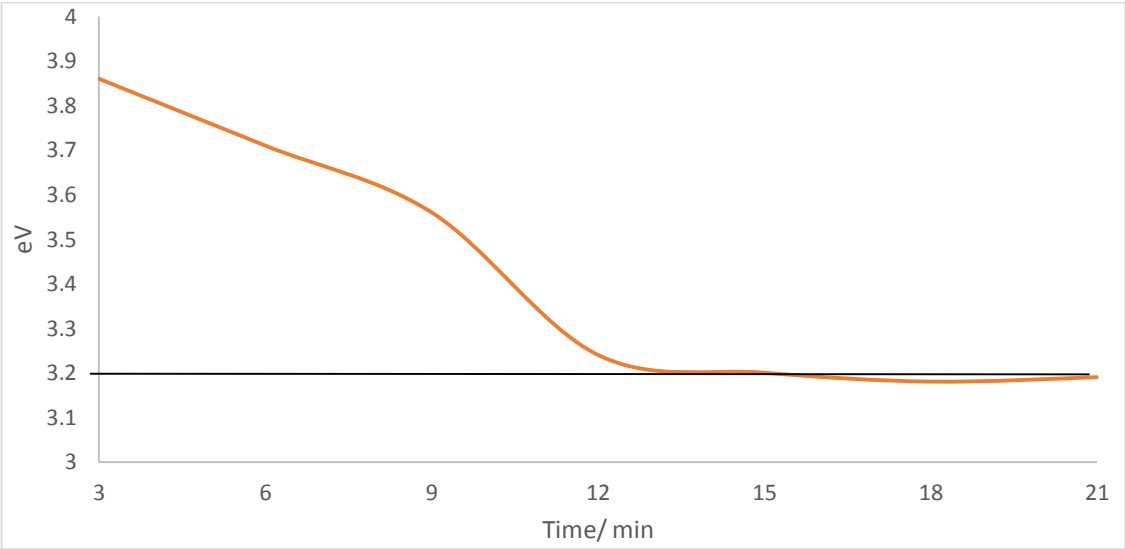

Figure 4.9: A graph charting the change in band gaps of the TiO_2/ SnO_2 composite material over time throughout the deposition process. Because the band gap is found to rest and stabilise at 3.2 eV for most samples, changes in absorption data cannot be attributed to red-shifting of spectra but to film thickness increasing.

4.3.1.5 Film Thickness

Film thickness measurements were obtained using the Swanepoel method to gain an insight into how thickness progresses throughout the deposition.[158] It is clear that film thickness increases proportionally with deposition time in a linear fashion (Figure 4.10). This indicates that the stream of precursor is roughly constant throughout the deposition process until the aerosol source is exhausted.

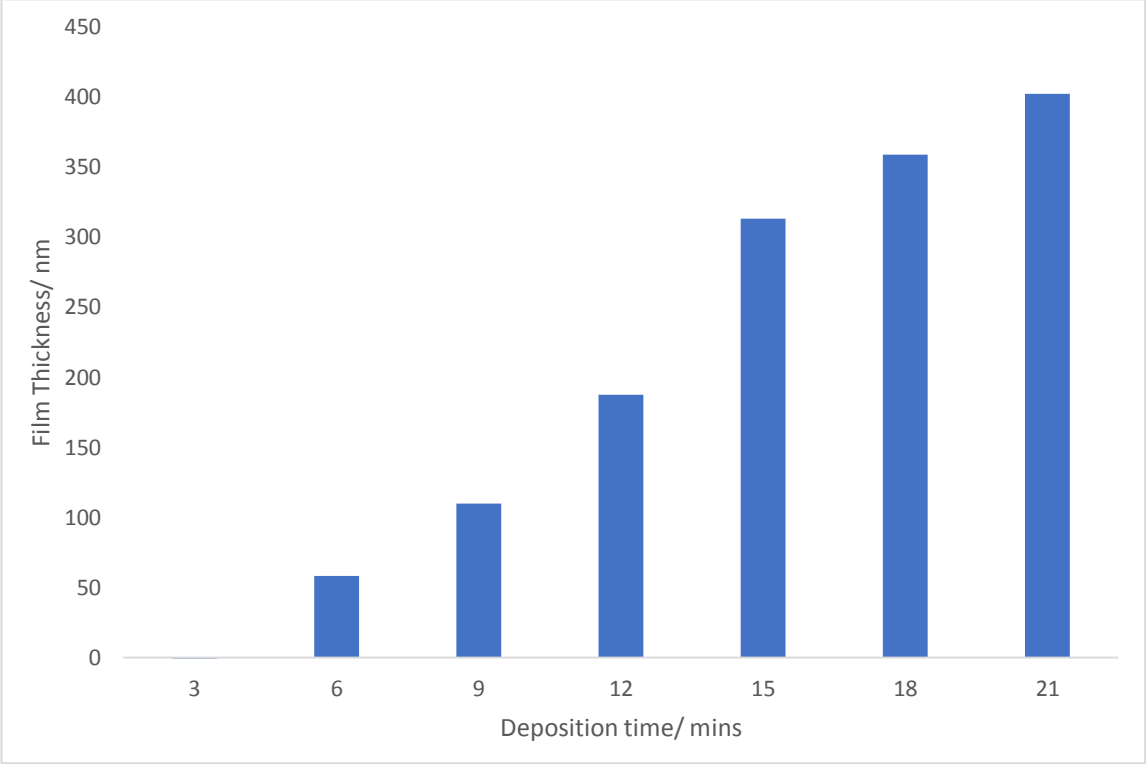

Figure 4.10: Thin film thickness as a result of time in the deposition of titanium (IV) isopropoxide and tin butyl trichloride at 450°C by AACVD. Film thickness is seen to increase in a linear fashion proportionally with deposition time indicating that both the precursor stream is roughly constant in intensity and also identity.

4.3.2 Functional Properties

4.3.2.1 Photo-Activity

Photo-activity measurements were obtained for all samples using a resazurin based 'intelligent ink'. This allowed for the rate of photo-activity to be tracked throughout the deposition process. It was found that all samples exhibit different rates of photo-activity and that these change in relative intensity throughout the deposition process (Figure 4.11) hinting that variances and transitions in structure and morphology could be responsible for this change in function. Formal quantum efficiency (FQE - the amount of dye molecules destroyed per incident photon) and formal quantum yield (FQY - amount of dye molecules destroyed per absorbed photon), which provide a quantitative

measure of a samples ability and efficiency to absorb light, was found however to mirror and track with changes in rates of photo-activity across all samples (Figure 4.12).

It is apparent that photo-activity alters dramatically across samples and thus throughout the deposition process. Photo-activity starts relatively low from 3-6 minutes but proceeds to increase substantially until 15 minutes upon where activity proceeds to then decline until the full deposition time is reached at 21 minutes. Therefore a 'state' of enhanced photo-activity exists, representing 15 minutes' worth of deposition time that would not be achieved in a traditional deposition regime and thus would not be identified otherwise.

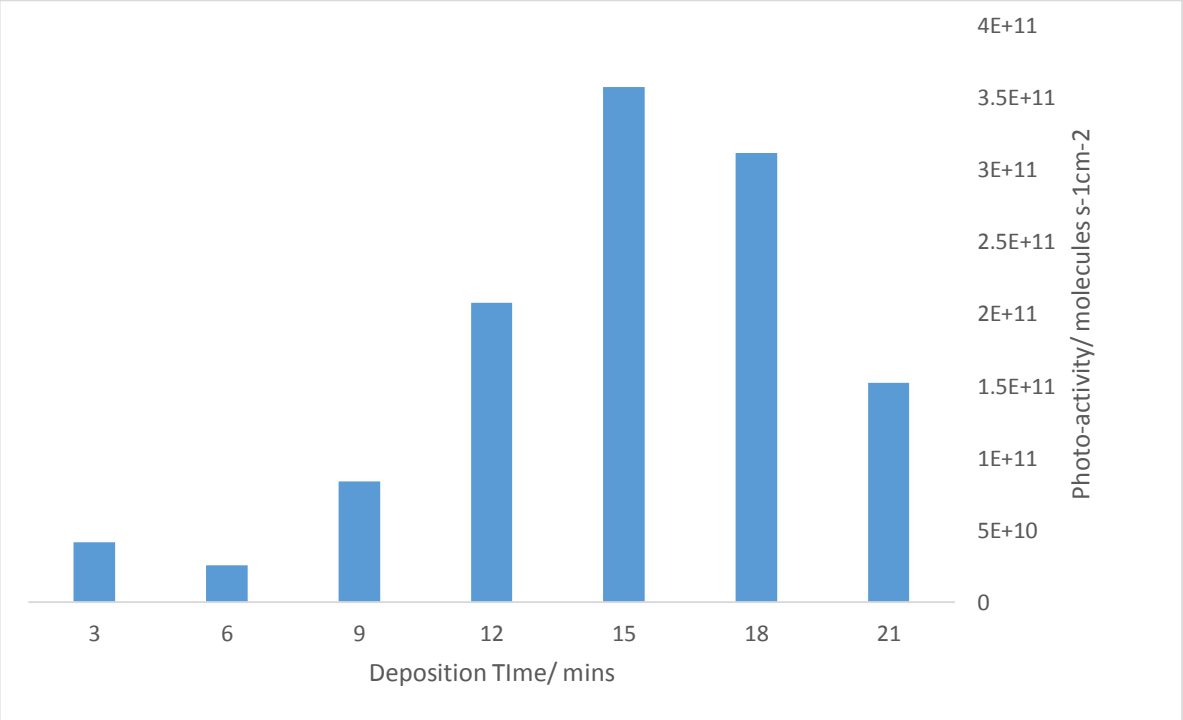

Figure 4.11: A graph comparing photo-activity for all samples. It appears to start low (3-6 minutes) but then increase between 9-15 where it reaches a maximum and decreases from 15-21 minutes. This indicates that there are states which exhibit higher rates of photo-activity which would normally be inaccessible with a traditional deposition regime.

Throughout the deposition process FQE and FQY remain relatively disparate from each other, signalling that whilst the films photo-activity changes in intensity the films'

efficiency in absorbing UV photons for use in photo-catalytic processes remains similar. At 21 minutes FQE and FQY appear to converge, signalling that a higher percentage of photons are absorbed and subsequently used in the generation of photo-electrons and holes. Therefore whilst the sample at 21 minutes exhibits lower photo-activity than samples 12- 15 it is a more efficient photo-catalyst (Figure 4.12). For the composite material formed after 21 minutes both FQE and FQY values are lower than those reported by Ponja *et al*, this could be attributed to many things such as transparency and doping levels.[167]

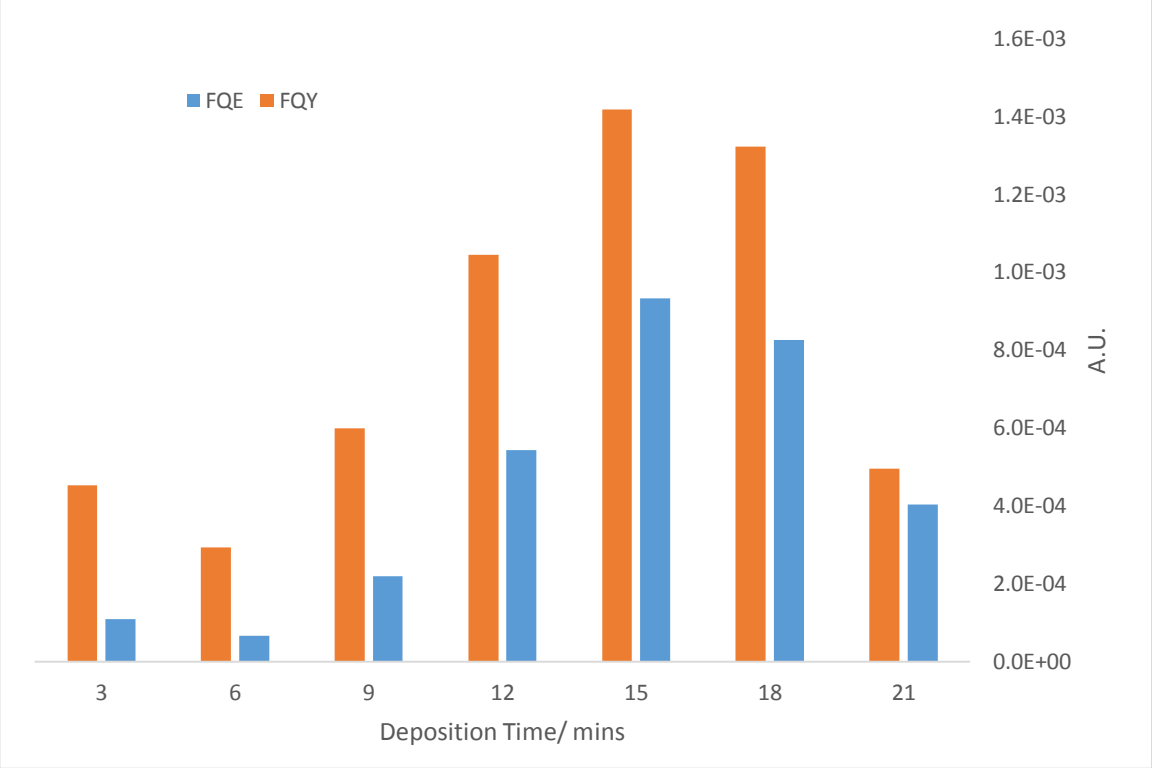

Figure 4.12: A graph comparing the relationship of formal quantum efficiency and formal quantum yield for each sample which charts how they change between samples and thus over time.

4.3.2.2 Water Contact Angles

Water contact angles were measured pre- and post-UVA (365 nm) irradiation to ascertain which samples exhibit photo induced wettability and how this particular

functional property changes with deposition time (Table 4.1). It was observed that hydrophobicity was immediately apparent from 3 minutes into the deposition process and continued to increase by roughly 10 degrees until a deposition time of 18 minutes. After 21 minutes the contact angle decreases to a similar value as 3 minutes. The samples were then irradiated under UV light (365 nm) for 24 hours. Samples were retested to determine the change, if any, in water contact angle post irradiation. It was found that for samples representing 3-12 minutes deposition time little or no change occurs. However from 15 minutes onwards a decrease in contact angle was observed for all samples. The largest decrease in contact angle was found at 18 and 21 minutes. This was attributed to a change in morphology and surface properties that occur when the Sn: Ti ratio, as observed in XPS, changes from being <1 to >1 and the observance of SnO_2 in the XRD for these samples which sequesters electrons, preserving holes which induce surface defects which water can co-ordinate into. The initial hydrophobicity observed for all samples is characteristic of nanoscale monolithic growths found in previous studies on a range of materials which also exhibit nanoscale (100 nm) monolithic surface morphology.[184–187] Due to nanoscale monoliths present in surface morphology the surface exhibits a high degree of roughness.[188]

Table 4.1: Table comparing water contact angle values for all timed samples pre and post irradiation with UVA (365 nm) light.

Deposition Time/ minutes	Pre-Irradiation/ °	Post-Irradiation/ °
3	111.4	100.1
6	112.0	110.4
9	112.0	113.3
12	115.9	110.4
15	120.0	100.8
18	124.7	68.3
21	114.4	70.3

4.4 Discussion

Time resolved aerosol assisted chemical vapour deposition (TR-AACVD) was used for the first time to map thin film growth as a function of deposition time. The deposition was carried out at 450 °C under a N_2 gas flow using a titanium dioxide precursor (titanium (IV) isopropoxide), a tin dioxide precursor (butyl tin (IV) trichloride) and an oxygen source (ethyl acetate) dissolved in the same flask. An altered experimental setup was used, utilising a carbon foil slip via the exhaust, to cover and subsequently reveal fresh areas of glass at specific time intervals throughout the deposition. The resultant film achieved samples representing seven different deposition times whilst requiring one deposition in total resulting in significant experimental time saving. The samples were characterised and their functional properties mapped utilising high throughput screening methods. This provided for the first time, insight into the key growth phases

of the material. The technique successfully reproduced the morphology and XRD structure of a TiO_2/ SnO_2 composite material.

X-ray diffraction has shown how the crystal structure develops over time. First a preferentially orientated anatase TiO_2 phase develops and continues to remain the dominant phase throughout the deposition. Concurrently the addition of the [110], [200] and [211] cassiterite SnO_2 peaks from 18 minutes onwards was also observed. XPS demonstrates that from 3 minutes onwards titanium and tin 4+ species are found both at the surface and within the bulk for all samples. Three minutes into the deposition tin is the dominant element relative to titanium, this tin layer is amorphous as no diffraction pattern was observed in XRD. This strongly suggests that the formation of an amorphous tin layer early in the deposition process acts as a seed layer for the growth of the Sn doped TiO_2 solid solution observed from 9 minutes onwards. For this composite material specifically, the tin to titanium ratio remains <1 at both the surface and within the bulk until 18 minutes where the surface ratio of tin to titanium becomes >1. Generally, tin concentration is higher at the surface relative to the bulk regardless of its concentration relative to titanium. Oxygen 1s peaks at 530.1 eV observed within the bulk indicate that a Sn-O-Ti linkage exists within the matrix implicating Sn as a substitutional dopant.[182,183] This indicates that the mechanism for Sn migration is via substitution with Ti atoms within the TiO_2 anatase lattice. SEM shows that the square pyramidal structure observed starts to grow from 9 minutes onwards and increases in size over time; this corroborates band gap analysis, where the band gap starts to decrease towards 3.2 eV and photo-activity where an increase in rate is seen to occur from 9 minutes onwards. The change in morphology seen at 18 and 21 minutes coincides with the inclusion of full cassiterite SnO_2 peaks in the XRD.

Generally, it became apparent from XPS and XRD that an anatase phase solid solution of (Ti / Sn)O_2 forms.[189] From this it is hypothesised that surface segregation, facilitated by heating and time, forces tin to collect at the surface, resulting in the high concentrations of tin found at the surface for all samples, relative to the bulk. Because all samples experience the same temperature inside the reactor, time is the only factor able to account for differences in surface Sn concentration and indeed it is found that; excluding 3-6 minutes, where amorphous SnO_2 is deposited and acts as a seed layer for the composite solid solution phase that grows subsequently, samples which experience longer deposition times are seen in XPS to exhibit higher surface concentrations of Sn, relative to the bulk and other samples with shorter deposition times (Figure 4.13). This explains why the natural formation of a hetero-junction with bulk tin doped TiO_2 and surface SnO_2 is attributed to surface segregation of tin and thus originates from within the original TiO_2 matrix. Its formation is therefore not a direct result of the deposition process. If this were not true, cassiterite SnO_2 XRD peaks would be observed earlier on in the deposition process and would be independent of the surface ratio of tin to titanium found in XPS. Therefore despite having equal amounts of precursor in the aerosol source, SnO_2 nucleates much easier upon the glass substrate and TiO_2 subsequently appears to nucleate much faster than SnO_2 once the amorphous SnO_2 layer has been established. Thermal migration of substitutional Sn, as observed in XPS, through the TiO_2 matrix over time then results in surface segregation of SnO_2. This results in a composite of highly Sn-doped anatase TiO_2 capped by SnO_2.

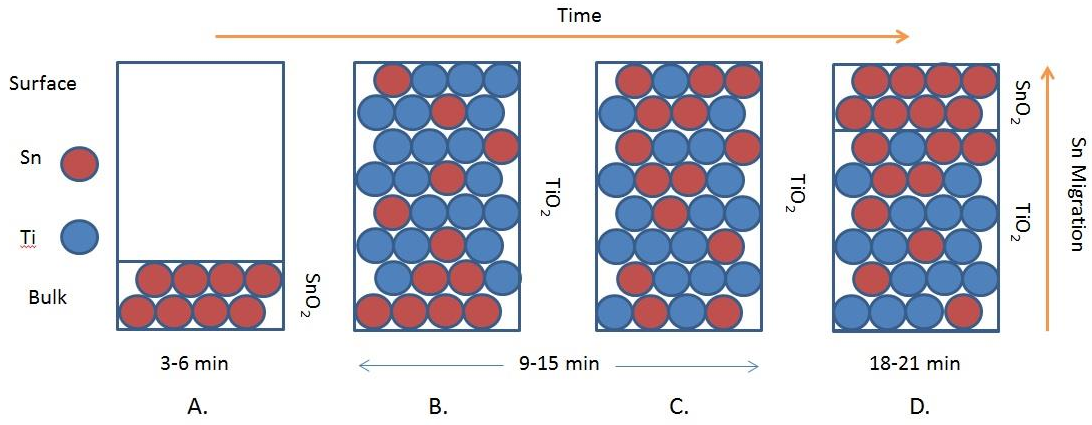

Figure 4.13: A schematic representing samples throughout the deposition process demonstrating how the position and concentration of Sn varies relative to Ti in time. A) Tin dioxide deposits preferentially over titanium dioxide within the first 3-6 minutes B) This initial SnO_2 layer is hypothesised to act as a seed layer allowing a Sn doped TiO_2 layer to develop (9-15 mins). As time progresses Sn begins to migrate to the surface as a result of heating (450 ^{o} C). C) This results in a higher concentration of Sn at the surface than within the bulk (seen in XPS), which is proposed to enhance surface photo-catalysis as the Sn^{4+} sites at the surface act as electron sinks promoting electron lifetimes. D) As time progresses further, Sn concentration becomes so high that it is now the majority element present at the surface (Sn: Ti >1). The surface now converts from an anatase phase Sn doped TiO_2 solid solution to a cassiterite SnO_2 phase which caps the Sn doped TiO_2 solid solution phase from which it originated, this is observed in XRD from 18 minutes onwards. Photo-catalysis is partially impaired by the formation of this SnO_2 layer but still displays a high rate of photo-catalysis.

Ultraviolet-Visible spectroscopy shows, that whilst there was apparent red-shifting of absorption data, transmission was found to decrease proportionally with deposition time. Concordant with tauc plot band gap analysis, demonstrating that the band gap for the final material was 3.2 eV, it was evident that the apparent red-shifting was therefore attributed to increasing film thickness, which was observed to increase incrementally in a linear fashion with increasing deposition time.

Film thickness was observed to increase proportionally with time across all samples, with samples with longer deposition times exhibiting thicker films. This echoes analysis of XPS and XRD. Thus changes in functional properties observed around 15-18 minutes

cannot simply be attributed to the growth of the film and that changes within the film that occur as a result of surface segregation are responsible.

XPS showed that the Sn: Ti ratio switched from <1 to >1, coinciding with the appearance of cassiterite SnO_2 in the XRD, from 15 to 18 minutes can explain how the rate of photo-activity was seen to peak at 15 minutes and proceed to decrease onwards to 21 minutes yet water contact angles exhibit the largest decrease in samples representing 18 and 21 minutes with 15 displaying intermediary behaviour transitions from hydrophobic to hydrophilic behaviour. This discrepancy in behaviour in these specific functional properties, which have their origins in the same underlying principle of photo-generated electrons and holes, is attributed to the formation of SnO_2 at the surface. The method of photo-activity quantification utilised in this report is photo-electron sensitive, hence the enhanced photo-activity observed at 15 minutes and the subsequent decrease after 18 minutes can be attributed to Sn^{4+} states, which act as electron traps at the surface[181], shifting from molecular states existing within the TiO_2 band structure to bulk states inherent in SnO_2 band structure. This results in the sequestration of electrons into the SnO_2 conduction band and hence less electrons are available to carry out reduction of the dye at the surface. This also explains why samples representing 18 and 21 minutes exhibit the biggest change in water contact angle. This is attributed to the same principle, as the mechanism responsible for photo-induced wettability is electron hole sensitive, which creates defect sites which water molecules co-ordinate into, the sequestration of electrons results in the enhancement of electron hole lifetimes and hence enhanced surface defect production.

The sample representing 21 minutes' worth of deposition time displayed FQE and FQY values which appeared to converge where all previous samples demonstrated a marked gap between FQE and FQY. This was attributed to a combination of increasing film thickness, thus a greater cross section for photon absorption and the increasing amount of SnO_2 at the surface which, by sequestering electrons through hetero-junction charge transfer, prolongs electron lifetimes and therefore minimises the recombination process. Therefore it can be deduced that the TiO_2 surface found at 15 minutes was more photo-active but was not as efficient as the sample at 21 minutes because electrons and holes are able to recombine throughout the entire medium. The sample at 21 minutes was a worse photo-catalyst because the surface was becoming more SnO_2 rich so less TiO_2 (and hence Ti^{3+}) sites were available for photo-catalysis but it is now able to sequester electrons at the surface and separate them from holes driving up the efficiency. Another consideration is that the particulates found in SEM at 21 minutes are larger than those observed at 15 and 18 minutes, thus exhibiting a smaller overall surface area. Further experiments would be required to validate this assertion.

4.5 Conclusions

Time-resolved AACVD has successfully provided an insight into the growth profile of a composite metal oxide thin film of technological interest. Although combinatorial AACVD has been successful in determining that the TiO_2 / SnO_2 composite in question displays a complex growth profile, which is not explained by a simple specific elemental ratio, it is unable to provide further mechanistic insight. In this regard TR-AACVD can be considered a success. By varying deposition time, comparison of functional and structural properties and how they change over time has identified intermediate

materials which display functional properties and structure different from the final deposition time whilst also providing mechanistic insight into thin film formation. Thus changes in functional properties relative to each other throughout the deposition sequence can be mapped and as a result the fine tuning of the material can be undertaken for a specific application where different functional properties can be utilised or maximised for specific purposes. The method has succeeded in probing and explaining the formation of the SnO_2 surface layer, which arises from the thermal induced diffusion of Sn through to the film from the bottom to the top. SnO_2 is also key to the formation of the composite acting as a seed layer for the growth of the heavily doped TiO_2 bulk. Whilst used to investigate this particular system, there exists no reason why TR-AACVD cannot provide mechanistic insight, as in combinatorial AACVD, into the growth of a wide range of metal oxide functional materials. It is therefore a novel and highly advantageous form of AACVD.

5 Chapter V: The UV-Induced Surface Segregation of Interstitial Nitrogen and Its Stoichiometric Contribution to the Observed Photo-catalytic Rate in N-TiO_2

5.1 Introduction

The earth receives more energy in a day from solar irradiance than human civilisation is capable of using in a year and is therefore a potent energy source and worthy of utilisation.[190] To this end efforts have been made to tailor materials to absorb and utilise light within the visible region of the electromagnetic spectrum for use in H_2 production,[191] energy efficient window coatings[143] and to drive photo-catalysis for specific applications. One such material investigated is nitrogen doped TiO_2.[109]

Titanium dioxide is a UV active photo-catalyst with a band gap of 3.2 eV and is an area of intense research for use in such applications because of its low cost, low toxicity and high UV activity.[47] TiO_2 once doped with nitrogen is reported to exhibit a shift in band gap toward to the visible spectrum.[109] Thus its utilisation as a visible light photo-catalyst for the remediation of environmental pollutants and the cleaning of water is of intense interest. Since the first synthesis of nitrogen doped TiO_2 many reports have documented visible light photo-activity, where none existed before. However the underlying mechanism for this observed activity has proved an area of intense debate. Many reports attribute the visible light activity to a decrease in band gap and is thus intrinsic to the material itself, representing a true photo-induced exciton mechanism where electrons are promoted to the conduction band from the valence band upon interaction of light with an energy equal to or higher than the band gap of TiO_2 (3.2 eV).[109,192] A

conflicting point of view is that the apparent shift in band gap is due to the introduction of 'colour' states that form between the valence and conduction bands due to the inclusion of nitrogen dopants.[193] This is apparent in many other doped TiO_2 materials and is therefore attributed to oxygen vacancies both within the bulk and the surface.[194,195] Another source of contention surrounds the two forms of nitrogen dopant and which functional properties these dopants are responsible for compared to baseline TiO_2.[196] Interstitial nitrogen doping is reported to enhance UV photo-activity whilst substitutional nitrogen doping is reported to enhance the visible light activity of TiO_2.[197] Recently others have responded that UV photo-activity can be seen to decrease after subsequent irradiation in the process of photo-catalytic testing and that activity decreases proportionally with the irradiation time.[112] This phenomenon is attributed to nitrogen surface species bound to the TiO_2 which are responsible for the observed increase in UV photo-catalysis, which does not represent a true catalytic process whilst observing no visible light photo-catalysis. Thus the actual effectiveness of nitrogen doping is called into question.

Experiments were undertaken to firstly, synthesise for the first time nitrogen doped TiO_2 films by aerosol assisted chemical vapour deposition (AACVD) using a one pot solution, and secondly, provide insight into the discussion surrounding nitrogen doped TiO_2 to see which prior argument found within the literature is evident. AACVD is a versatile technique which allows the use of precursors which traditionally are inaccessible for normal CVD techniques, due to high vapour pressures or relative instability in the presence of oxygen or water, to be utilised for the growth of thin films for technological applications. It is capable of synthesising a wide range of metal oxides which exhibit a wide array of functional properties.

5.2 Experimental

5.2.1 Thin film Preparation using AACVD

Nitrogen (99.99%) (BOC) was used as supplied. Depositions were obtained on SiO_2 coated float-glass. Prior to use the glass substrates were cleaned using water, isopropanol and acetone and dried in air. Glass substrates of ca. 45 mm x 5 mm x 4 mm were used. The precursors, titanium (IV) isopropoxide (99%) and n-butylamine (99%) were obtained from Sigma-Aldrich Chemical Co. and used as supplied. Aerosols were generated in ethanol (99%) and carried into the reactor in a stream of nitrogen gas through a brass baffle to obtain a laminar flow. A graphite block, containing a Whatmann cartridge heater, was used to heat the glass substrate. The temperature of the substrate was monitored using a Pt–Rh thermocouple. Depositions were carried out by heating the horizontal bed reactor to the required temperature of 500 ^{o}C before diverting the nitrogen line through the aerosol and hence to the reactor. The total time for the deposition process took ~40 minutes. At the end of the deposition, under the nitrogen flow, the glass substrates were left to cool to room temperature with the graphite block before it was removed. Two levels of doping were explored with a ratio of nitrogen: titanium of 1:5 (sample $NTiO_2$-20) and 2:1 (sample $NTiO_2$-200), which equated to 0.5 g of titanium (IV) isopropoxide in 20 ml of ethanol with 0.36 and 3.6 ml of n-butylamine for $NTiO_2$-20 and $NTiO_2$-200 respectively.

5.2.2 Sample Characterisation

X-ray diffraction (XRD) was carried out using a Lynx-Eye Bruker X-ray diffractometer with a mono-chromated Cu Kα (1.5406 Å) source. X-ray photoelectron spectroscopy (XPS) was carried out using a Thermo Scientific K-Alpha instrument with monochromatic Al-

Kα source to identify the oxidation state and chemical constituents. High resolution scans were done for the Ti (3d), N (1s), O (1s) and C (1s) at a pass energy of 40 eV. The peaks were modelled using Casa XPS software with binding energies adjusted to adventitious carbon (284.5 eV). SEM images were taken on a JEOL JSM-6301F Field Emission instrument with acceleration voltage of 5 kV. Images were captured using SEMAfore software. Samples were cut into coupons representing the different timed samples and coated with a fine layer of gold to avoid charging. The optical transmission was measured over 320–800 nm range using a Lamda 950 UV/Vis spectrometer.

5.2.3 Functional Property Testing

Visible light induced photo-catalytic activity was assessed using an established method based on the hydroxyl radical induced mineralisation of stearic acid and UV photo-activity was assessed via the reduction of a resazurin dye. Samples were dip coated into a stock solution of stearic acid in chloroform at a rate of 60 cm/minute, one side was wiped clean and the sample mounted on an aperture to facilitate irradiation and IR spectroscopy. The resazurin based ink was evenly applied using a spray gun and the photo-induced degradation of the resazurin ink monitored by UV-Vis spectroscopy. Formal quantum efficiency and the formal quantum yield was then calculated. Formal quantum efficiency was calculated by dividing the rate of dye molecules destroyed per s per cm^2 by the photon flux (4.53×10^{14} photons per cm^2 per s). The photon flux and photon absorption for each film was determined using a UVX digital radiometer with a detector for 365 nm radiation attached.

5.3 Results

Nitrogen doped TiO_2 films were synthesised by AACVD using titanium (IV) isopropoxide as the Ti precursor and n-butylamine as the nitrogen source dissolved in neat ethanol in a singular flask. The deposition was carried out at 500 ^oC at a N_2 flow rate of 1l/min until the aerosol precursor solution was exhausted. A non-doped TiO_2 sample was also deposited in the same way by excluding the nitrogen precursor from aerosol precursor solution to create a control film identical in surface morphology and growth conditions. This allowed a true comparison of nitrogen doping between the N doped samples and non-doped sample.

5.3.1 Characterisation and Functional Properties

Initially many different ratios of doping were tried (N%: 2, 5, 10, 20 and 200), but detectable nitrogen doping levels were only observed for N: Ti molar ratios of 1:5 (20% N: Ti) and 2:1 (200% N: Ti). Nitrogen doping levels were observed to plateau regardless of nitrogen precursor concentration relative to the titanium precursor suggesting a ceiling of solubility for nitrogen within the bulk for this particular precursor system. This insolubility of nitrogen within a TiO_2 matrix is reflected in previous studies.[198,199] This is discussed further in XPS, and for this reason this study focuses solely on a standard TiO_2 sample and two nitrogen doped samples which exhibit an N: Ti molar ratio of 1:5 (20%) and 2:1(200%). These samples will be referred to as $NTiO_2$-20 and $NTiO_2$-200 respectively. This chapter aims to characterise the nitrogen doped films and compare the irradiation induced change in nitrogen surface species with the observed rate of photo-catalysis and transient absorption spectroscopy studies to provide insight into the role of nitrogen within TiO_2.

5.3.1.1 X-ray Diffraction (XRD)

X-ray diffraction was undertaken to identify the crystal structure of the resultant films, and to see if any change in crystal structure resulted from nitrogen doping. The anatase crystal structure was observed for the standard TiO_2 sample and, similar to many previous reports,[200] this crystal structure was preserved in the nitrogen doped samples (Figure 5.1). This is attributed to nitrogen, either as a substitutional or interstitial dopant, having an ionic radius small enough to not cause expansion of the anatase crystal lattice. The diffraction patterns also display little apparent preferential orientation, which is common for doped TiO_2 thin films synthesised by AACVD.

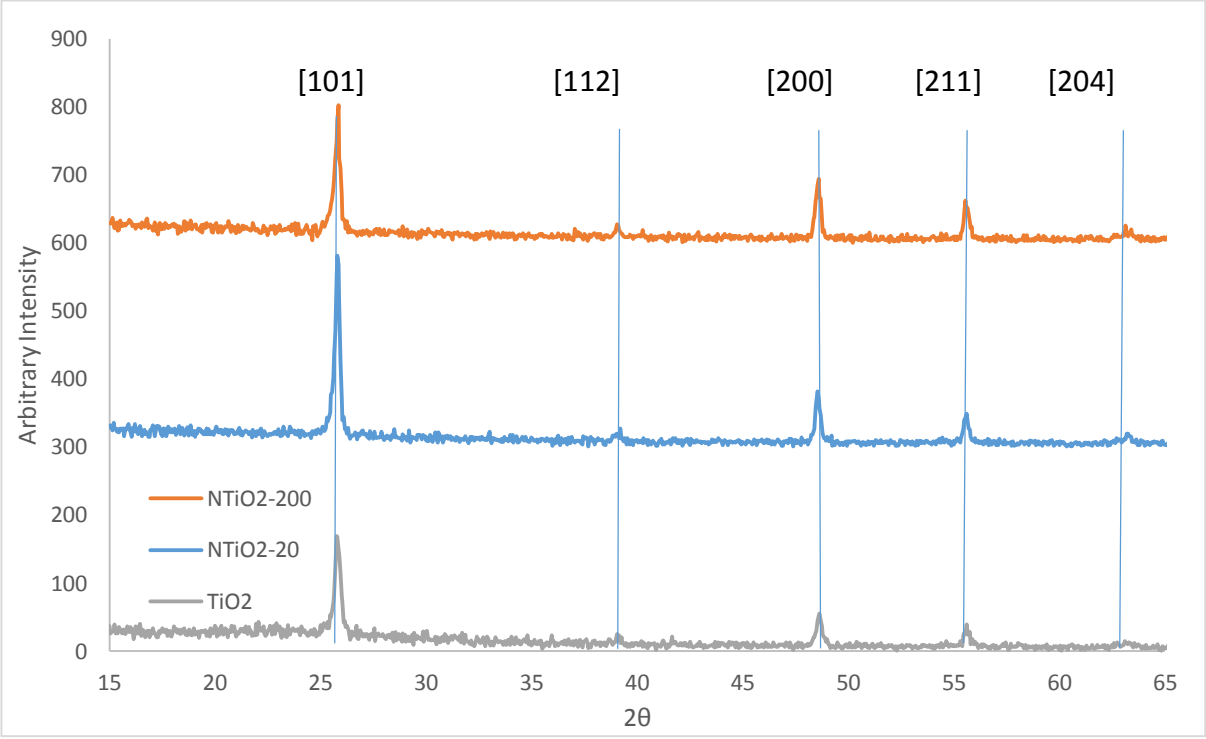

Figure 5.1: XRD of TiO_2, N-TiO_2-20 and NTiO_2-200 films grown by AACVD at 500 °C. The anatase TiO_2 crystal phase is observed for all samples. No shifting of peaks is observed which corroborates previous literature reports which show that nitrogen, either as a substitutional or interstitial dopant within the TiO_2 matrix does not cause changes in the crystal lattice parameters of the host material.[200]

5.3.1.2 X-ray Photoelectron Spectroscopy (XPS)

X-ray Photoelectron Spectroscopy (XPS) was undertaken to identify the oxidation state, identity and concentration of titanium, oxygen and nitrogen relative to each other in all samples. Ti^{4+} species indicative of TiO_2 were found in all samples with characteristic binding energies of 458.7 eV and 464.37 eV for the $2p_{3/2}$ and $2p_{1/2}$ peaks respectively. Oxygen 1s peaks, characteristic of TiO_2 were found at expected binding energies too for all samples. Specifically a Ti-O-Ti linkage at 530.1 eV was seen, as well as a Ti-OH surface linkage at 532.0 eV. At the surface nitrogen was detected, in both $NTiO_2$-20 and $NTiO_2$-200 samples, at characteristic binding energies in the form of interstitial dopants and nitrogen surface species, such as chemisorbed N_2 and NH_x.[112] Nitrogen was detected within the bulk at characteristic binding energies in the form of both substitutional (~396.8 eV) and interstitial (~399.1 eV) species in the nitrogen doped samples. Interstitial N doping was found to be the dominant form however within the bulk (Figure 5.2).

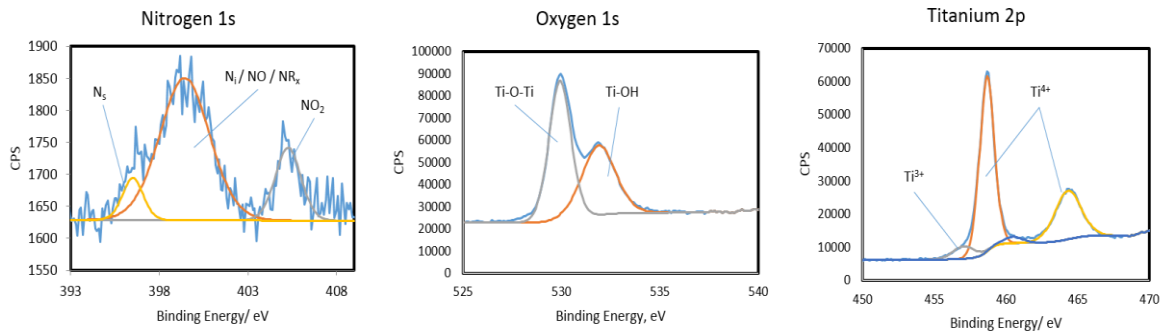

Figure 5.2: Sample XPS spectra for nitrogen, oxygen and titanium in nitrogen doped TiO_2. Nitrogen: at the surface both Substitutional and interstitial nitrogen is observed (397 and 400 eV respectively). NO_2 is also observed at the surface but not within the bulk. Surface oxygen shows Ti-O-Ti and Ti-OH species whilst within the bulk only Ti-O-Ti is observed. Titanium shows both Ti^{4+} and Ti^{3+} species at the surface with the Ti^{3+} peak reduced in intensity within the bulk.

XPS depth profiling was undertaken to understand how the relative concentrations of nitrogen species varied from the surface to the bulk. It was observed that regardless of the concentration of nitrogen precursor used in the aerosol source, the concentration of nitrogen remained roughly constant in the bulk (Figure 5.3). However, at the surface the concentration of nitrogen species was higher for $NTiO_2$-200 which correlates with the higher concentration of nitrogen precursor present in the synthesis of the film.

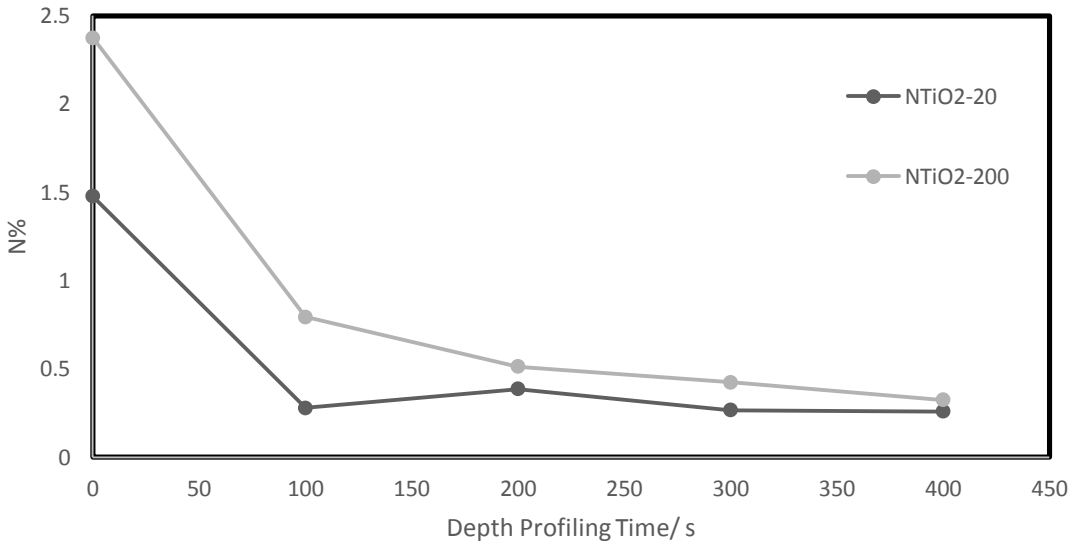

Figure 5.3: XPS depth profiling shows that the concentration profile of nitrogen relative to titanium at the surface is much higher compared to within the bulk. In the bulk (after >200s of sputtering) nitrogen concentrations remain roughly constant ranging from 0.3-0.7%. Just below the surface the concentration of nitrogen raises to between 0.3-0.8%. The elevated concentration of nitrogen at the surface is to be ~1.5% ($NTiO_2$-20) and ~2.4% ($NTiO_2$-200).

In light of previous work on nitrogen doped TiO_2 thin films grown by APCVD[112] an irradiation study was carried out to see how nitrogen surface concentration varied following irradiation of the films by 365 nm UV light. Each sample was irradiated for 24 hours and washed with water; this process was repeated for a total of 28 days to create samples representative of 0, 4, 7, 12, 14, 18, 21, 25 and 28 days' worth of UV irradiation.

XPS depth profiling was done for all samples to chart how the concentration of nitrogen surface and bulk species changes as a function of irradiation time (Figure 5.4).

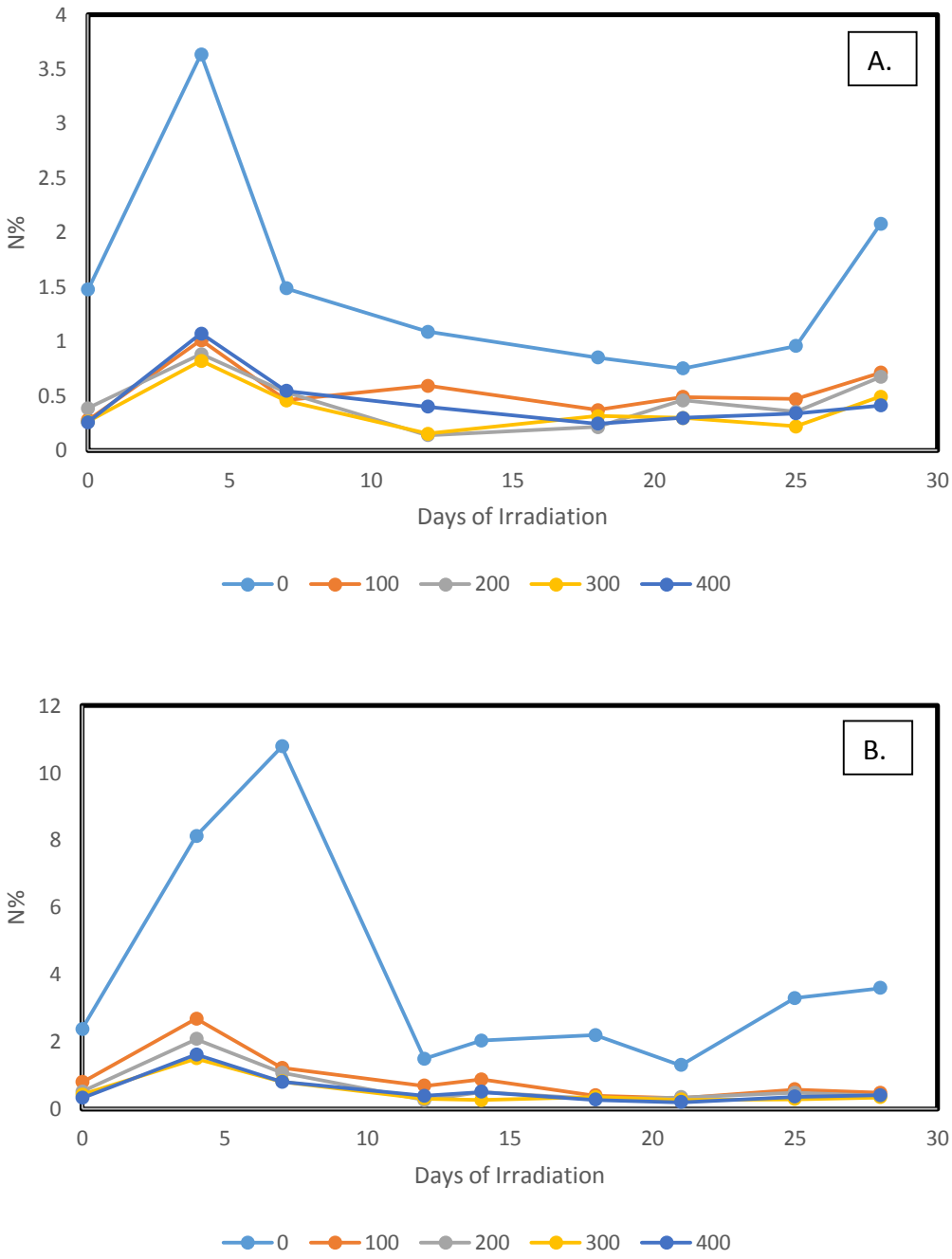

Figure 5.4: A) A graph showing how nitrogen levels vary after varying levels of sputtering (0, 100, 200, 300 and 400 s, with 0 s representing the surface and 400 s representing the bulk) over the course of 28 days of irradiation at 365nm for $NTiO_2$-20. Nitrogen surface concentration is found to increase over time at both the surface and within the bulk until after 7 days at which point it is found to drop back to pre-irradiation levels. B) A graph showing how nitrogen levels vary from the surface through two layers of sputtering over the course of 28 days of irradiation at 365nm for the $NTiO_2$-200. Nitrogen surface concentration is found to increase over time at both the surface and within the bulk until after 7 days at which point surface nitrogen concentration is found to drop back to pre-irradiation levels.

It was found in both samples, $NTiO_2$-20 and $NTiO_2$-200, that nitrogen surface concentration increases proportionally with irradiation time between 0-4/7 days until it is then seen to decrease dramatically and remain roughly constant for the rest of the irradiation time. The increase in surface nitrogen species was observed to be roughly proportional to the amount of nitrogen the sample was doped with, with the $NTiO_2$-200 sample exhibiting a higher degree of nitrogen surface segregation. This phenomenon was also observed within the bulk, which suggests that the process of activation of the TiO_2 by UV irradiation is in some way causing the nitrogen within the bulk to collect at the surface. This mirrors reports that nitrogen as an interstitial dopant is labile whilst incorporated into a TiO_2 lattice and that the dopant in its interstitial state is capable of migrating from one site to another over time. [198,199]

Interestingly the surface Ti-O-Ti:Ti-OH ratio, as observed in oxygen 1s XPS was seen to increase, peak between 4-7 days of irradiation and then fall to initial concentrations where levels proceed to plateau (Figure 5.5). The significance of this will be discussed later in light of other analysis. It however appears that the increase in hydroxy surface species is linked to nitrogen concentrations at the surface.

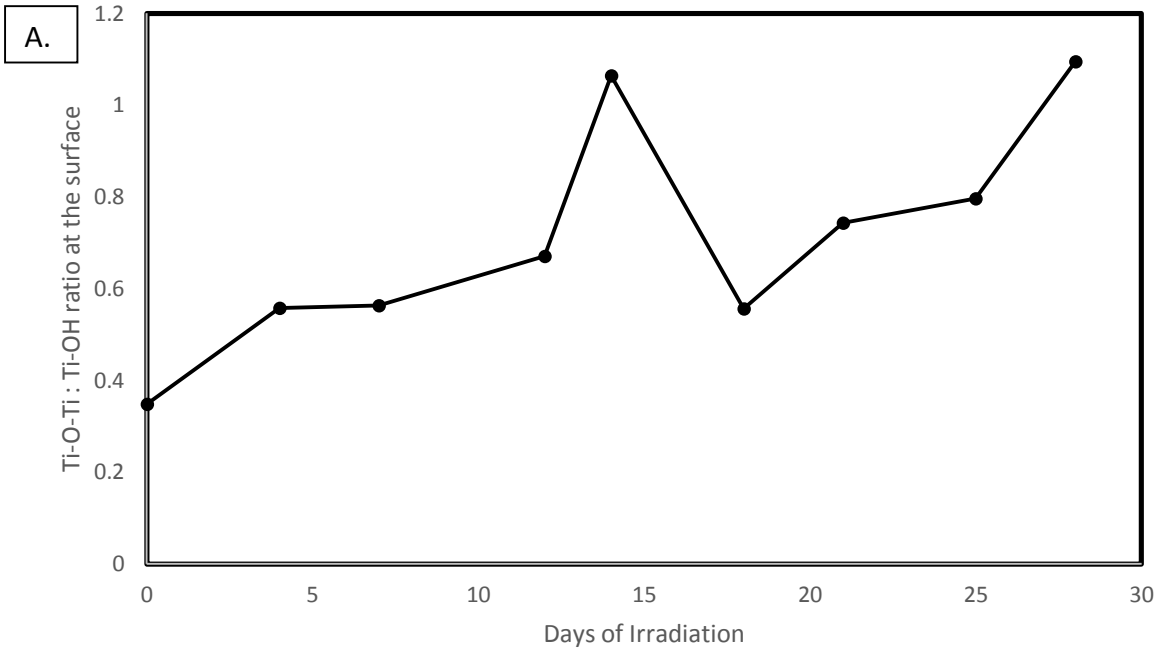

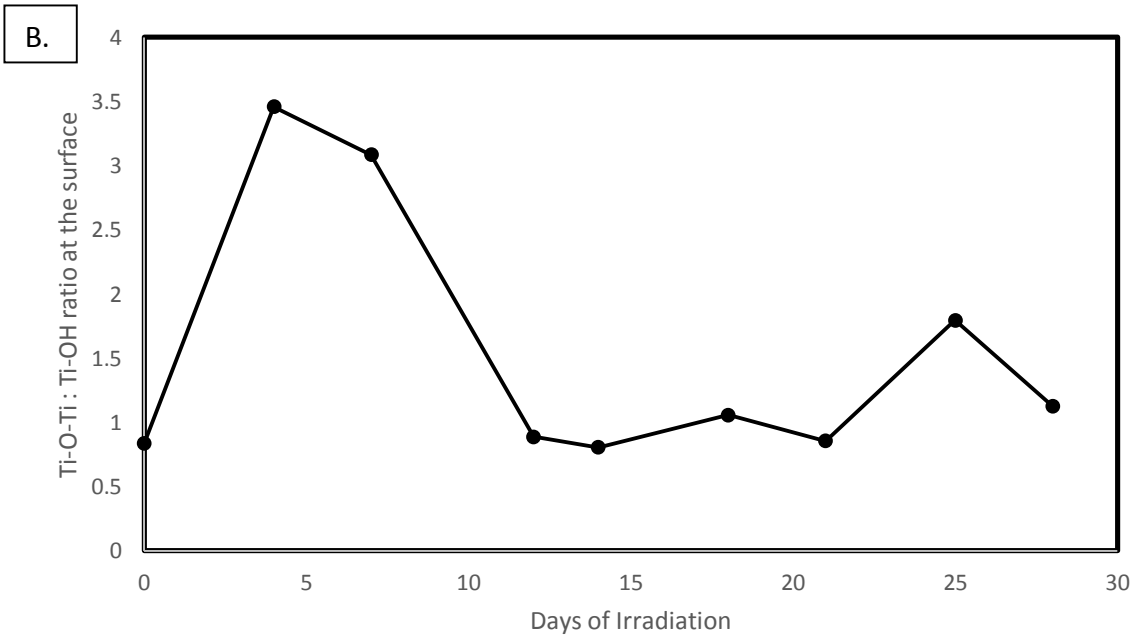

Figure 5.5: Graphs demonstrating the ratio of oxygen in surface hydroxyl species compared to Ti-O-Ti oxygen species. A. for $NTiO_2$-20 the ratio is slowly seen to increase as radiation time increases. B. $NTiO_2$-200 demonstrates a marked increase in the surface ratio of Ti-OH compared to Ti-O-Ti oxygen species. This is very similar in nature to the surface concentrations of nitrogen seen for the same amount of irradiation time.

5.3.1.3 Scanning Electron Microscopy (SEM)

Scanning Electron Microscopy was undertaken to see how the process of nitrogen doping affected surface morphology, this is important to consider because surface morphology has a significant impact upon functional properties. Features such as porosity, surface area and exposed crystal faces can affect the observed rate of photo-catalysis. The standard non-doped TiO_2 sample exhibits a high surface morphology consisting of upright thin plates. The nitrogen doped samples both exhibit similar morphologies, with the surface covered in 'shark tooth' like growths with some of the plates appearing to be lying on their side (Figure 5.6). As the morphologies are relatively similar the importance of morphology is reduced and the effect of nitrogen doping can be considered more important when comparing differences in functional properties. Figure 5.6 also details SEMs of each sample after 28 days of irradiation at 365 nm. TiO_2 exhibits expected surface roughening caused by exciton generation. The nitrogen doped samples however do not exhibit this surface roughening and display intact morphologies which show none of the micro cracks exhibited by the pristine TiO_2 sample. This irradiation was done to chart how elemental composition and photo-activity changed as a result of irradiation which is discussed in later sections.

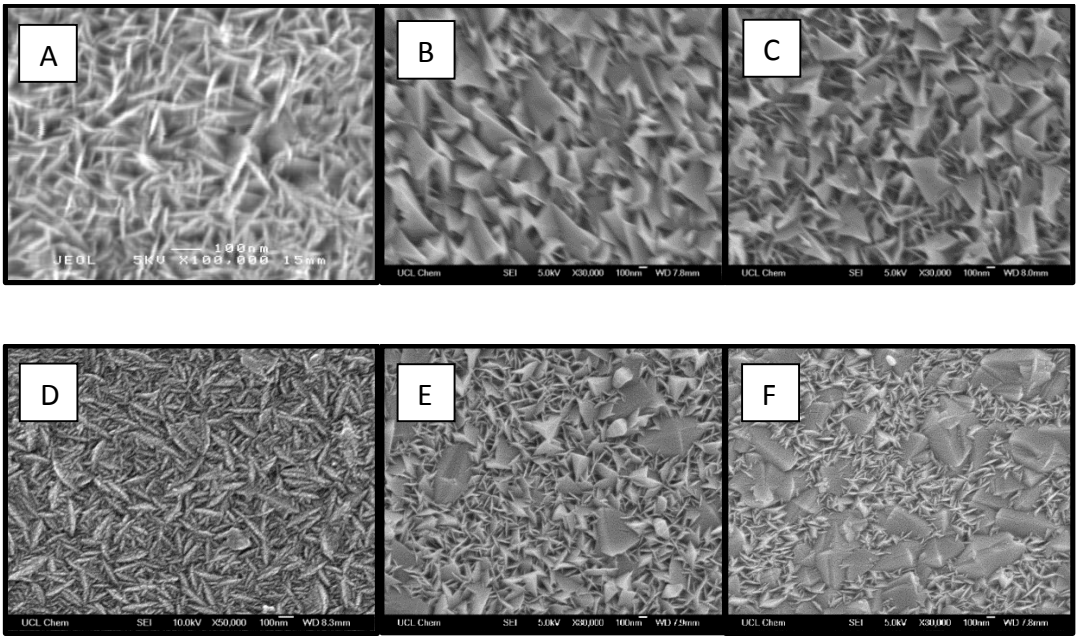

Figure 5.6: SEM of TiO_2, $NTiO_2$-20 and $NTiO_2$-200 films grown by AACVD at 500 ° C. A) Needle like structures are observed in the standard TiO_2 sample, replicating previous reports (X 100,000 magnification). B-C) The nitrogen doped samples, exhibit the sample surface morphology, with the addition of 'shark tooth' like structures on the surface (x 30,000 magnification). D-F) TiO_2, $NTiO_2$-20 and $NTiO_2$-200 samples were irradiated for seven days to observe the effect irradiation has upon surface morphology. TiO_2 (D) exhibits fracturing which could be attributed to hole induced surface roughening. $NTiO_2$-20 (E) and $NTiO_2$-200 (F) exhibit little change in surface morphology.

5.3.1.4 UV-Visible spectroscopy

Ultraviolet- Visible transmission spectroscopy demonstrates a significant red-shifting of the absorption edge for the nitrogen doped materials compared to the un-doped TiO_2 sample (Figure 5.7). The TiO_2 sample exhibited a calculated band gap of 3.22 eV which is indicative of anatase TiO_2. The red-shifted band gaps for the nitrogen doped samples both display band gap values of 2.51 eV which is similar to previous reports of nitrogen doped TiO_2 (Table 5.1). Both nitrogen doped films themselves exhibit a yellow to orange colour which confirms on a qualitative level that the absorption edge for these materials now interacts in some way with visible light.

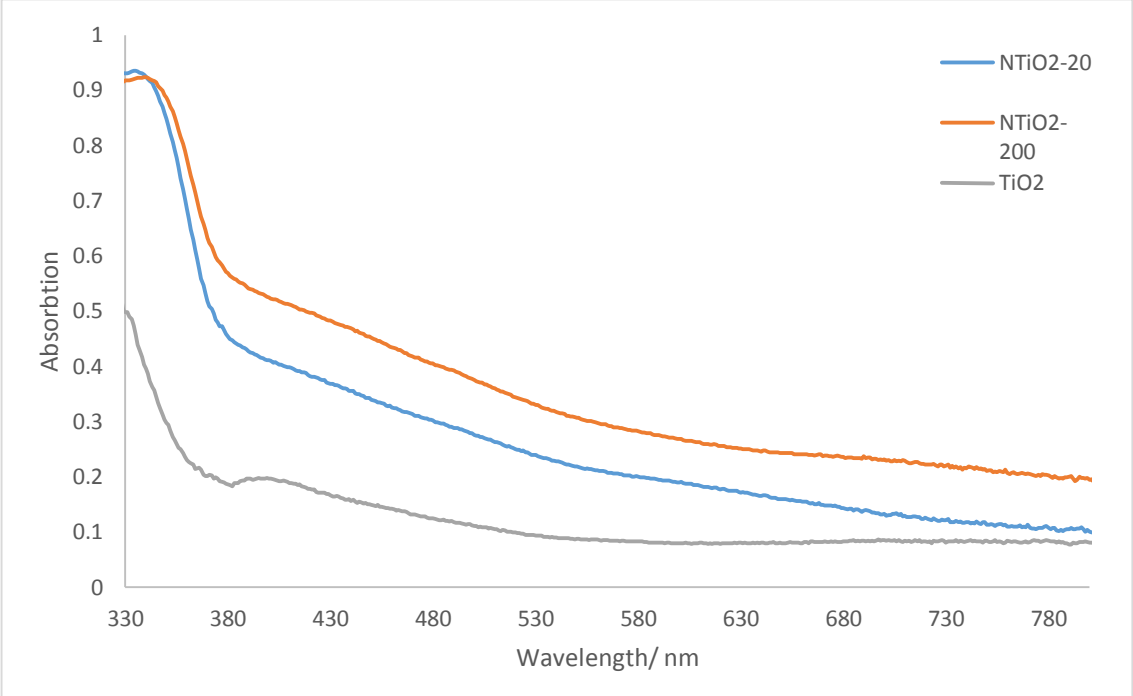

Figure 5.7: Ultraviolet-Visible transmission spectroscopy for TiO_2, $NTiO_2$-20 and $NTiO_2$-200 films grown by AACVD at 500 °C. There is an apparent red-shifting of the absorption edge for the nitrogen doped samples.

Table 5.1: A table for all samples displaying; the precursors for each deposition, the initial solution N: Ti molar ratios, the observed N : Ti ratios within the bulk and at the surface and the band gap values calculated using tauc plot analysis.

Sample	Ti Source	N Source	Initial N %	Bulk N %	Surface N %	Bandgap/ eV
TiO_2	TTIP	-	-	-	-	3.22
$NTiO_2$-20	TTIP	N- Butylamine	20	0.3	1.5	2.51
$NTiO_2$-200	TTIP	N-Butylamine	200	0.5	2.4	2.51

5.3.1.5 Photo-catalysis

An observed enhancement of UV photo-catalysis in nitrogen doped thin films by Cabrera *et al*[112] has been attributed to a stoichiometric oxidation of stearic acid by nitrogen surface species rather than by pure photo-catalysis, which upon conversion to nitrate species proceed to hamper photo-activity. Subsequent washing of the samples with water was shown to remove the nitrate species from the surface, partially restoring the

previous observed rate of UV photo-catalysis. After long periods of irradiation the surface concentration of nitrogen species was seen to decrease until no further change occurred and photo-activity was observed to be roughly the same as non-doped TiO_2. Hence any 'observed' enhancement in UV photo-catalysis is attributed purely to a stoichiometric process separate from UV induced semiconductor photo-catalysis.

An effort to see if a similar effect is observed with nitrogen doped TiO_2 thin films produced by AACVD was thus undertaken. The previous study contradicts a large volume of the established literature, thus reproducibility of this phenomenon is important. The individual films were cut into 1 cm^2 coupons to allow for samples representing 0, 4, 7, 12, 14, 18, 21, 25 and 28 days' worth of 365 nm UV irradiation to be created, as done previously in XPS. All samples were irradiated for 24 hours and then washed with deionised water to remove nitrate surface species. This was repeated as necessary to obtain the correct amount of irradiation time.

All samples were tested using a previously established photo-catalytic test based on the reduction of a resazurin based dye.

Visible light photo-catalysis was also tested by utilising a previously established method involving stearic acid.

5.3.1.6 UV Photo-catalysis

Photo-catalytic testing was done for all samples by charting the reduction of a resazurin dye to resorufin.[168] All samples were irradiated for the number of days stated and washed every 24 hours during this period with deionized water to remove surface nitrate species. It was observed that all samples exhibited similar rates of photo-catalysis before irradiation, however as irradiation time increases the nitrogen doped

samples exhibited increased rates of photo-catalysis proportional to the amount of irradiation it has been subjected to (Figure 5.8). The nitrogen doped samples were therefore exceptional photo-catalysts for the reduction of pollutants on the surface. However in the light of XPS it was apparent that the increase in photo-catalytic activity observed in the photo-induced reduction of resazurin coincides with increasing levels of interstitial nitrogen on the surface, and it is postulated that N^{3-} is contributing electrons to the dye and thus stoichiometrically adding to the base rate of photo-catalysis observed in non-doped TiO_2. Finally TiO_2 was seen to decrease in photo-activity after 7 days of irradiation, this is attributed to hole-induced surface roughening, which may result in a decrease in crystallinity and quality of surface morphology. This is corroborated by SEM which displays a fracturing of the TiO_2 morphology after irradiation, whilst the nitrogen doped samples exhibit no roughening effects.

Table 5.2: Photo-catalytic rates of all samples with differing 365 nm irradiation times.

Sample	Photo-catalytic Rate / no. of molecules destroyed s^{-1} cm^{-2}			
	0 days	2 days	6 days	7 days
TiO_2	1.66E+13	4.34E+12	1.67E+12	3.25E+11
$NTiO_2$-20	1.66E+13	2.68E+13	1.7E+13	3.32E+13
$NTiO_2$-200	2.4E+13	3.6E+13	3.59E+13	8.77E+13

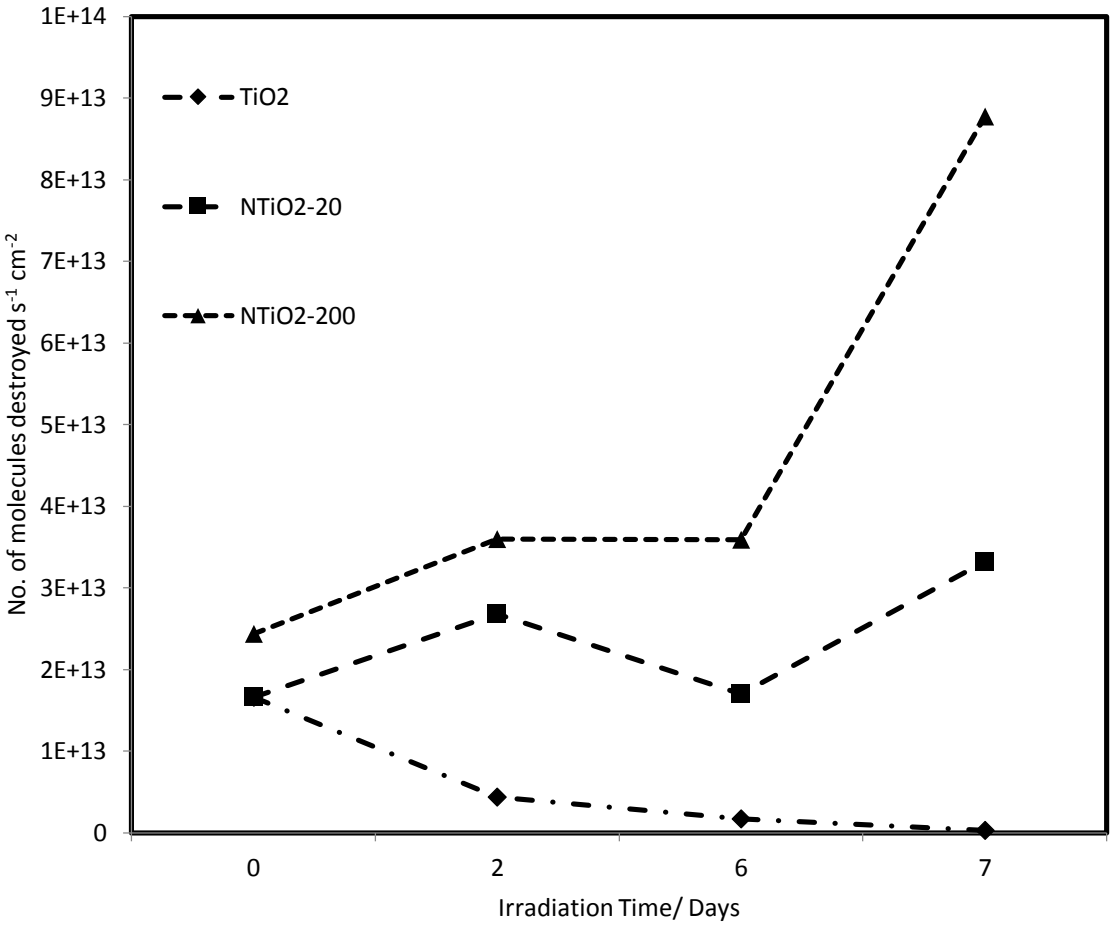

Figure 5.8: A graph showing photo-catalytic rates generated from the resazurin dye test for each sample (TiO_2. $NTiO_2$-20 and $NTiO_2$-200). The nitrogen doped samples are seen to get better as irradiation time increases, proportional in some way to nitrogen concentration, whereas TiO_2 is seen to get worse.

5.3.1.7 Visible Photo-catalysis

Photo-catalysis was undertaken to ascertain the degree of activity present in the non-doped and nitrogen doped TiO_2 samples when exposed to visible light. Samples were tested using the same standard photo-catalytic test which employs stearic acid and follows the degradation via IR measurements as done for UV induced photo-catalysis. Samples were irradiated overnight using a custom setup which delivered irradiation equivalent to one sun's worth of irradiation. A filter was applied with a cut off at 420 nm ensuring that no UV was irradiating the sample. There was no significant visible light

activity for all samples. For TiO_2 this is to be expected. For the nitrogen doped TiO_2 samples this is contradictory to many studies which observe visible light induced photo-catalysis. Possible explanations for this are discussed later in the light of other experiments.

5.3.1.8 Transient Absorption Spectroscopy (TAS)

Transient absorption spectroscopy (TAS) was performed on all samples. Transient absorption spectroscopy involves the excitation of the material using a 6 ns pulse from a 355 nm 'pump' laser. The formation and lifetime of excited electrons and holes is then charted by measuring the absorbance of the sample at specific wavelengths. Due to the electrons and holes forming molecular states within the bulk from which they originate they exhibit a HOMO and LUMO. A 'probe' wavelength is able to excite electrons from the valence band into the LUMO of the hole or an electron from the HOMO of the photo-generated electron to the conduction band. In pristine TiO_2 this is 500 nm for holes and 700 nm for electrons.[160,201] The decay in these absorption signals can be charted and the lifetime of photo generated electrons and holes inferred from the kinetics of this process. For nitrogen doped TiO_2, which exhibits a shifting of the bandgap (specifically a raising of the conduction band) a probe wavelength of 650 nm is utilized to chart the absorption decay. There is one previous study which reports TAS for nitrogen doped TiO_2, thus it remains a novel spectroscopic method for the investigation of $NTiO_2$.[202] By measuring the differences in recombination rates or lifetime of charge carriers and overall charge carrier generation per absorption further insight into the bulk material can be ascertained, allowing comparison between the observed effects of UV irradiation

at the surface in photo-catalytic studies and what is actually happening within the bulk upon UV irradiation.

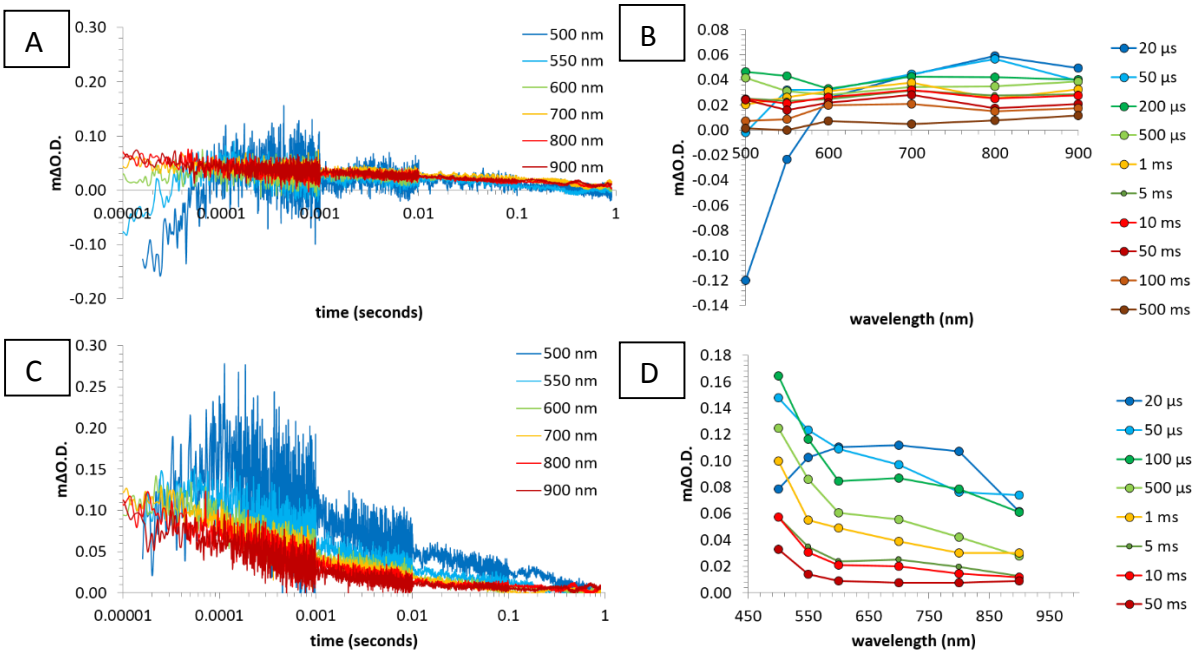

Figure 5.9: Graphs A and C plot exciton absorption (mΔO.D) against constituent lifetimes (s) for specific wavelengths. Graphs B and D plot exciton absorption (mΔO.D) at specific wavelengths (nm) at specific time intervals. A. hole and electron lifetimes for $NTiO_2$-20 before 28 days of irradiation. The sample exhibits bleaching at 500-550nm. B. Lifetime charted for specific wavelengths show the pronounced effect of the bleach present in the first 20 µs and is seen to recover from 50 µs onwards. C-D. The experiments were repeated after the sample was irradiated for 28 days. The bleach signal is seen to decrease significantly.

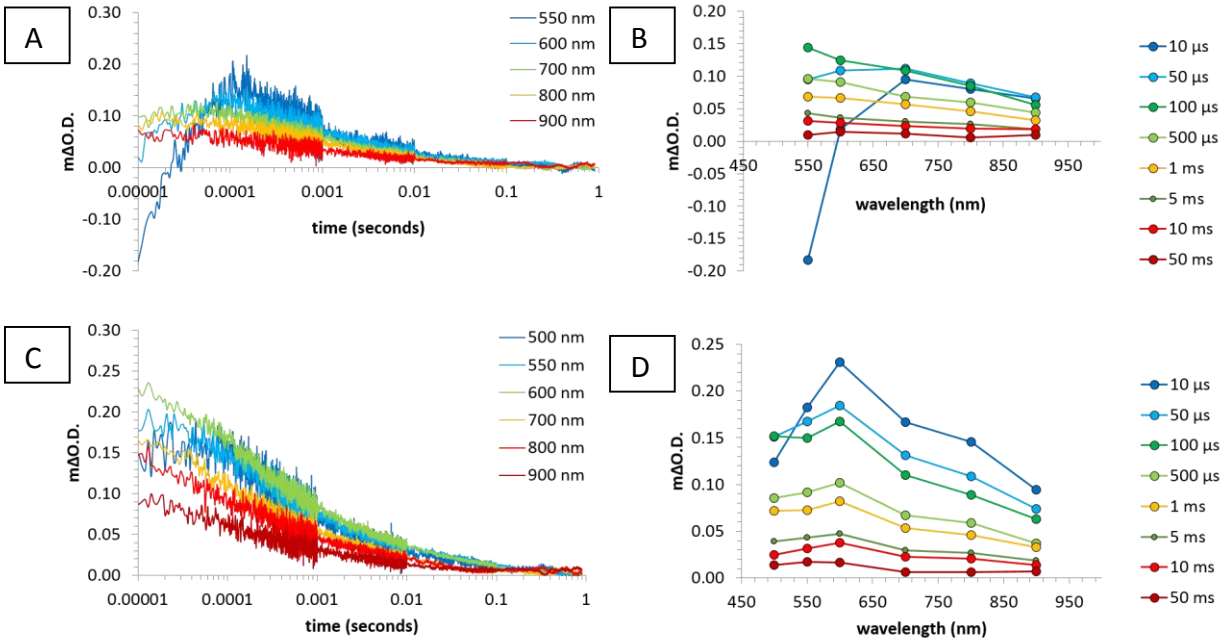

Figure 5.10: Graphs A and C plot exciton absorption (mΔO.D) against constituent lifetimes (s) for specific wavelengths. Graphs B and D plot exciton absorption (mΔO.D) at specific wavelengths (nm) at specific time intervals. A. hole and electron lifetimes for $NTiO_2$-200 before 28 days of irradiation. The sample exhibits bleaching at 500-550nm. B. Lifetime charted for specific wavelengths show the pronounced effect of the bleach present in the first 20 µs and is seen to recover from 50 µs onwards. C-D. The experiments were repeated after the sample was irradiated for 28 days. The bleach signal is seen to decrease to insignificance.

Transient absorption spectroscopy studies have demonstrated that both $NTiO_2$-20 and $NTiO_2$-200 both exhibit a bleach signal (Figures 5.9 and 5.10), where the sample absorbs large amounts of the probe laser for around 20-50 µs before the signal is seen to recover. After 28 days of irradiation the bleach signal appears to be significantly reduced or gone in both $NTiO_2$-20 and $NTiO_2$-200. This indicates that whatever is responsible in the nitrogen doped TiO_2 samples for the Initial bleach signal observed at 500-550 nm is removed by the process of irradiation. This is discussed later in context of XPS studies. Interestingly, the charge carrier generation concentration at 20 and 100 µs for both $NTiO_2$-20 and $NTiO_2$-200 before irradiation and post irradiation remain fairly similar with only a slight increase observed as a result of irradiation, however it can be considered

that no real overall change in charge carrier concentrations occur pre and post irradiation (Table 5.3). Thus nitrogen doping confers little enhancement in charge carrier concentration compared to a TiO_2 sample, regardless of irradiation, whilst a marked increase in the observed rate of photo-catalysis was observed in the resazurin test. The half-life of charge carriers was seen in fact to decrease in nitrogen doped TiO_2 samples post irradiation indicating that nitrogen impurities acted as trap states and thus the expected rate of photo-catalysis should decrease after removal by irradiation observed in XPS. That the observed rate of photo-catalysis was seen to increase as a function of irradiation indicates that something more than just charge carriers generated from UV irradiation is responsible for the increased rate of photo-catalysis.

Table 5.3: Charge carrier lifetimes at 20 and 100 µs and half-lives for each sample.

	$NTiO_2$-200, non-irradiated (900 nm)	$NTiO_2$-200, irradiated (900 nm)	$NTiO_2$-20, non-irradiated (900 nm)	$NTiO_2$-20, irradiated (900 nm)	TiO_2, not-irradiated (900 nm)
20 µs	6.78E-02	8.46E-02	4.92E-02	6.16E-02	9.55E-02
100 µs	5.61E-02	6.31E-02	4.42E-02	6.13E-02	7.93E-02
$t_{50\%}$ (ms)	2.0	0.78	20	0.75	2.7

5.4 Discussion

Nitrogen doped TiO_2 thin films have been grown by AACVD for the first time. The films were compared to a non-doped TiO_2 sample and characterised by XRD, XPS, SEM, UV-Visible transmission spectroscopy and their functional properties charted via UV and visible light induced photo-catalysis. Transient absorption spectroscopy was employed as a relatively new technique to this area of discourse to chart the lifetime of excitons

in the non-doped and nitrogen doped samples.[203,204] This has allowed the analysis of nitrogen doped TiO_2 films with methods not usually accessible for powders whilst demonstrating AACVD's ability to reproduce a growing range of materials as it increases in industrial significance.

The nitrogen doped species exhibit anatase crystal structure, equivalent in nature to non-doped TiO_2 with no significant shifting or broadening of diffraction peaks, signalling that, if nitrogen is present it is small enough not to affect the overall crystal structure in terms of lattice size, corroborating previous reports.[205] X-ray photoelectron spectroscopy shows that expected Ti^{4+} species found in TiO_2 were observed in all samples at the correct binding energy of 458.7 eV and 464.37 eV for Ti^{4+} $2p_{3/2}$ and Ti^{4+} $2p_{1/2}$ respectively. The same was observed for oxygen 1s peaks at 530.1 eV and 532 eV for Ti-O-Ti and Ti-OH linkages respectively. Both interstitial (~399 eV) and substitutional (~396 eV) nitrogen dopants were observed within the bulk, with interstitial states being the dominant form. Relatively ambiguous nitrogen surface species such as NH_x, NO, N_2 and surface interstitial states N^o were responsible for the peak observed at ~400 eV in XPS. Literature reports however show that dinitrogen is not chemisorbed to metal oxide surfaces at room temperature.[121] NH_x species are proposed mostly in studies in which ammonia is the nitrogen source. In this case, as the nitrogen source is n-butylamine, in place of NH_x the nitrogen species is proposed as NRH_x to account for the possible carbon chain. Another possibility is the formation of NH_x species from NRH_x species via beta hydride elimination reactions. Thus it can be reasoned that the four most likely surface species are nitrogen interstitials (N^o), NO, NH_x and NRH_x species. However the process of irradiation and subsequent washing of these samples will remove initial NH_x and NRH_x

species. As such the two most likely nitrogen surface species found at ~400 eV in XPS are nitrogen interstitials and bound NO species.[113,119,122]

SEM demonstrates that pristine TiO_2 and both the $NTiO_2$-20 and $NTiO_2$-200 samples exhibit roughly similar high surface area morphologies and porosities. All samples exhibit sharp needle like growths that suggest a degree of homogenous gas phase degradation of the TiO_2 precursor into particulates which become immobilised upon the surface resulting in a high surface area film.[147] All samples exhibit a degree of hole induced surface roughening[206] after prolonged periods of irradiation, which means changes in surface area and loss of crystallinity that result from this process can be said to not affect the observed rate of photo-catalysis if it deviates between samples. As the morphology is similar between samples it can also be argued that differences in photo-activity do not arise from differences in surface area.

UV-Visible transmission spectroscopy suggest that the bandgap is redshifted in the nitrogen doped TiO_2 samples (2.51 eV) compared to pristine TiO_2 (3.2 eV) mirroring previous reports for interstitially doped N-TiO_2.[109,196,199] This is confirmed on a qualitative level with the films exhibiting a yellow hue. In light of work done by Serpone *et al*, this colour could also be attributed to the production of 'colour centres' that sit between the valence and conduction band and form regardless of dopant.[193]

Previous work has highlighted the importance of surface species and how these relate to the functional properties observed. Cabrera *et al* demonstrated that the presence of relatively ambiguous nitrogen surface species, identified previously as chemisorbed N_2, NH_x and interstitial N^o, resulted in an observed increase in the rate of UV photo-catalysis.[112] Subsequent UV irradiation was shown to cause a decrease in the

concentration of these surface species in XPS. This was observed to correlate positively with a decrease in UV activity of the nitrogen doped thin films from an original position of enhanced UV photo-catalysis compared to non-doped TiO_2 to a state of equivalence with non-doped TiO_2. The initial enhancement of UV photo-catalysis observed could be attributed to a combination of the photo-catalytic generation of redox mediator species by TiO_2 (e^- and h^+) coupled with a stoichiometric process where surface species contributed to the mineralisation of surface contaminants.

In this work experiments were done to corroborate these findings as the original ones contradict the prevailing consensus within the literature by exhibiting a photo-catalytic enhancement in the UV range whilst exhibiting no activity in the visible range for stearic acid despite exhibiting apparent band gap values in the visible range (2.4-2.6 eV).

Transient absorption spectroscopy (TAS) was undertaken for the nitrogen doped samples pre and post irradiation (28 days, UVA). This demonstrates that the charge carrier generation rates for both pristine TiO_2 and N-doped TiO_2 before irradiation are roughly the same whilst the process of irradiation significantly decreases the half-life of photo-generated charge carriers. Thus any distinct observed differences in photo-activity between samples, which cannot be attributed to surface area or hole induced surface roughening or a dopant contribution, must be due simply to a stoichiometric surface contribution of nitrogen as postulated by Cabrera *et al*. A bleach signal was seen in both $NTiO_2$-20 and $NTiO_2$-200 which absorbs in the visible range around 500-550nm.

A time resolved XPS study was undertaken to chart the surface concentration of nitrogen species and how they altered as a function of irradiation time. Nitrogen levels seen in XPS at ~400 eV were observed to peak in both $NTiO_2$-20 and $NTiO_2$-200 between 4-7

days of irradiation before sharply plummeting back to pre-irradiation levels. Hydroxyl surface concentrations were seen to increase and stabilise around 4/7 days concurrent with the peak and subsequent drop in concentration of nitrogen surface species. This hints that the UV induced surface migration of nitrogen may be linked to hydroxyl concentrations at the surface.

It is worth noting that in the context of the time resolved XPS study all samples exhibited a bleach signal and also are postulated to contain high levels of labile interstitial nitrogen, which subsequently surface segregate and were removed by the process of irradiation with 365 nm UVA and washing with water. Nitrogen interstitial concentration was then seen to plummet back to original surface nitrogen concentrations whilst bulk interstitial nitrogen concentrations were seen to be depleted compared to before irradiation and remain constant until the end of irradiation 28 days later. Transient absorption spectroscopy shows that the bleach signal around 500 nm was now severely diminished. This bleach signal is attributed to labile interstitial nitrogen species in the form of N-O species.[119]

Thus so far, both nitrogen doped samples were observed to exhibit similar charge carrier generation rates under UV illumination and also exhibit the segregation of interstitial nitrogen with nitrogen levels increasing proportionally with irradiation time. Finally, photo-activity measurements were taken to ascertain what effect this had upon the observed rates of photo-catalysis.

These results are similar to those reported by Cabrera *et al*.[112] Initially TiO_2, $NTiO_2$-20 and $NTiO_2$-200 exhibit roughly similar rates of photo-catalysis. However, once irradiation begins the rates of photo-catalysis for nitrogen doped samples were seen to correlate

positively with irradiation time and thus nitrogen surface concentration. Little was observed in the way of visible light photo-catalysis using stearic acid as an analysis method.

In light of further literature it is important to separate the phenomenon of enhanced UV photo-activity and the presence of visible light photo-activity.

Ultraviolet activity in nitrogen doped samples was seen to increase with irradiation time which coincided with an increasing amount of surface interstitial sites observed in XPS compared to pristine TiO_2. Given that there is no difference in charge carrier generation rates and recombination kinetics pre-irradiation it is therefore postulated that surface interstitial sites are contributing stoichiometrically towards the reduction of the resazurin dye resulting in an increase in the apparent photo-catalytic rate. The exact nature of this mechanism is unknown. One possible mechanism involves the reaction of superoxide, itself a product of reaction between elemental atmospheric oxygen and a surface electron (Ti^{3+}), and nitric oxide (NO^-), which can be found in the form of interstitial nitrogen co-ordinated to an oxygen site, to form surface bound intermediates such as peroxynitrite/peroxynitrous acid (ONOO-/ONOOH). These could contribute electrons to the resazurin dye before degrading into NO_2 species and surface Hydroxyl species as a possible mechanism.[122,123,207,208] Both NO_2, NO_3 and OH species were observed in XPS in this study and by Cabrera *et al.* Hydroxyl concentration at the surface was seen to increase and then plateau around 4-7 days onwards, adding weight to the idea that a mechanism similar to this may be responsible for the stoichiometric contribution to the observed rate of photo-catalysis. However, further work is of course required to quantitatively comment on this.

Literature reports focusing specifically on the surface of anatase and rutile single crystals demonstrate that oxygen vacancies and anionic dopants, such as nitrogen, are labile within the TiO_2 matrix and it appears that their movement is facilitated by the creation of surface and bulk differences in oxidation state. However, most studies focus on the thermal diffusion of dopants and defects between 400-1000 K, which is outside the temperature range of the phenomena discussed.[209–212]

This work indicates that, even at room temperature, the process of simply irradiating the surface is enough to create oxidation differences large enough between the surface and bulk to facilitate the movement of labile dopants and defects between these two areas. This explains how interstitial nitrogen concentrations at the surface are observed to increase proportionally with irradiation time. They are then used in stoichiometric surface reactions, and then removed in the form of NO_2 and NO_3 species in the process of washing. Under constant UV irradiation the oxidation difference between the surface and bulk is maintained, ensuring the diffusion of nitrogen interstitials to the surface. Once all labile nitrogen interstitials are consumed the surface nitrogen concentration is seen to mirror that of the surface before irradiation began. This observation corroborates previous theoretical calculations, which show that it is thermodynamically favourable for interstitial nitrogen to diffuse away from the bulk to the surface.[198]

Regarding the lack of observed visible light photo-activity, the test employed by the majority of studies involves the reduction of a dye in solution,[113,116,213] hence they are not dependent upon the creation of hydroxyl radicals. As stearic acid destruction does require hydroxyl radical formation it could be that the energy required to create a hydroxyl radical is too high for visible irradiation in the nitrogen doped TiO_2 system. This

may explain why this study and that of Cabrera *et al* do not observe any visible light induced photo-catalysis.[112] Another explanation proposed by Zhang *et al* demonstrates that the process of visible light photo-catalysis is found to be a product of both oxygen vacancies and nitrogen doping.[214] Nitrogen levels are seen to be around those found within the literature but studies to probe whether sufficient oxygen vacancies are present within the sample are required to determine this.

This study highlights the importance of long term testing in the field of photo-catalysis. If a material is to be considered fit for use in an environmental application it must be tested on appropriate time scales. That room temperature UV irradiation is sufficient to facilitate the loss of interstitial nitrogen dopants also raises question about doped TiO_2s in general and whether they will exhibit the desired photo-catalytic rates, observed in the laboratory over longer time periods.

5.5 Conclusions

Nitrogen doped TiO_2 has been grown for the first time by AACVD using a one pot solution. The films exhibited differing levels of nitrogen doping. They were characterised by XRD, XPS, SEM, UV-Visible transmission spectroscopy and their photo-activity in the UV and visible range charted using a resazurin based dye and steric acid respectively. Transient absorption spectroscopy (TAS) was utilised for charting the lifetime and recombination kinetics of all samples. The nitrogen doped samples exhibit similar photo-activities to pristine TiO_2 before irradiation but the observed rate of photo-catalysis in nitrogen doped samples increased after irradiation for seven days. This is attributed to the irradiation induced surface migration of nitrogen interstitial states (N^o) which stoichiometrically add to the baseline photo-catalytic rate of TiO_2 resulting in an

observed increase in the overall photo-catalytic rate. Transient absorption spectroscopy confirms that the charge carrier generation and lifetime remains unchanged as a result from nitrogen doping backing up this hypothesis. Whilst focusing primarily on nitrogen doped TiO_2 this study has important implications for the pursuit of future photo-catalysts for use in long term applications. Many doped materials may exhibit similar properties on the timescales investigated and may suffer loss of activity as a result of irradiation induced surface diffusion and subsequent loss. Testing on this timescale has yet to be realised in the photo-catalysis community and must play an important role in further studies for the evaluation of whether a material, which may exhibit high initial rates of photo-catalysis, will exhibit that rate on longer timescales given UV irradiation is sufficient, in this instance, to cause the surface segregation and loss of nitrogen dopants in TiO_2.

6 Chapter VI: Incorporation of High Photo-catalytic Activity and Low Resistivity in N/Nb Co-doped TiO_2 Thin Films by Combinatorial AACVD.

6.1 Introduction

Given the success of the previous chapter in elucidating previously unknown facets of nitrogen doped TiO_2, experiments were conceived to explore more complex systems such as N/ Nb co-doped TiO_2. As discussed previously titanium dioxide, particularly once doped, is a material of interest in many technological fields such as solar photovoltaics,[215] photo-catalysis[47] and transparent conducting oxides (TCOs)[216] because of its low cost, low toxicity and well defined physical properties.[217] In an effort to combine two or more functional properties, such as photo-catalytic activity and high conductivity, the use of co-dopants has featured heavily in the literature. [218–221] The dopants usually involve an anionic and cationic dopant. One particular set of dopants that has attracted recent interest is N/ Nb doped TiO_2. The singularly doped materials are well characterised within the literature and this body of work. As discussed in Chapter V, nitrogen doped TiO_2 exhibits a shift in the observed bandgap towards the visible region of the electromagnetic spectrum. It also reports an enhancement in UV induced photo-catalysis which is shown to have a stoichiometric surface reaction component. Niobium doped TiO_2 is of interest principally because of its ability to populate the Fermi level of TiO_2 closer to the conduction band so that Nb doped TiO_2 exhibits conductivities orders of magnitude higher than undoped TiO_2.[127,130,222–225] Co-doping of this nature has been explored in powder form before but not in thin film form, which convey many advantages in terms of analysis.[20,21] With this in mind niobium and

nitrogen co-doped thin films have been synthesised by combinatorial aerosol assisted chemical vapour deposition (cAACVD) for the first time.[107,139] Given that nitrogen is shown to contribute little in enhancing TiO_2's functional properties, the relationship of niobium to changes in functional properties across the combinatorial film is of particular interest.

6.2 Experimental

6.2.1 Thin film Preparation using AACVD

Nitrogen (99.99%) (BOC) was used as supplied. Depositions were obtained on SiO_2 coated float-glass. Prior to use the glass substrates were cleaned using water, isopropanol and acetone and dried in air. Glass substrates of ca. 90 mm x 45 mm x 4 mm were used. The precursors; titanium (IV) isopropoxide (99%), niobium (IV) ethoxide (99%) and n-butylamine (99%) were obtained from Sigma-Aldrich Chemical Co. and used as supplied. Aerosols were generated in ethanol (99%) and toluene (98%) and carried into the reactor in a stream of nitrogen gas through a brass baffle to obtain a laminar flow. A graphite block, containing a Whatmann cartridge heater, was used to heat the glass substrate. The temperature of the substrate was monitored using a Pt–Rh thermocouple. Depositions were carried out by heating the horizontal bed reactor to the required temperature of 450^{o}C before diverting the nitrogen line through the aerosol and hence to the reactor. At the end of the deposition, under the nitrogen flow, the glass substrate was left to cool to room temperature with the graphite block before it was removed. To synthesise the combinatorial Nb/ N co-doped TiO_2 film titanium (IV) isopropoxide (0.5 g) and n-butylamine (3.6 ml) was dissolved in ethanol (20 ml) and added to a flask. In a separate flask was added titanium (IV) isopropoxide (0.5 g) and

niobium (IV) ethoxide (20%) dissolved in toluene (20 ml) and the separate flasks connected to a split nitrogen line with the aerosol feed leading from the individual flasks to a specially constructed baffle ensuring mixing of the individual precursor streams happened in the reactor under nitrogen flow. AACVD was carried out at 500 ^{o}C until both aerosol solutions were exhausted; effort was made to match the intensity of the aerosol so that this happened at roughly the same time.

6.2.2 Sample Characterisation

X-ray diffraction (XRD) was carried out using a Lynx-Eye Bruker X-ray diffractometer with a mono-chromated Cu Kα (1.5406 Å) source. X-ray photoelectron spectroscopy (XPS) was carried out using a Thermo Scientific K-Alpha instrument with monochromatic Al-Kα source to identify the oxidation state and chemical constituents. High resolution scans were done for the Ti (3d), Nb (3d), N (1s), O (1s) and C (1s) at a pass energy of 40 eV. The peaks were modelled using Casa XPS software with binding energies adjusted to adventitious carbon (284.5 eV). SEM images were taken on a JEOL JSM-6301F Field Emission instrument with acceleration voltage of 5 kV. Images were captured using SEMAfore software. Samples were cut into coupons representing the locations on the grid and coated with a fine layer of gold to avoid charging. The optical transmission was measured over 350–1500 nm range using a Lamda 950 UV/Vis spectrometer.

6.2.3 Functional Property Testing

Photo-catalytic activity was assessed using an established method based on a resazurin 'intelligent ink' first developed by Mills *et al.*[168] Photo induced wettability was tested by placing the samples under a UVC lamp for 2 hours then measuring the water contact angle by placing a 5 µL droplet onto the surface of the films. The film was then irradiated

overnight for 16 hours and water contact angles were re-measured. Water droplet contact angles were measured using a First Ten angstroms 1000 device with a side mounted rapid fire camera after casting a 5 µL droplet from a fixed height onto the surface. To assess the photo-catalytic activity of the film at sites marked at specific grid positions the whole sample was first washed with water, rinsed with isopropanol and irradiated for 30 minutes to clean and activate the sample. A resazurin based ink was then evenly applied using a spray gun and the photo-induced degradation of the resazurin ink monitored by canning whole images of the film and calculating the photo activity by measuring the change in the red component of the pixels of the scanned images at specific grid positions. Formal quantum efficiency and the formal quantum yield was then calculated. Formal quantum efficiency was calculated by dividing the rate of dye molecules destroyed per s per cm^2 by the photon flux (4.53×10^{14} photons per cm^2 per s). The formal quantum yield (FQY) was calculated by dividing the rate of dye molecules destroyed per s per cm^2 by the number of photons absorbed by the films. The photon flux and photon absorption for each film was determined using a UVX digital radiometer with a detector for 365 nm radiation attached.

6.3 Results

The combinatorial film was generated, using AACVD at a deposition temperature of 500 ^oC, by creating two separate N or Nb doped TiO_2 precursor solutions for the formation of nitrogen and niobium doped TiO_2 respectively. This ensured the combinatorial nature of the film. Both precursor solutions were aerosolised and fed into the deposition chamber under inert gas flow separately, utilizing a custom baffle that ensured the precursor streams mixed only when inside the reactor. Once the deposition was

completed the combinatorial film generated was over laid with a grid so that individual areas of the film could be selected and analysed. In this way data on how crystal structure, elemental composition and functional properties change as a result of relative concentrations of dopants were collected. The resulting film with overlaid grid can be seen in Figure 6.1. The graduation from yellow to aquamarine to blue to purple can be seen across the width of the film, confirming on a qualitative level that the concentration of dopants changes across its width.

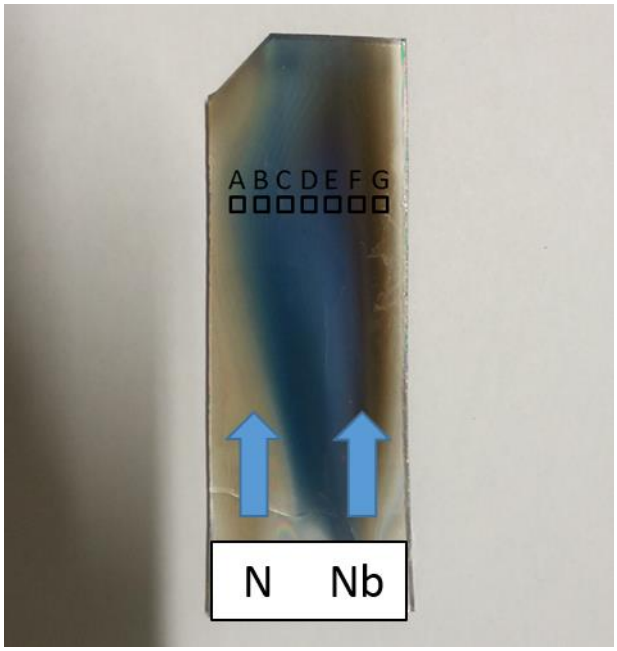

Figure 6.1: The combinatorial film. The left hand side is nitrogen dominant and the right hand side niobium dominant. A grid is overlaid to standardise analysis areas and create samples. The graduating nature of the film is evident with a transition from yellow to blue through to purple and eventually brown is clearly visible.

6.3.1 Characterisation

The combinatorial film was analysed by X-ray diffraction (XRD), X-ray photoelectron spectroscopy (XPS), scanning electron microscopy (SEM) and transmission UV/Visible spectroscopy. This allowed changes in crystallinity, elemental composition, morphology and band gaps to be charted relative to each other.

6.3.1.1 X-ray Diffraction (XRD)

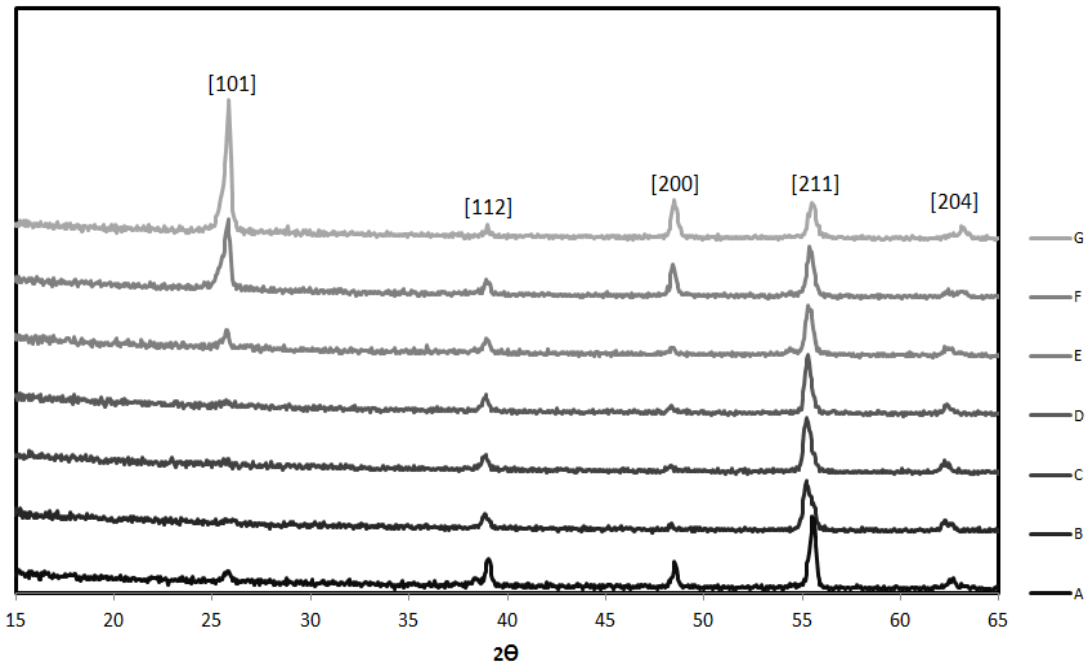

Figure 6.2: A graph comparing the XRD patterns from all samples A – G grown at 500 °C by combinatorial AACVD. All samples are seen to exhibit crystal structure concordant with anatase TiO_2. A change in the prevalence of peaks and shifting is evident across the samples. A change in intensity is particularly acute in the [101] and [200] planes. The [112] and [211] planes exhibit little change in intensity, however the [211] exhibits a shift in its 2θ value as focus moves from left to right across the width of the film.

X-ray diffraction was undertaken for all samples A- G (Figure 6.2). All samples exhibit TiO_2 XRD reflections consistent with anatase TiO_2. No reflections are attributed to Nb_2O_5 or TiN. The prevalence of certain crystal planes is seen to fluctuate across all grid positions. All grid positions therefore display some form of preferred orientation. The [101] plane was observed to disappear from samples A – D and then reappear with heightened prevalence from samples E – G with the [200] plane changing in a similar way. The [112] plane was observed to remain constant throughout all samples as was the [211]. In the context of N and Nb doping, it is expected that Nb doped samples will exhibit a shift to lower 2θ values as seen in the [212] peak.[227] Nitrogen doping on its own

does not historically produce a lattice expansion within the TiO_2 matrix as its ionic radii is not big enough to cause this, acting either as a substitutional or interstitial dopant. Therefore any shift seen is most likely due to the uptake of Nb into substitutional position replacing Ti^{4+} with Nb^{5+}. However given the ionic radius of Nb^{5+} (0.64 Å) and its similar size to Ti^{4+} (0.61 Å) the lack of shift in any other peak is unsurprising.

6.3.1.2 X-ray Photoelectron Spectroscopy (XPS)

X-ray photoelectron spectroscopy (XPS) was undertaken for all samples to identify the relative concentration of elements so as to quantify the variances in co-doping of nitrogen and niobium that occurs across the film between positions A - G. XPS was also used to identify the oxidation state and environment of the nitrogen and niobium dopants within the TiO_2 matrix. Depth profiling was also undertaken to compare the identity and ratios of elements on the surface compared to within the bulk. No niobium was identified at the surface but nitrogen in the form of NH_x, N_2 and NO_x was observed at all positions. After 900s of sputtering to sample the bulk niobium was found to reside at positions C-G. All positions A - G exhibited peaks characteristic of Ti^{4+} at ~464.5 eV and ~458 eV for the Ti^{4+} 2p 1/2 and 3/2 peaks respectively, which is indicative of TiO_2. This was corroborated further by the identification of oxygen peaks at ~530 eV for the oxygen 1s peak which is characteristic of oxygen in TiO_2. At positions D and E there is also evidence of Ti^{3+} at the surface with a peak with a binding energy of ~457 eV. It is however in the minority with Ti^{4+} being the dominant oxidation state for titanium. Nitrogen and niobium levels varied across the width of the film with nitrogen levels remaining constant across the film within the bulk whilst niobium levels were found to be highest at the side where the niobium precursor entered the reactor and proceeded

to drop off as focus moves from position G left to position A with no niobium found at position A. The variances in nitrogen and niobium doping were quantified and compared (Figure 6.3).

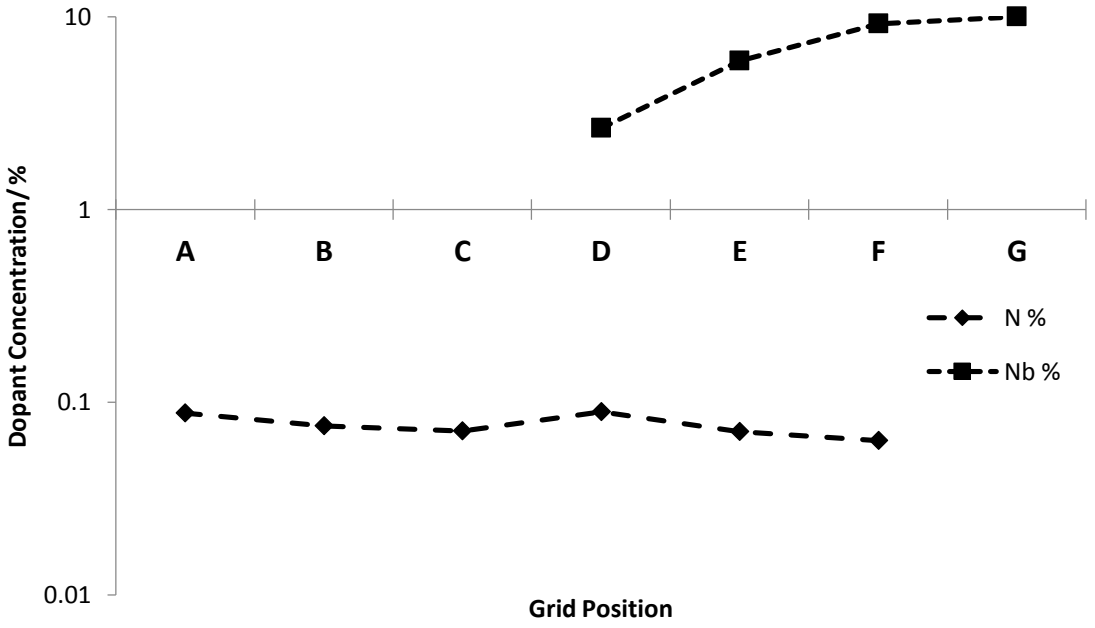

Figure 6.3: A graph comparing how the nitrogen and niobium concentration changes from positions A – G of the combinatorial film. Nitrogen is seen to remain constant around 0.08 (atom) % across all positions. Niobium concentration is seen to increase from around 2.6% at position C in a proportional manner to about 8% at position G. The method of combinatorial deposition to create many samples which exhibit different levels of co-doping is thus proved. All percentages calculated from XPS.

Nitrogen was found to reside as both an interstitial (~396 eV) and substitutional (~399 eV) dopant from the surface all the way through to the bulk (Figure 6.4 A). Given the in-depth discussion of nitrogen doped TiO_2 in the previous chapter it is important to note that the presence of surface nitrogen species can affect the perceived rate of photo-catalysis and this will be discussed in light of photo-activity data later. Niobium was found not to reside at the surface and only existed as a substitutional dopant deep within the bulk. Peaks at ~203 eV were found to be congruent with Nb bonded to O

indicating that niobium is directly bonded to oxygen in place of titanium within the bulk. Peaks at ~208 eV and ~206 eV are attributed to niobium oxy-nitride (Figure 6.4 B). XPS therefore proves that creating samples that vary in the level of nitrogen and niobium co-doping in a single deposition utilising a high throughput method, in this case combinatorial AACVD, has been achieved.

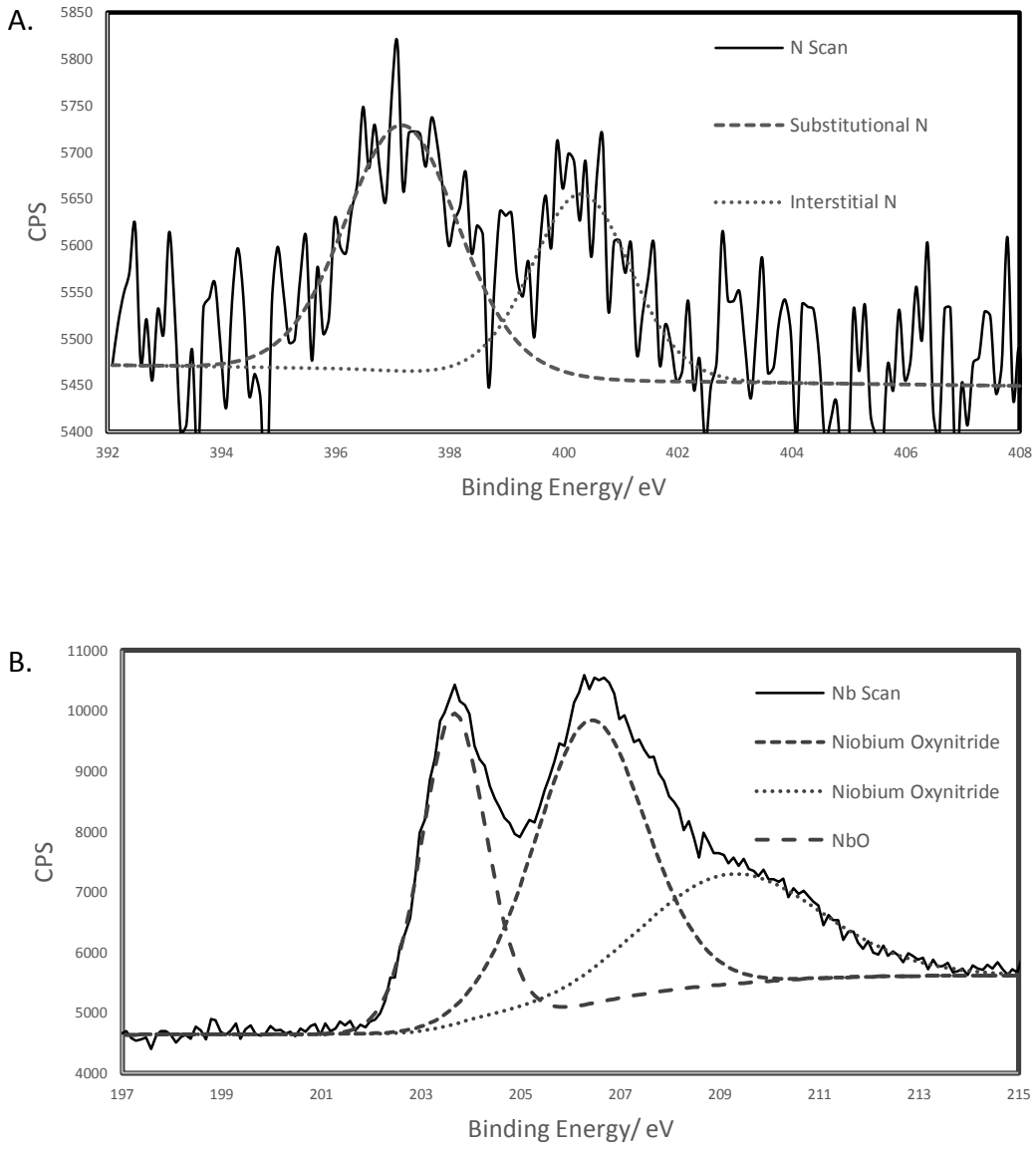

Figure 6.4: A. Sample Niobium 3d XPS spectrum showing the peaks responsible for niobium oxynitride and niobium oxide. B. Sample nitrogen 1s XPS spectrum showing the peaks responsible for interstitial and substitutional nitrogen.

6.3.1.3 Scanning Electron Microscopy (SEM)

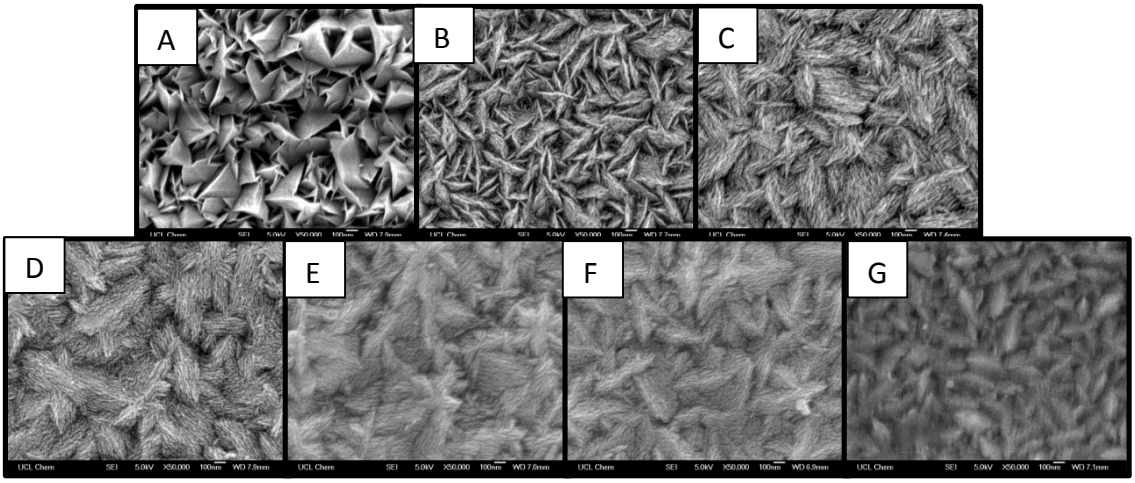

Figure 6.5: SEMs for positions A – G. Position A exhibits a highly porous and well defined 'shark tooth' morphology. From positions B- G there are two marked changes, overall the highly structured morphology seen in A is observed to degrade incrementally from B through to G. Also the structure appears to break down into small strands or fibres as from position A- G.

SEM was taken of all samples (Figure 6.5). Surface morphology is an important consideration when discussing photo-catalytic rates as surface area can change as a result of changes in morphology. Changes in morphology are also responsible for changes in water contact angles and other properties. The morphology seen at position A exhibits thin 'shark tooth' like growths observed in the Chapter V for nitrogen doped TiO_2. The film was observed to be highly porous with a high surface area. Position B exhibited very similar morphologies but the porosity was seen to decrease with the grains sitting closer to each other. The grains also exhibited secondary structure that manifested itself as veins or threads along its length. Position C exhibited a transition in morphology, with the primary 'sharktooth' structure starting to break down and the secondary thread structure starting to take over with more and more threads becoming evident. This trend continues through positions D – G until in F and G there is little left of the 'sharktooth' morphology and the threads that grew from them become the

dominant morphology. Thus overall the quality of morphology was observed to decrease from left to right across the width of the film.

6.3.1.4 UV/Vis Transmission Spectroscopy

Ultraviolet- visible transmission spectroscopy was undertaken to calculate how the bandgap changes between samples A-G (Figure 6.6). As sample A should exhibit the highest levels of nitrogen dopant and the lowest levels of niobium doping it can be, relative to the rest of the samples, be considered the most similar to purely nitrogen doped TiO_2. This was reflected in the calculated bandgap at position A, which was 2.44 eV. This is concordant with much of the literature regarding nitrogen doped TiO_2. From position A through to position G the bandgap was seen to increase to and beyond the literature bandgap value for non-doped anatase TiO_2 (3.2 eV). The bandgap was seen to plateau around 3.5 eV between positions D-G. This increase of bandgap values was indicative of Nb doped TiO_2.[228,229]

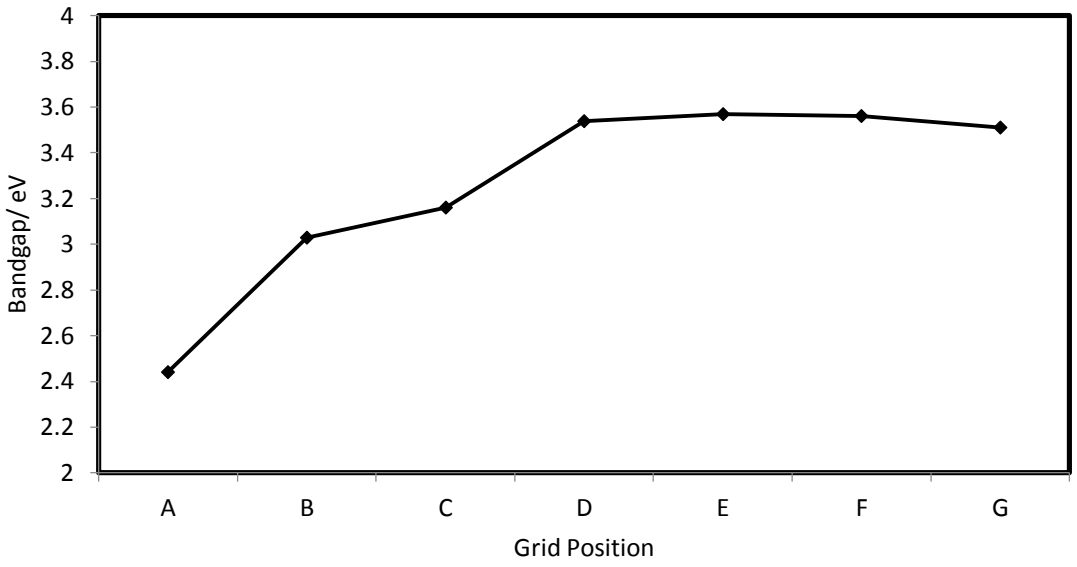

Figure 6.6: A graph of bandgap values for all positions A-G. At position A, which should exhibit bandgap values similar to nitrogen doped TiO_2 and a value of 2.44 eV is seen which agrees with literature published on N doped TiO_2. The bandgap is then seen to increase to 3.03 and 3.16 for position B and C respectively. This is close to the reported value of 3.2 eV for non-doped anatase TiO_2. The band gap then increases past this point at position D to 3.51 eV and plateaus around 3.55 eV for positions E-G.

6.3.2 Functional Properties

Functional property testing was undertaken so that changes in photo-catalysis, water contact angle and resistivity that occur across the width of the combinatorial film can be correlated with changes in elemental composition, crystal structure and morphology as seen in previous combinatorial studies.[146]

6.3.2.1 Hall Effect Measurements

Hall Effect measurements were carried out for all positions. Grid position C-F provided meaningful data whilst positions A-B and G exhibited resistivity values too high to obtain data. Thin film thickness was first calculated utilising the Swanepoel method.[158] This was then used to allow the calculation of bulk carrier concentration, carrier mobility and resistivity (Table 6.1). It was observed that the sign of the bulk carrier concentration

switched from positive to negative from position C to position D-F. This signals a change from a p-type to n-type semiconductor and is congruent with previous literature reports. The switch also coincides with the appearance of Nb doping in position D to G onwards. No Nb was found at position C and as such it is only nitrogen doped explaining the p-type behaviour. Resistivity values from C-F were seen to decrease by an order of magnitude as niobium content, as seen by XPS, increases. Thus it is evident that niobium is contributing electrons to the Fermi level and populating the conduction band with a higher proportion of mobile electrons congruent with literature reports. Whilst bulk carrier concentrations and carrier mobility were seen to vary in magnitude it is difficult to relate this to dopant effects as film thickness was seen to decrease from positions C-F, which is an artefact of the combinatorial deposition process. Given that resistivity decreased in line with a decrease in thin film thickness, it can be assumed that dopant effects are responsible for this change in resistivity across positions C-F.

Table 6.1: Hall Effect data for positions C-F. Thin Film Thickness is seen to vary across the width of the film which is expected as an artefact of the combinatorial deposition regime. Bulk carrier concentration is seen to switch from C to D-F from p-type (N: TiO_2) to n-type (Nb: N: TiO_2). Resistivity is also seen to decrease from C through to F which correlates with increasing niobium content seen in XPS.

Samples	Film Thickness/ nm	Bulk Carrrier Concentration/ cm^3	Carrier Mobility / $cm^2 Vs^{-1}$	Resitivity / Ω cm
A	-	-	-	-
B	-	-	-	-
C	1500	1.19E+20	6.49E+00	8.06E-03
D	1379	-4.52E+19	1.85E+01	7.47E-03
E	494	-2.89E+20	6.98E+00	3.10E-03
F	572	-1.01E+19	2.95E+01	2.10E-02
G	-	-	-	-

6.3.2.2 Photo-catalysis

The photo-activity of all positions was measured by charting the reduction of a resazurin based ink to resorufin, first utilised by Mills *et al* (Figure 6.7).[168] It was found that positions A and B exhibit the highest rate of photo-activity. From this point it was observed that photo-activity for other positions decreases incrementally from points B-G by roughly an order of magnitude. In comparison with SEM, it is interesting that the morphology observed in A and B was seen to degrade and change from point C-G. Thus morphology can be said to play a vital part in the observed rate of photo-catalysis. As the morphology seen from C-F in SEM does not change between these points, yet photo-activity was seen to continue to decrease in an incremental and proportional manner, it can be deduced that whilst morphology plays an important role in the observed rate of photo-catalysis, the role of co-dopant concentration is hinted at by the disparity between the declining photo-catalytic rate observed from B-G and the change in morphology that occurs between B-C. Formal Quantum Yield (no. of molecules destroyed per incident photon) and Formal Quantum Efficiency (no. of molecules destroyed per absorbed photon) values are seen to mirror the photo-catalytic rate at each position (Figure 6.8). Position G is a more efficient photo-catalyst compared to position A as its FQY and FQE are relatively similar, whereas there is a larger disparity between the FQE and FQY at position A. This however does not take in consideration changes in surface morphology which are seen to occur from positions A to G.

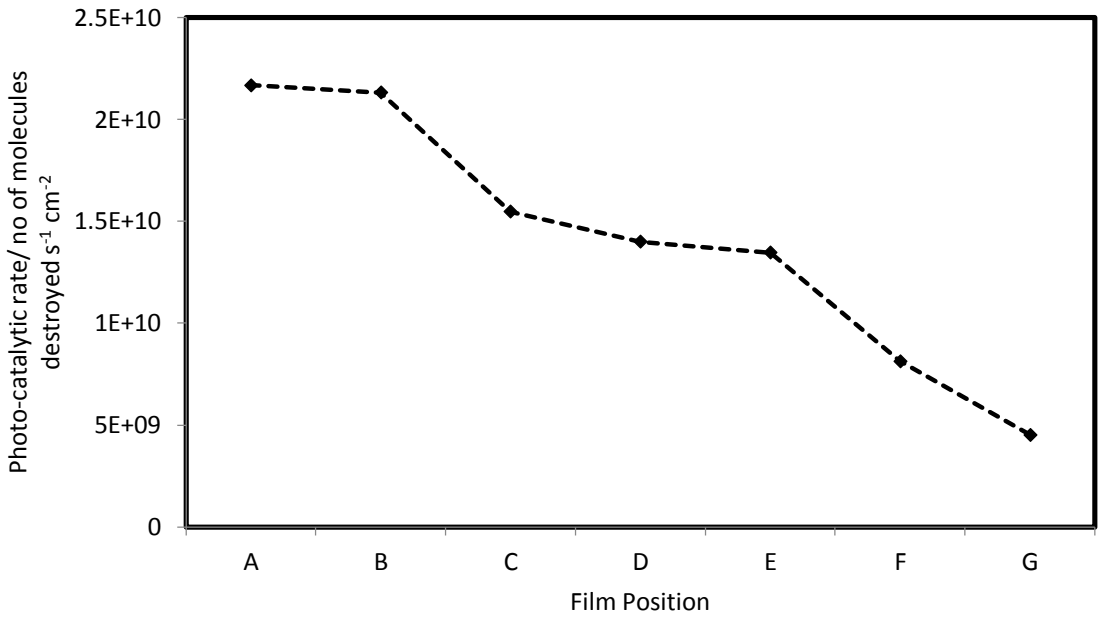

Figure 6.7: A graph comparing the photo-catalytic activity of all positions A – G. It is observed that UV photo-activity is highest at position A, where the level of nitrogen doping is highest and the level of niobium doping is lowest. Photo-activity proceeds to then decrease incrementally from position B – G by roughly an order of magnitude.

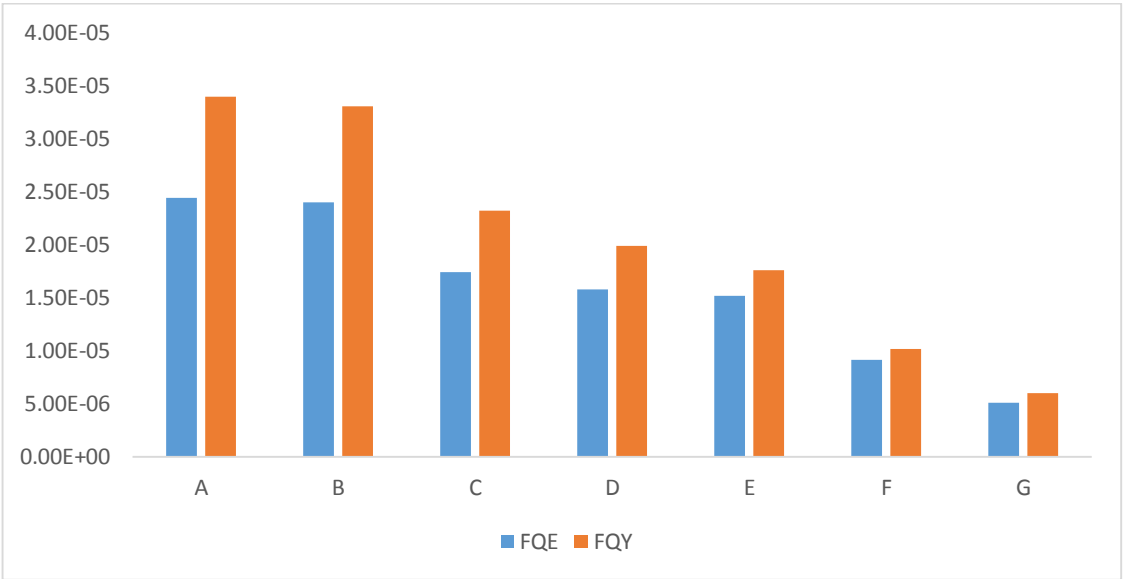

Figure 6.8: Formal Quantum Yields and Formal Quantum Efficiencies for all positions. A decrease in both FQY and FQE is seen as focus moves from position A to G. This mirrors the photo-catalytic rates in charting a decrease from nitrogen doping to niobium doping, which is expected. The sample at position G is a more efficient photo-catalyst compared to position A but exhibits an overall lower rate of charge carrier generation. This does not take into account the effects that surface morphology can have, as surface morphology is seen to change across the film from positions A to G.

6.3.2.3 Water Contact Angles

Water contact angles are found to be hydrophilic at point A and then increase as focus transitions to point B. The rest of the film exhibits little change in pre-irradiation water contact angles from this point onwards with points C – G exhibiting fairly similar contact angles. After irradiation all samples are seen to exhibit photo-induced wettability, indicating that all samples are photoactive with point B exhibiting the biggest change in contact angle (Figure 6.9 and Table 6.2).

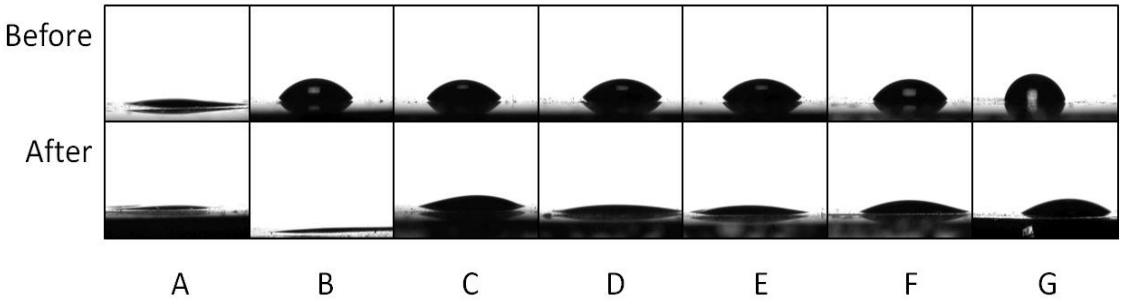

Figure 6.9: Water contact angles before and after 24 hours of irradiation with a 365nm UV light source. Point A is seen to display hydrophilic behaviour both before and after irradiation. All other samples exhibit higher water contact angles, with roughly similar angles from point B – G. After irradiation all samples are seen to exhibit photo-induced wettability, with point B exhibiting the biggest change in water contact angle.

Table 6.2: A table of water contact data for the combinatorial film for all points A- G

Sample	Water Contact Angle/ ^{o}	
	Before	After
A	19.1	7.3
B	58.3	6.4
C	53.1	23.8
D	49.6	9.2
E	51.8	11.5
F	62.7	17.3
G	82.4	36.2

6.4 Discussion

XRD shows that crystalline samples of anatase TiO_2 are present across the entire width of the combinatorial film. The change in intensity of peaks, and therefore preferential orientation, in the diffraction patterns between samples demonstrates that the formation of these materials is subject to different conditions which can be attributed to the incorporation of dopants within the TiO_2 matrix. Coupled with SEM this corroborates the idea of changing preferential orientation as microstructure was seen to change in a linear fashion from one morphology to another as the concentration of niobium changes relative to nitrogen.

XPS confirms on a quantitative level that nitrogen and niobium co-doped TiO_2 thin films have been achieved. Interestingly nitrogen levels were seen to remain relatively constant across the entire width of the film while niobium exhibits the expected tail off as focus moves from the right, where the niobium dopant stream enters the reactor, to the left. This is novel as the experimental setup should ensure that nitrogen starts high

in concentration on the left hand side, where its precursor stream enters the reactor, and drops off in concentration to the right. That this is not observed leaves two possibilities. Either the nitrogen is diffusing and equalising throughout the whole film once it is incorporated due to thermal diffusion or the n-butylamine has a longer residence time within the reactor and is diffusing far to the right and into the niobium stream before degrading and becoming incorporated. Given discussion in the previous chapter regarding the lability of interstitial nitrogen via UV induced surface segregation and literature reports of thermal diffusion at 400 K and above it is entirely possible that nitrogen is found throughout the entire material as a result of thermal induced diffusion that occurs as an artefact of the deposition process (>700 K). However further experimentation is therefore required to elucidate the true mechanism behind this.

Bandgap values expected for nitrogen doped TiO_2 and niobium doped TiO_2 are observed in the expected positions (A for N-TiO_2 and G for Nb-TiO_2) with a transition in between. There is no apparent lowering of the bandgap seen in literature reports for other N/Nb co-doped TiO_2s and this is attributed to low concentrations of nitrogen and relative inhomogeneity of the films. [124,125,226]

Regarding functional properties photo-catalysis exhibits the expected change in photo-catalysis shown in the literature with a decrease in ultraviolet photo-catalytic rate seen from nitrogen doped TiO_2 to niobium doped TiO_2. Formal quantum efficiency and yield (FQE and FQY) values are seen to mirror changes in photo-catalytic rate. That a change in morphology is concurrently seen with this transition highlights the importance of microstructure and its ability to produce an enhanced observable rate of photo-catalysis whilst the material inherently produces the same amount of charge carriers regardless

of doping. The role of nitrogen surface species must be considered too. That nitrogen surface species are found at all positions suggests that they may add to the perceived rate of photo-catalysis in a stoichiometric fashion. However, as noted in the previous chapter, pre irradiation, the nitrogen doped samples exhibit similar rates to non-doped TiO_2. Thus it can be reasoned that without the input of sustained periods of UV irradiation over several days, the stoichiometric role of nitrogen surface species can be considered minimal. As nitrogen levels are roughly constant throughout the material both at the surface and bulk across all positions differences in the photo-catalytic rate can be discussed without needing to invoke stoichiometric surface reactions between the resazurin dye and N surface species. When considering the contribution that dopants make to the photo-catalytic rate, it must be remembered that niobium states seen from position D-G lie deep within the bulk and hence contribute very little to changes in charge carrier generation or recombination for photo-catalysis as the underlying recombination rate of TiO_2 ensures that only charge carriers generated at or near the surface undergo surface redox reactions. The previous chapter demonstrates that nitrogen as a dopant promotes the lifetime of charge carriers by acting as a trap state, and as the concentration of nitrogen is found to be roughly equal at all positions the decrease in photo-catalytic rate seen from positions A - G can be considered to simply arise from the transition in microstructure seen from positions. Photo induced wettability studies highlight that whilst all samples differ in photo-catalytic rate, they all exhibit some form of photo-activity, as all samples start hydrophilic and upon UV irradiation at 365nm for 24 hours they exhibit a further decrease in the water contact angle. Positions A and B unsurprisingly give the largest change in water contact angles.

Hall Effect measurements demonstrate that the left hand side of the film, which is nitrogen doped, exhibits p-type behaviour and that once niobium is found in the bulk this switches to n-type behaviour in good agreement with the literature.[127,230] Thus despite niobium lying deep within the bulk it is prominent enough to define the nature of charge carrier in positions D-F. The values reported in this work compare favourably with literature reports for doped ZnO with charge carrier concentrations on the order of ~10^{20} cm^{-3} and resistivity values on the order of 10^{-3} but cannot compete with industry standards such as ITO which exhibit charge carrier concentrations and resistivity values an order of magnitude better.[231] This can be attributed to the inhomogeneity of the films at positions C-F, as shown in XPS, where TCO behaviour is observed.

Because the photo-activity, which is relatively surface sensitive, appears decoupled from the resistivity of the bulk at specific positions, this means that a midway point can be achieved where low concentrations of niobium are sufficient to decrease resistivity and change the nature of charge carriers whilst retaining a competitive rate of photo-catalysis imbued by nitrogen doping at positions C-D. This is because the films are relatively inhomogeneous. Thus the surface and sub-surface bulk, which exhibit little niobium but are nitrogen doped, retain a high rate of photo-catalysis whilst the bulk, which is doped with niobium, displays low resistivity values and imbues the whole material with good TCO properties. Thus the incorporation of a high rate of photo-catalysis and good TCO properties in TiO_2 has been achieved using the combinatorial deposition regime in AACVD.

6.5 Conclusion

In conclusion, N/ Nb co-doped thin films with varying dopant concentrations have been synthesised by AACVD as a result of a combinatorial deposition regime. This allows for the rapid creation of many different samples in a single deposition. Samples were found, given previous work in Chapter V, to exhibit changes in functional properties that correlate strongly with changes in microstructure. Dopants such as nitrogen and niobium are observed to affect the physical properties of the material, creating variances in crystal structure, band gap and elemental composition. A good photo-catalytic rate, due to nitrogen doping, is observed from positions A-D whilst niobium, which is found from positions C-G deep within the bulk imbues competitive resistivity values upon the materials at these positions. Thus the crossover positions C and D therefore represent a half-way house where both photo-activity and resistivity values suitable in commercial applications are found.

7 Chapter VII: Conclusions and Future Work

Chapter III utilised combinatorial AACVD (c-AACVD) to explore and gain insight into the growth of a TiO_2/SnO_2 composite film which has previously been published. The technique was successful in creating a film which graduated from SnO_2 to TiO_2 across its width, left to right. In doing so it was proposed that, if the TiO_2/SnO_2 composite arose purely as a result of a particular concentration of titanium relative to tin, the composite material should occur somewhere in the middle of the film where TiO_2 and SnO_2 occurs the most. In the process of characterisation it was found that XRD, XPS and SEM all corroborated each other showing that the composite material formed in the top left hand corner of the film (grid position A4). The correct morphology identified by Ponja *et al* was reproduced along with the correct elemental profile from the surface through to bulk and the presence of anatase TiO_2 and cassiterite SnO_2 confirming the correct crystal structure for the composite. Grid position A4 was found to be the only area of significant photo-catalytic activity by the resazurin test. Because the composite material was found at grid position A4 it was hypothesised that a more complex growth profile existed for the composite material and that simple elemental ratios could not account for the manifestation of the composite material.

Chapter IV drew on these discoveries to design new experiments which would provide further insight into the growth of the TiO_2/SnO_2 composite material. To truly understand what was occurring inside the AACVD reactor samples were needed that varied as a function of deposition time and not concentration, as demonstrated in combinatorial AACVD. To do this a cover slip was inserted into the reaction chamber via the exhaust, exploiting the fact that AACVD is carried out at atmospheric pressure. This enables the

production of samples which are exposed to the same precursor stream but for varying amounts of time. By retracting the cover slip a set distance every few minutes many depositions worth of experiments can be conducted in a singular deposition, saving time whilst also providing insight into the growth profile of functional materials. It was found that the TiO_2/SnO_2 composite has three distinct growth phases, first an amorphous Ti rich SnO_2 layer forms which seeds the growth of a Sn rich anatase TiO_2 layer. Tin is then observed to migrate and surface segregate until it reaches sufficient concentrations at the surface to facilitate the growth of cassiterite SnO_2 forming the heterojunction structure observed in the composite which is proposed to enhance the rate of photo-catalysis by sequestering electrons and enhancing the lifetime of holes. It was observed that an enhanced rate of photo-catalysis is observed mid deposition hinting that this method could be used to further tailor any material grown by AACVD towards a specific functional property by mapping the deposition sequence first.

Chapter V explored the deposition of nitrogen doped TiO_2 by AACVD for the first time. Previous work within the group had identified the role of stoichiometric surface species and their contribution to the 'observed' rate of photo-catalysis. Thus a timed irradiation study over the course of 28 days was conducted to observe how; nitrogen concentrations in the bulk and at the surface, UV photo-activity and charge carrier lifetime and generation rates varied during this time. These were measured by XPS, the resazurin test and transient absorption spectroscopy respectively. It was observed in XPS that interstitial nitrogen levels both at the surface and within the bulk, were found to increase until 7 days when levels were found to drop drastically back down to pre irradiation levels. Photo-activity measurements found that UV photo-catalytic activity was found to positively correlate with surface nitrogen concentrations. Transient

absorption spectroscopy found that nitrogen doping conferred little in the way of enhanced charge carrier generation rates and that a trap state which caused bleaching of the probe signal was present. After 28 days of irradiation this bleach state is observed to have been removed. This is attributed to the UV irradiation induced surface migration and segregation of interstitial nitrogen which is then removed from the surface via stoichiometric surface reactions.

Chapter VI explores the creation of nitrogen and niobium co-doped TiO_2 using combinatorial AACVD. This was achieved by creating two precursor streams for the synthesis of nitrogen and niobium doped TiO_2 respectively. By using the combinatorial AACVD regime the precursor streams mixed once inside the reactor, thus creating a film which created a film which graduated from nitrogen doped TiO_2 to niobium doped TiO_2 with co-doped states in between. Thus changes in relative concentrations of nitrogen and niobium can be linked to changes in functional properties such as resistivity and photo-catalysis. The incorporation of TCO and photo-catalytic properties has been successfully achieved using combinatorial AACVD.

Regarding further work three distinct themes standout. Firstly the creation of composite films similar in nature to the TiO_2/ SnO_2 composite film explored in this body of work utilising the growth processes explored by time resolved AACVD. This could be achieved by creating a highly doped metal oxide which upon prolonged periods of heating, which induces surface segregation, to create a surface layer of metal oxide from the dopant.

Secondly the use of time resolved and combinatorial AACVD for the investigation of advanced functional material, such as the ones explored in this thesis should continue to be used. They provide unique insight into the growth of many materials.

Thirdly the process of irradiation has been demonstrated to cause the migration and surface segregation of nitrogen in N doped TiO_2. This is the most significant result found in this body of work. Many materials use interstitial dopants to confer favourable light interactions for use in a variety of fields. The applications they are often envisioned for use in involve protracted periods of environmental visible and ultraviolet light exposure higher in intensity than has been utilised in these experiments. Thus irradiation is shown to be able create differences in charge between the surface and bulk, which results in the migration of dopants, any material capable of generating electrons and holes (any suitable semiconductor) under visible or UV irradiation with eventually see migration and potential loss of interstitial dopants on time scales much shorter than its proposed operational lifetimes. Further work is therefore required to characterise this phenomenon.

Finally, this work has demonstrated that surface area and morphology play an important role, not attributed in the literature, in the process of photo-catalysis. It is telling in Chapter V that despite nitrogen doping of TiO_2 no enhancement of photo-catalytic rate is observed pre irradiation compared to pristine TiO_2. The role of surface species is poorly understood too and these two themes remain an important facet of photo-catalysis which is underexplored within the literature. Serpone *et al* proposes that for dopants to contribute to band structure in the manner proposed by the TiO_2 and photo-catalysis communities doping levels would have to be extremely high and risk changing the original character of the host material. Given low levels of doping explored within the literature, photo-catalytic effects that are attributed purely to dopant effects must be considered carefully.

8 References

1. Grätzel, M. Dye-sensitized solar cells. *J. Photochem. Photobiol. C Photochem. Rev.* **4,** 145–153 (2003).

2. Muthukumar, A. *et al.* Fluorine doped tin oxide (FTO) thin film as transparent conductive oxide (TCO) for photovoltaic applications. in *Solid State Physics: Proceedings of the 57th DAE Solid State Physics Symposium 2012* **1512,** 710–711 (AIP Publishing, 2013).

3. Fujishima, A. Electrochemical photolysis of Water at a Semiconductor Electrode. *Nature* **238,** 37–38 (1972).

4. NASA. Solar Radiation and Climate Experiment (SORCE). at <http://earthobservatory.nasa.gov/Features/SORCE/sorce_02.php>

5. Armenante, P. M. *Characterization of Industrial Wastewaters*.

6. Bryan, K. Man's great geophysical experiment can we model the consequences. *Ocean. (United States)* **29:4,**

7. Worm, B. *et al.* Impacts of biodiversity loss on ocean ecosystem services. *Science* **314,** 787–90 (2006).

8. Herrmann, J. Heterogeneous photocatalysis: fundamentals and applications to the removal of various types of aqueous pollutants. *Catal. Today* **53,** 115–129 (1999).

9. Peel, M. Hunger strikes. *BMJ* **315,** 829–30 (1997).

10. UN. Water for Life 2005 - 2015. at <http://www.un.org/waterforlifedecade/human_right_to_water.shtml>

11. WHO. Health through safe drinking water and basic sanitation. at <http://www.who.int/water_sanitation_health/mdg1/en/>

12. WHO. *Access to Drinking Water 2012 Update*. (2012).

13. Rolland, M., Le Moal, J., Wagner, V., Royère, D. & De Mouzon, J. Decline in semen concentration and morphology in a sample of 26,609 men close to general population between 1989 and 2005 in France. *Hum. Reprod.* **28,** 462–70 (2013).

14. Jobling, S., Nolan, M., Tyler, C. R., Brighty, G. & Sumpter, J. P. Widespread Sexual Disruption in Wild Fish. *Environ. Sci. Technol.* **32,** 2498–2506 (1998).

15. Santos, E. M. *et al.* Gonadal transcriptome responses and physiological consequences of exposure to oestrogen in breeding zebrafish (Danio rerio). *Aquat. Toxicol.* **83,** 134–42 (2007).

16. Kidd, K. A. *et al.* Collapse of a fish population after exposure to a synthetic estrogen. *Proc. Natl. Acad. Sci. U. S. A.* **104,** 8897–901 (2007).

17. Viglino, L., Aboulfadl, K., Prévost, M. & Sauvé, S. Analysis of natural and synthetic estrogenic endocrine disruptors in environmental waters using online preconcentration coupled with LC-APPI-MS/MS. *Talanta* **76,** 1088–96 (2008).

18. Bouman, A., Heineman, M. J. & Faas, M. M. Sex hormones and the immune response in humans. *Hum. Reprod. Update* **11,** 411–23 (2005).

19. Santhi, V. A., Sakai, N., Ahmad, E. D. & Mustafa, A. M. Occurrence of bisphenol A in surface water, drinking water and plasma from Malaysia with exposure assessment from consumption of drinking water. *Sci. Total Environ.* **427-428,** 332–8 (2012).

20. *Ullmann's Encyclopedia of Industrial Chemistry*. (Wiley-VCH Verlag GmbH & Co. KGaA, 2000).

21. Rueters. Experts demand European action on plastics chemical. (2010). at <http://www.reuters.com/article/2010/06/22/us-chemical-bpa-health-idUSTRE65L6JN20100622?loomia_ow=t0:s0:a49:g43:r3:c0.084942:b35124310:z0>

22. EPA, U. HPV Chemical Hazard Characterizations. at <http://iaspub.epa.gov/oppthpv/hpv_hc_characterization.get_report?doctype=2>

23. Shelby, M. D. NTP-CERHR monograph on the potential human reproductive and developmental effects of bisphenol A. *Ntp Cerhr Mon.* **22,** (2008).

24. Agency, U. S. E. P. & Environmental Protection Agency. Bisphenol A Action Plan. *Environ. Heal.* 1–22 (2011). at <http://en.wikipedia.org/wiki/Bisphenol_A#Environmental_risk\nhttp://www.epa.gov/oppt/existingchemicals/pubs/actionplans/bpa_action_plan.pdf>

25. Consumer Reports. Concern over Canned Foods. (2009). at <http://www.consumerreports.org/cro/magazine-archive/december-2009/food/bpa/overview/bisphenol-a-ov.htm>

26. Commissioner, O. of the. Public Health Focus - Bisphenol A (BPA): Use in Food Contact Application. at <http://www.fda.gov/NewsEvents/PublicHealthFocus/ucm064437.htm?_cldee=a2F0aHJ5bl9zdGpvaG5AYW1lcmljYW5jaGVtaXN0cnkuY29t>

27. Dianin, A. On condensation products of ketones with phenols. *J. Russ. Phys. Chem. Soc.* **23,** (1891).

28. Dodds, E. C. & Lawson, W. Synthetic Œstrogenic Agents without the Phenanthrene Nucleus. *Nature* **137,** 996–996 (1936).

29. Kwon, J. H., Katz, L. E. & Liljestrand, H. M. Modeling binding equilibrium in a competitive estrogen receptor binding assay. *Chemosphere* **69,** 1025–1031 (2007).

30. Matsushima, A. *et al.* Structural evidence for endocrine disruptor bisphenol A binding to human nuclear receptor ERR gamma. *J. Biochem.* **142,** 517–524 (2007).

31. Vogel, S. a. The politics of plastics: the making and unmaking of bisphenol a 'safety'. *Am. J. Public Health* **99 Suppl 3,** 559–566 (2009).

32. Li, D. *et al.* Occupational exposure to bisphenol-A (BPA) and the risk of Self-Reported Male Sexual Dysfunction. *Hum. Reprod.* **25,** 519–527 (2010).

33. Dolinoy, D. C., Huang, D. & Jirtle, R. L. Maternal nutrient supplementation counteracts bisphenol A-induced DNA hypomethylation in early development. *Proc. Natl. Acad. Sci. U. S. A.* **104,** 13056–61 (2007).

34. N'Tumba-Byn, T. *et al.* Differential effects of bisphenol A and diethylstilbestrol on human, rat and mouse fetal leydig cell function. *PLoS One* **7,** e51579 (2012).

35. Soto, A. M. & Sonnenschein, C. Environmental causes of cancer: endocrine disruptors as carcinogens. *Nat. Rev. Endocrinol.* **6,** 363–70 (2010).

36. Vrooman, L. A., Oatley, J. M., Griswold, J. E., Hassold, T. J. & Hunt, P. A. Estrogenic exposure alters the spermatogonial stem cells in the developing testis, permanently reducing crossover levels in the adult. *PLoS Genet.* **11,** e1004949 (2015).

37. Croen, L. A., Grether, J. K., Yoshida, C. K., Odouli, R. & Hendrick, V. Antidepressant use during pregnancy and childhood autism spectrum disorders. *Arch. Gen. Psychiatry* **68,** 1104–12 (2011).

38. Thomas, M. A. & Klaper, R. D. Psychoactive pharmaceuticals induce fish gene expression profiles associated with human idiopathic autism. *PLoS One* **7,** e32917

(2012).

39. Step Out Asia. Drink and Be Wary: Drinking Water in Southeast Asia. at <http://stepoutasia.wordpress.com/2010/10/31/drink-and-be-wary-drinking-water-in-southeast-asia/>

40. Sinha, R. P. & Häder, D.-P. UV-induced DNA damage and repair: a review. *Photochem. Photobiol. Sci.* **1,** 225–236 (2002).

41. Ashcroft,N. W., and Mermin, N. D. & Ashcroft, N. W. *Solid State Physics*. (Holt, Rineheart and Winston, 1988).

42. Einstein, A. Über die von der molekularkinetischen Theorie der Wärme geforderte Bewegung von in ruhenden Flüssigkeiten suspendierten Teilchen. *Ann. Phys.* **322,** 549–560 (1905).

43. Fermi, E. On the Quantization of the Monoatomic Ideal Gas. *Rend. Lincei* **3,** 145–149 (1926).

44. Dirac, P. A. M. On the Theory of Quantum Mechanics. *Proc. R. Soc. A Math. Phys. Eng. Sci.* **112,** 661–677 (1926).

45. Momox, E., Zakhleniuk, N. & Balkan, N. Solution of the 1D Schrödinger equation in semiconductor heterostructures using the immersed interface method. *J. Comput. Phys.* **231,** 6173–6180 (2012).

46. Schrödinger, E. An Undulatory Theory of the Mechanics of Atoms and Molecules. *Phys. Rev.* **28,** 1049–1070 (1926).

47. Fujishima, A., Rao, T. N. & Tryk, D. A. Titanium dioxide photocatalysis. *J. Photochem. Photobiol. C* **1,** 1–21 (2000).

48. Reisfeld, R. Nanosized semiconductor particles in glasses prepared by the sol–gel method: their optical properties and potential uses. *J. Alloys Compd.* **341,** 56–61 (2002).

49. Liang, W. Y. Excitons. *Phys. Educ.* **5,** 226–228 (1970).

50. Frenkel, J. On the Transformation of light into Heat in Solids. I. *Phys. Rev.* **37,** 17–44 (1931).

51. Wannier, G. The Structure of Electronic Excitation Levels in Insulating Crystals. *Phys. Rev.* **52,** 191–197 (1937).

52. Daneshvar, N., Salari, D. & Khataee, A. . Photocatalytic degradation of azo dye acid red 14 in water on ZnO as an alternative catalyst to TiO_2. *J. Photochem. Photobiol. A Chem.* **162,** 317–322 (2004).

53. Rao, P. S. & Hayon, E. Redox potentials of free radicals. IV. Superoxide and hydroperoxy radicals . O_2- and . HO_2. *J. Phys. Chem.* **79,** 397–402 (1975).

54. Mills, A. & Morris, S. Photomineralization of 4-chlorophenol sensitized by titanium dioxide: a study of the initial kinetics of carbon dioxide photogeneration. *J. Photochem. Photobiol. A Chem.* **71,** 75–83 (1993).

55. Cristina Yeber, M., Rodríguez, J., Freer, J., Durán, N. & D. Mansilla, H. Photocatalytic degradation of cellulose bleaching effluent by supported TiO_2 and ZnO. *Chemosphere* **41,** 1193–1197 (2000).

56. Dozzi, M. V. & Selli, E. Doping TiO_2 with p-block elements: Effects on photocatalytic activity. *J. Photochem. Photobiol. C Photochem. Rev.* **14,** 13–28 (2013).

57. Nuttall, L. Use of Hydrogen in Fuel Cells. *SAE Trans.* **74,** 102–& (1966).

58. DRAVNIEKS, A. Hydrogen – Air Fuel Cell with Homogeneous Oxidation Catalyst Redox Cycle. *Nature* **199,** 1182–1182 (1963).

59. Heller, A. Conversion of sunlight into electrical power and photoassisted electrolysis of water in photoelectrochemical cells. *Acc. Chem. Res.* **14,** 154–162 (1981).

60. Frank, S. N. & Bard, A. J. Heterogeneous photocatalytic oxidation of cyanide ion in aqueous solutions at titanium dioxide powder. *J. Am. Chem. Soc.* **99,** 303–304 (1977).

61. Frank, S. N. & Bard, A. J. Heterogeneous photocatalytic oxidation of cyanide and sulfite in aqueous solutions at semiconductor powders. *J. Phys. Chem.* **81,** 1484–1488 (1977).

62. Okamoto, K., Yamamoto, Y., Tanaka, H., Tanaka, M. & Itaya, A. Heterogeneous photocatalytic decomposition of phenol over TiO_2 powder. *Bull. Chem. Soc. Jpn.* **58,** 2015–2022 (1985).

63. Okamoto, K., Yamamoto, Y., Tanaka, H. & Itaya, A. Kinetics of heterogeneous photocatalytic decomposition of phenol over anatase TiO_2 powder. *Bull. Chem. Soc. Jpn.* **58,** 2023–2028 (1985).

64. Sakamaki, K., Matsunaga, S., Itoh, K., Fujishima, A. & Gohshi, Y. Imaging the phenol

molecule adsorbed on TiO_2(110) by scanning tunneling microscopy. *Surf. Sci.* **219,** L531–L536 (1989).

65. Al-Ekabi, H. & Serpone, N. Kinetics studies in heterogeneous photocatalysis. I. Photocatalytic degradation of chlorinated phenols in aerated aqueous solutions over titania supported on a glass matrix. *J. Phys. Chem.* **92,** 5726–5731 (1988).

66. Sclafani, A., Palmisano, L. & Davì, E. Photocatalytic degradaton of phenol in aqueous polycrystalline TiO_2 dispersions: the influence of Fe^{3+}, Fe^{2+} and Ag^{+} on the reaction rate. *J. Photochem. Photobiol. A Chem.* **56,** 113–123 (1991).

67. Li, X., Cubbage, J. W. & Jenks, W. S. Photocatalytic Degradation of 4-Chlorophenol. 2. The 4-Chlorocatechol Pathway. *J. Org. Chem.* **64,** 8525–8536 (1999).

68. Matthews, R. W. Photooxidation of organic impurities in water using thin films of titanium dioxide. *J. Phys. Chem.* **91,** 3328–3333 (1987).

69. Shaban, Y. a, El Sayed, M. a, El Maradny, A. a, Al Farawati, R. K. & Al Zobidi, M. I. Photocatalytic degradation of phenol in natural seawater using visible light active carbon modified (CM)-n-TiO_2 nanoparticles under UV light and natural sunlight illuminations. *Chemosphere* **91,** 307–13 (2013).

70. Al-Sayyed, G., D'Oliveira, J.-C. & Pichat, P. Semiconductor-sensitized photodegradation of 4-chlorophenol in water. *J. Photochem. Photobiol. A Chem.* **58,** 99–114 (1991).

71. Mills, A., Hill, C. & Robertson, P. K. J. Overview of the current ISO tests for photocatalytic materials. *J. Photochem. Photobiol. A Chem.* **237,** 7–23 (2012).

72. Robinson, T., McMullan, G., Marchant, R. & Nigam, P. Remediation of dyes in textile effluent: a critical review on current treatment technologies with a proposed alternative. *Bioresour. Technol.* **77,** 247–255 (2001).

73. Glaze, W. H., Kang, J.-W. & Chapin, D. H. The Chemistry of Water Treatment Processes Involving Ozone, Hydrogen Peroxide and Ultraviolet Radiation. *Ozone Sci. Eng.* **9,** 335–352 (1987).

74. Spadaro, J. T., Isabelle, L. & Renganathan, V. Hydroxyl radical mediated degradation of azo dyes: evidence for benzene generation. *Environ. Sci. Technol.* **28,** 1389–93 (1994).

75. Vinodgopal, K., Bedja, I., Hotchandani, S. & Kamat, P. V. A Photocatalytic Approach for the Reductive Decolorization of Textile Azo Dyes in Colloidal Semiconductor Suspensions. *Langmuir* **10,** 1767–1771 (1994).

76. Vinodgopal, K. & Kamat, P. V. Enhanced Rates of Photocatalytic Degradation of an Azo Dye Using SnO_2/TiO_2 Coupled Semiconductor Thin Films. *Environ. Sci. Technol.* **29,** 841–5 (1995).

77. Konstantinou, I. K. & Albanis, T. A. TiO_2-assisted photocatalytic degradation of azo dyes in aqueous solution: kinetic and mechanistic investigations. *Appl. Catal. B Environ.* **49,** 1–14 (2004).

78. Lachheb, H. *et al.* Photocatalytic degradation of various types of dyes (Alizarin S, Crocein Orange G, Methyl Red, Congo Red, Methylene Blue) in water by UV-irradiated titania. *Appl. Catal. B Environ.* **39,** 75–90 (2002).

79. Guo, W., Zhang, F., Lin, C. & Wang, Z. L. Direct growth of TiO_2 nanosheet arrays on carbon fibers for highly efficient photocatalytic degradation of methyl orange. *Adv. Mater.* **24,** 4761–4 (2012).

80. Daneshvar, N., Salari, D. & Khataee, A. R. Photocatalytic degradation of azo dye acid red 14 in water: investigation of the effect of operational parameters. *J. Photochem. Photobiol. A Chem.* **157,** 111–116 (2003).

81. Sakthivel, S. *et al.* Solar photocatalytic degradation of azo dye: comparison of photocatalytic efficiency of ZnO and TiO_2. *Sol. Energy Mater. Sol. Cells* **77,** 65–82 (2003).

82. Sunada, K., Kikuchi, Y., Hashimoto, K. & Fujishima, A. Bactericidal and Detoxification Effects of TiO 2 Thin Film Photocatalysts. *Environ. Sci. Technol.* **32,** 726–728 (1998).

83. Kikuchi, Y., Sunada, K., Iyoda, T., Hashimoto, K. & Fujishima, A. Photocatalytic bactericidal effect of TiO_2 thin films: dynamic view of the active oxygen species responsible for the effect. *J. Photochem. Photobiol. A Chem.* **106,** 51–56 (1997).

84. Nikitin, N. J. & Jurjew, W. J. Absorption des Ammoniaks, der Kohlensäure, der Benzol- und Acetondämpfe durch Gele des TiO_2 und SnO_2. *Zeitschrift für Anorg. und Allg. Chemie* **171,** 281–284 (1928).

85. Milligan, W. O. & Holmes, B. G. X-Ray Diffraction Studies in the System Al_2O_3 –SnO_2 – TiO_2. *J. Phys. Chem.* **57,** 11–14 (1953).

86. SCHULTZ, A. & STUBICAN, V. Kinetics of Separation of Phases in System TiO_2-SnO_2. *Am. Ceram. Soc. Bull.* **47,** 364–& (1968).

87. Gao, C. *et al.* A facile method to prepare SnO_2 nanotubes for use in efficient SnO_2–TiO_2 core–shell dye-sensitized solar cells. *Nanoscale* **4,** 3475 (2012).

88. Green, A. N. M., Palomares, E., Haque, S. A., Kroon, J. M. & Durrant, J. R. Charge Transport versus Recombination in Dye-Sensitized Solar Cells Employing Nanocrystalline TiO_2 and SnO_2 Films. *J. Phys. Chem. B* **109,** 12525–12533 (2005).

89. Kawashima, T. *et al.* FTO/ITO double-layered transparent conductive oxide for dye-sensitized solar cells. *J. Photochem. Photobiol. A Chem.* **164,** 199–202 (2004).

90. Moon, W. J., Yu, J. H. & Choi, G. M. Selective Gas Detection of SnO_2-TiO_2 Gas Sensors. *J. Electroceramics* **13,** 707–713 (2004).

91. Wen, Z. & Tian-mo, L. Gas-sensing properties of SnO_2–TiO_2-based sensor for volatile organic compound gas and its sensing mechanism. *Phys. B Condens. Matter* **405,** 1345–1348 (2010).

92. Zakrzewska, K. & Radecka, M. TiO_2–SnO_2 system for gas sensing—Photodegradation of organic contaminants. *Thin Solid Films* **515,** 8332–8338 (2007).

93. Zeng, W. *et al.* Selective Detection of Formaldehyde Gas Using a Cd-Doped TiO_2-SnO_2 Sensor. *Sensors (Basel).* **9,** 9029–38 (2009).

94. Zuca, S., Terzi, M., Zaharescu, M. & Matiasovsky, K. Contribution to the study of SnO_2-based ceramics. *J. Mater. Sci.* **26,** 1673–1676 (1991).

95. Shi, L., Zhang, Y., Fang, D., Li, C. & Gu, H. The effect of SnO_2 on the photocatalytic activity of aerosol-made TiO_2 particles. *J. Mater. Synth. Process.* **7,** 357–363 (1999).

96. Tai, W.-P. Photoelectrochemical properties of ruthenium dye-sensitized nanocrystalline SnO_2:TiO_2 solar cells. *Sol. Energy Mater. Sol. Cells* **76,** 65–73 (2003).

97. Tai, W.-P. & Inoue, K. Eosin Y-sensitized nanostructured SnO_2/TiO_2 solar cells. *Mater. Lett.* **57,** 1508–1513 (2003).

98. Tennakone, K., Senadeera, G. K. R., Perera, V. P. S., Kottegoda, I. R. M. & De Silva, L. A. A. Dye-Sensitized Photoelectrochemical Cells Based on Porous SnO_2 /ZnO Composite and TiO_2 Films with a Polymer Electrolyte. *Chem. Mater.* **11,** 2474–2477 (1999).

99. Nasr, C., Kamat, P. V. & Hotchandani, S. Photoelectrochemistry of Composite Semiconductor Thin Films. Photosensitization of the SnO_2/TiO_2 Coupled System with a Ruthenium Polypyridyl Complex. *J. Phys. Chem. B* **102,** 10047–10056 (1998).

100. Zhou, M., Yu, J., Liu, S., Zhai, P. & Jiang, L. Effects of calcination temperatures on photocatalytic activity of SnO_2/TiO_2 composite films prepared by an EPD method. *J. Hazard. Mater.* **154,** 1141–1148 (2008).

101. Lin, C.-F., Wu, C.-H. & Onn, Z.-N. Degradation of 4-chlorophenol in TiO_2, WO_3, SnO_2, TiO_2/WO_3 and TiO_2/SnO_2 systems. *J. Hazard. Mater.* **154,** 1033–9 (2008).

102. Cai Zhen-Qian, Shen Qian-Hong, Gao Ji-Wei & Yang Hui. Low-temperature preparation of TiO_2/SnO_2 composite film and its photocatalytic activity. *J. Inorg. Mater.* **22,** 733–736 (2007).

103. Chai, S. Y., Kim, Y. S. & Lee, W. I. Photocatalytic property of TiO_2 loaded with SnO_2 nanoparticles. *J. Electroceramics* **17,** 323–326 (2006).

104. Akurati, K. K. *et al.* One-step flame synthesis of SnO_2 / TiO_2 composite nanoparticles for photocatalytic applications. *Int. J. Photoenergy* **7,** 153–161 (2005).

105. Zhang, J., Li, Q. & Cao, W. Photocatalytic properties of TiO_2-SnO_2-SiO_2 nano-composite photocatalyst prepared by supercritical fluid drying. *CHINESE J. Inorg. Chem.* **20,** 725–730 (2004).

106. Peng, F. & Ren, Y. Preparation of nano-TiO_2-SnO_2 composite film and its photocatalytic activity for toluene degradation. *CHINESE J. Catal.* **24,** 243–247 (2003).

107. Chadwick, N. *et al.* Combinatorial aerosol assisted chemical vapour deposition of a photocatalytic mixed SnO_2/TiO_2 thin film. *J. Mater. Chem. A* **2,** 5108 (2014).

108. Chadwick, N. *et al.* The Use of Time Resolved Aerosol Assisted Chemical Vapour Deposition in Mapping Metal Oxide Thin Film Growth and Fine Tuning Functional Properties. *J. Mater. Chem. A* **03,** 4811 (2015).

109. Asahi, R., Morikawa, T., Ohwaki, T., Aoki, K. & Taga, Y. Visible-light photocatalysis in nitrogen-doped titanium oxides. *Science* **293,** 269–71 (2001).

110. Saha, N. C. & Tompkins, H. G. Titanium nitride oxidation chemistry: An x-ray photoelectron spectroscopy study. *J. Appl. Phys.* **72,** 3072 (1992).

111. Morikawa, T., Asahi, R., Ohwaki, T., Aoki, K. & Taga, Y. Band-Gap Narrowing of Titanium Dioxide by Nitrogen Doping. *Jpn. J. Appl. Phys.* **40,** L561–L563 (2001).

112. Quesada-Cabrera, R., Sotelo-Vazquez, C., Darr, J. A. & Parkin, I. P. Critical influence of surface nitrogen species on the activity of N-doped TiO_2 thin-films during photodegradation of stearic acid under UV light irradiation. *Appl. Catal. B Environ.* **160-161,** 582–588 (2014).

113. Yoshida, T., Niimi, S., Yamamoto, M., Nomoto, T. & Yagi, S. Effective nitrogen doping into TiO_2 (N-TiO_2) for visible light response photocatalysis. *J. Colloid Interface Sci.* **447,** 278–81 (2015).

114. Kachina, A. *et al.* A New Approach to the Preparation of Nitrogen-Doped Titania Visible Light Photocatalyst. *Chem. Mater.* **24,** 636–642 (2012).

115. Di Valentin, C., Pacchioni, G., Selloni, A., Livraghi, S. & Giamello, E. Characterization of paramagnetic species in N-doped TiO_2 powders by EPR spectroscopy and DFT calculations. *J. Phys. Chem. B* **109,** 11414–9 (2005).

116. Ruzimuradov, O. *et al.* A facile preparation of dual-phase nitrogen-doped TiO_2–$SrTiO_3$ macroporous monolithic photocatalyst for organic dye photodegradation under visible light. *J. Eur. Ceram. Soc.* **35,** 1815–1821 (2015).

117. Di Valentin, C. *et al.* N-doped TiO_2: Theory and experiment. *Chem. Phys.* **339,** 44–56 (2007).

118. Finazzi, E., DiValentin, C., Selloni, A. & Pacchioni, G. First Principles Study of Nitrogen Doping at the Anatase TiO_2(101) Surface. *J. Phys. Chem. C* **111,** 9275–9282 (2007).

119. Chen, H. & Dawson, J. a. The Nature of Nitrogen-doped Anatase TiO_2 and the Origin of Its Visible-light Activity. *J. Phys. Chem. C* 150619120825001 (2015). doi:10.1021/acs.jpcc.5b03587

120. Sotelo-Vazquez, C., Quesada-Cabrera, R., Darr, J. A. & Parkin, I. P. Single-step synthesis of doped TiO_2 stratified thin-films by atmospheric-pressure chemical vapour deposition. *J. Mater. Chem. A* **2,** 7082 (2014).

121. Sato, S., Nakamura, R. & Abe, S. Visible-light sensitization of TiO_2 photocatalysts by wet-method N doping. *Appl. Catal. A Gen.* **284,** 131–137 (2005).

122. Graciani, J., Fdez Sanz, J., Asaki, T., Nakamura, K. & Rodriguez, J. A. Interaction of oxygen with TiN(001): N<-->O exchange and oxidation process. *J. Chem. Phys.* **126,** 244713 (2007).

123. Chen, H. *et al.* Reaction of NH_3 with Titania: N-Doping of the Oxide and TiN Formation. *J. Phys. Chem. C* **111,** 1366–1372 (2007).

124. Breault, T. M. & Bartlett, B. M. Lowering the Band Gap of Anatase-Structured TiO_2 by Coalloying with Nb and N: Electronic Structure and Photocatalytic Degradation of Methylene Blue Dye. *J. Phys. Chem. C* **116,** 5986–5994 (2012).

125. Breault, T. M. & Bartlett, B. M. Composition Dependence of TiO_2 :(Nb,N)- x Compounds on the Rate of Photocatalytic Methylene Blue Dye Degradation. *J. Phys. Chem. C* **117,** 8611–8618 (2013).

126. Zhang, P., Yin, S., Sekino, T., Lee, S. W. & Sato, T. Nb and N co-doped TiO_2 for a high-performance NO_x photocatalyst under visible LED light irradiation. *Res. Chem. Intermed.* **39,** 1509–1515 (2012).

127. Bhachu, D. S. *et al.* Solution Processing Route to Multifunctional Titania Thin Films: Highly Conductive and Photcatalytically Active Nb:TiO[sub 2]. *Adv. Funct. Mater.* **24,** 5075–5085 (2014).

128. Arbiol, J. *et al.* Effects of Nb doping on the TiO_2 anatase-to-rutile phase transition. *J. Appl. Phys.* **92,** 853 (2002).

129. J.F. Moulder, W.F. Stickle, P.E. Sool, K.D. Bomben. *Handbook of X-ray Photoelectron Spectroscopy, Perkin-Elmer, Eden Prairie.* (1992).

130. Furubayashi, Y. *et al.* A transparent metal: Nb-doped anatase TiO_2. *Appl. Phys. Lett.* **86,** 1–3 (2005).

131. Tsurumi, T., Nishizawa, S., Ohashi, N. & Ohgaki, T. Electric Properties of Zinc Oxide Epitaxial Films Grown by Ion-Beam Sputtering with Oxygen-Radical Irradiation. *Jpn. J. Appl. Phys.* **38,** 3682–3688 (1999).

132. Shigesato, Y., Paine, D. C. & Haynes, T. E. Study of the effect of ion implantation on the electrical and microstructural properties of tin-doped indium oxide thin films. *J. Appl. Phys.* **73,** 3805 (1993).

133. Lewis, B. G. & Paine, D. C. Applications and Processing of Transparent Conducting Oxides. *MRS Bull.* **25,** 22–27 (2011).

134. Minami, T. New n-Type Transparent Conducting Oxides. *MRS Bull.* **25,** 38–44 (2011).

135. Lü, X. *et al.* Improved-Performance Dye-Sensitized Solar Cells Using Nb-Doped TiO_2 Electrodes: Efficient Electron Injection and Transfer. *Adv. Funct. Mater.* **20,** 509–515 (2010).

136. Atashbar, M. Z., Sun, H. T., Gong, B., Wlodarski, W. & Lamb, R. XPS study of Nb-doped oxygen sensing TiO_2 thin films prepared by sol-gel method. *Thin Solid Films* **326,** 238–244 (1998).

137. Cottineau, T. *et al.* One step synthesis of niobium doped titania nanotube arrays to

form (N,Nb) co-doped TiO_2 with high visible light photoelectrochemical activity. *J. Mater. Chem. A* **1,** 2151–2160 (2013).

138. Emeline, A. V *et al.* Photoelectrochemical behavior of Nb-doped TiO_2 electrodes. *J. Phys. Chem. B* **109,** 24441–4 (2005).

139. Knapp, C. E., Kafizas, A., Parkin, I. P. & Carmalt, C. J. The use of combinatorial aerosol-assisted chemical vapour deposition for the formation of gallium-indium-oxide thin films. *J. Mater. Chem.* **21,** 12644 (2011).

140. Chadwick, N. *et al.* Combinatorial aerosol assisted chemical vapour deposition of a photocatalytic mixed SnO_2/TiO_2 thin film. *J. Mater. Chem. A* **2,** 5108 (2014).

141. Kafizas, A., Dunnill, C. W. & Parkin, I. P. Combinatorial atmospheric pressure chemical vapour deposition (cAPCVD) of niobium doped anatase; effect of niobium on the conductivity and photocatalytic activity. 8336–8349 (2010). doi:10.1039/c0jm01244k

142. Kafizas, A. *et al.* Combinatorial atmospheric pressure chemical vapor deposition of F:TiO_2; The relationship between photocatalysis and transparent conducting oxide properties. *Adv. Funct. Mater.* **24,** 1758–1771 (2014).

143. Wilkinson, M. *et al.* Combinatorial atmospheric pressure chemical vapor deposition of graded TiO_2-VO_2 mixed-phase composites and their dual functional property as self-cleaning and photochromic window coatings. *ACS Comb. Sci.* **15,** 309–19 (2013).

144. Sathasivam, S. *et al.* Combinatorial Atmospheric Pressure CVD of a Composite TiO_2 /SnO_2 Thin Film. *Chem. Vap. Depos.* **20,** 69–79 (2014).

145. Kafizas, A. & Parkin, I. P. The combinatorial atmospheric pressure chemical vapour deposition (cAPCVD) of a gradating N-doped mixed phase titania thin film. *J. Mater. Chem.* **20,** 2157 (2010).

146. Kafizas, A. & Parkin, I. P. Combinatorial Atmospheric Pressure Chemical Vapor Deposition (cAPCVD): A Route to Functional Property Optimization. *J. Am. Chem. Soc.* **133,** 20458 (2011).

147. Choy, K. Chemical vapour deposition of coatings. *Prog. Mater. Sci.* **48,** 57–170 (2003).

148. Hou, X. & Choy, K. L. Processing and Applications of Aerosol-Assisted Chemical Vapor Deposition. *Chem. Vap. Depos.* **12,** 583–596 (2006).

149. Kafizas, A., Adriaens, D., Mills, A. & Parkin, I. P. Simple method for the rapid simultaneous screening of photocatalytic activity over multiple positions of self-

cleaning films. *Phys. Chem. Chem. Phys.* **11,** 8367–75 (2009).

150. Kiel, S. *et al.* Forming nanoparticles of water-soluble ionic molecules and embedding them into polymer and glass substrates. *Beilstein J. Nanotechnol.* **3,** 267–76 (2012).

151. Bragg, W. H. & Bragg, W. L. The Reflection of X-rays by Crystals. *Proc. R. Soc. A Math. Phys. Eng. Sci.* **88,** 428–438 (1913).

152. Cowley, J. *Diffraction physics*. (North-Holland Pub. Co. ;;American Elsevier, 1975).

153. The Nobel Prize in Physics 1921. at <http://www.nobelprize.org/nobel_prizes/physics/laureates/1921/>

154. Goudsmit, S. A. & Richards, P. I. The Order of Electron Shells in Ionized Atoms. *Proc. Natl. Acad. Sci.* **51,** 664–671 (1964).

155. Rubio, G. D. & Danişman, T. The Spider Genus Mazax (Araneae: Corinnidae: Castianeirinae) Newly Recorded from South America, with the Description of a New Species. *Florida Entomol.* **97,** 1182–1190 (2014).

156. Kendir, G., Güvenç, A., Acar, A., Çeter, T. & Pınar, N. M. Fruits, seeds and pollen morphology of Turkish Ribes L. (Grossulariaceae). *Plant Syst. Evol.* **301,** 185–199 (2014).

157. Scanning Electron Microscopy - Physics of Image Formation and Microanalysis. at <http://www.springer.com/physics/optics+%26+lasers/book/978-3-540-63976-3>

158. Swanepoel, R. Determination of the thickness and optical constants of amorphous silicon. *J. Phys. E.* **16,** 1214 (1983).

159. Tauc, J. Optical properties and electronic structure of amorphous Ge and Si. *Mater. Res. Bull.* **3,** 37–46 (1968).

160. Yoshihara, T. *et al.* Identification of Reactive Species in Photoexcited Nanocrystalline TiO_2 Films by Wide-Wavelength-Range (400−2500 nm) Transient Absorption Spectroscopy. *J. Phys. Chem. B* **108,** 3817–3823 (2004).

161. Alfano, J. C., Walhout, P. K., Kimura, Y. & Barbara, P. F. Ultrafast transient-absorption spectroscopy of the aqueous solvated electron. *J. Chem. Phys.* **98,** 5996 (1993).

162. Logunov, S. L., Ahmadi, T. S., El-Sayed, M. A., Khoury, J. T. & Whetten, R. L. Electron Dynamics of Passivated Gold Nanocrystals Probed by Subpicosecond Transient Absorption Spectroscopy. *J. Phys. Chem. B* **101,** 3713–3719 (1997).

163. Ohkita, H. *et al.* Charge carrier formation in polythiophene/fullerene blend films studied by transient absorption spectroscopy. *J. Am. Chem. Soc.* **130,** 3030–42 (2008).

164. Mills, A. & Le Hunte, S. An overview of semiconductor photocatalysis. *J. Photochem. Photobiol. A Chem.* **108,** 1–35 (1997).

165. Smits, F. M. Measurement of Sheet Resistivities with the Four-Point Probe. *Bell Syst. Tech. J.* **37,** 711–718 (1958).

166. Dieter K. Schroder. *Semiconductor Material and Device Characterization.* (2006). at <http://eu.wiley.com/WileyCDA/WileyTitle/productCd-0471739065.html>

167. Ponja, S. *et al.* Aerosol assisted chemical vapour deposition of hydrophobic TiO_2–SnO_2 composite film with novel microstructure and enhanced photocatalytic activity. *J. Mater. Chem. A* **1,** 6271 (2013).

168. Mills, A., Wang, J., Lee, S.-K. & Simonsen, M. An intelligence ink for photocatalytic films. *Chem. Commun. (Camb).* 2721–3 (2005). doi:10.1039/b501131k

169. Noor, N. & Parkin, I. P. Halide doping effects on transparent conducting oxides formed by aerosol assisted chemical vapour deposition. *Thin Solid Films* **532,** 26–30 (2013).

170. Tahir, A. A., Peiris, T. a. N. & Wijayantha, K. G. U. Enhancement of Photoelectrochemical Performance of AACVD-produced TiO2 Electrodes by Microwave Irradiation while Preserving the Nanostructure. *Chem. Vap. Depos.* **18,** 107–111 (2012).

171. Ali, S. M., Hussain, S. T., Bakar, S. A., Muhammad, J. & Rehman, N. U. Effect of doping on the Structural and Optical Properties of SnO_2 Thin Films fabricated by Aerosol Assisted Chemical Vapor Deposition. *J. Phys. Conf. Ser.* **439,** 012013 (2013).

172. Yoon, J., Oh, H. K. & Kwag, Y. J. Structural and Optical Properties of TiO_2-SiO_2 Composite Films Prepared by Aerosol-Assisted Chemical-Vapor Deposition. *J. Korean Phys. Soc.* **33,** 699–704 (1998).

173. Kamble, V. B. & Umarji, A. M. Defect induced optical bandgap narrowing in undoped SnO2 nanocrystals. *AIP Adv.* **3,** 082120 (2013).

174. Reddy, K. M., Manorama, S. V & Reddy, A. R. Bandgap studies on anatase titanium dioxide nanoparticles ☪ **78,** 239–245 (2002).

175. Sarah, M. S. P., Musa, M. Z., Asiah, M. N. & Rusop, M. Electrical conductivity

characteristics of TiO<inf>2</inf> thin film. *Electron. Devices, Syst. Appl. (ICEDSA), 2010 Intl Conf* 361–364 (2010). doi:10.1109/ICEDSA.2010.5503040

176. Lai, K., Sun, Y., Chen, H., Zhi, L. & Wei, W. Effect of oxygen vacancy and Al-doping on the electronic and optical properties in SnO_2. *Phys. B Condens. Matter* **428,** 48–52 (2013).

177. Gubanov, V. A. & Medvedeva, N. I. Electronic band structure and chemical bonding in the transition metal dioxides. *Phys. B Condens. Matter* **172,** 285–288 (1991).

178. Villamagua, L. *et al.* Change in the electrical conductivity of SnO_2 crystal from n-type to p-type conductivity. *Chem. Phys.* **452,** 71–77 (2015).

179. Akurati, K. K. *et al.* One-step flame synthesis of SnO_2/TiO_2 composite nanoparticles for photocatalytic applications. *Int. J. Photoenergy* **07,** (2005).

180. Wang, H.-J. & Lee, S.-C. Photo-Catalytic Activity of Different Thicknesses TiO_2/SnO_2 Double Layer Nano Composite Thin Films. *Mater. Trans.* **50,** 2329–2334 (2009).

181. Oropeza, F. E., Davies, B., Palgrave, R. G. & Egdell, R. G. Electronic basis of visible region activity in high area Sn-doped rutile TiO_2 photocatalysts. *Phys. Chem. Chem. Phys.* **13,** 7882–91 (2011).

182. Jiang, H. B. *et al.* Enhancing photocatalytic activity of Sn doped TiO_2 dominated with {105} facets. *Catal. Today* **225,** 18–23 (2014).

183. Li, J. & Zeng, H. C. Hollowing Sn-doped TiO_2 nanospheres via ostwald ripening. *J. Am. Chem. Soc.* **129,** 15839–47 (2007).

184. Lin, Z. *et al.* Polymer monolithic capillary column fabricated by using monodisperse iron oxide nanocrystal template to enhance the electrochromatographic separation of small molecules. *Electrophoresis* **35,** 1947–55 (2014).

185. Garipcan, B. *et al.* Controllable formation of nanoscale patterns on TiO_2 by conductive-AFM nanolithography. *Langmuir* **24,** 8944–9 (2008).

186. Bao, X.-M. *et al.* Facile preparation of superhydrophobic surfaces based on metal oxide nanoparticles. *Appl. Surf. Sci.* **303,** 473–480 (2014).

187. Balachandran, S., Praveen, S. G., Velmurugan, R. & Swaminathan, M. Facile fabrication of highly efficient, reusable heterostructured Ag–ZnO–CdO and its twin applications of dye degradation under natural sunlight and self-cleaning. *RSC Adv.* **4,** 4353 (2014).

188. Whitehouse, D. *Surfaces and their Measurements*. (2012).

189. Trotochaud, L. & Boettcher, S. W. Synthesis of Rutile-Phase $Sn_xTi_{1-x}O_2$ Solid-Solution and $(SnO_{2-x} / TiO_2)_{1-x}$ Core / Shell Nanoparticles with Tunable Lattice Constants and Controlled Morphologies. *Chem. Mater.* **23,** 4920–4930 (2011).

190. Karam, A. What Percentage of natural Sunlight is UV Rays? (2005). at <http://www.madsci.org/posts/archives/2005-06/1119964750.En.r.html>

191. Zou, Z., Ye, J., Sayama, K. & Arakawa, H. Direct splitting of water under visible light irradiation with an oxide semiconductor photocatalyst. *Nature* **414,** 625–7 (2001).

192. Ayieko, C. O., Musembi, R. J., Waita, S. M., Aduda, B. O. & Jain, P. K. Structural and Optical Characterization of Nitrogen-doped TiO_2 Thin Films Deposited by Spray Pyrolysis on Fluorine Doped Tin Oxide (FTO) Coated Glass Slides. **2,** 67–72 (2012).

193. Kuznetsov, V. N. & Serpone, N. Visible light absorption by various titanium dioxide specimens. *J. Phys. Chem. B* **110,** 25203–9 (2006).

194. Li, D., Haneda, H., Labhsetwar, N. K., Hishita, S. & Ohashi, N. Visible-light-driven photocatalysis on fluorine-doped TiO_2 powders by the creation of surface oxygen vacancies. *Chem. Phys. Lett.* **401,** 579–584 (2005).

195. Li, D., Ohashi, N., Hishita, S., Kolodiazhnyi, T. & Haneda, H. Origin of visible-light-driven photocatalysis: A comparative study on N/F-doped and N–F-codoped TiO_2 powders by means of experimental characterizations and theoretical calculations. *J. Solid State Chem.* **178,** 3293–3302 (2005).

196. Zeng, L. *et al.* Comparative study on the visible light driven photocatalytic activity between substitutional nitrogen doped and interstitial nitrogen doped TiO_2. *Appl. Catal. A Gen.* **488,** 239–247 (2014).

197. Maeda, M. & Watanabe, T. Visible Light Photocatalysis of Nitrogen-Doped Titanium Oxide Films Prepared by Plasma-Enhanced Chemical Vapor Deposition. *J. Electrochem. Soc.* **153,** C186 (2006).

198. Hu, X. *et al.* Nitrogen atom diffusion into TiO_2 anatase bulk via surfaces. *Comput. Mater. Sci.* **82,** 107–113 (2014).

199. Powell, M. J., Palgrave, R. G., Dunnill, C. W. & Parkin, I. P. A fast and effective method for N-doping TiO_2 by post treatment with liquid ammonia: visible light photocatalysis. *Thin Solid Films* **562,** 223–228 (2014).

200. Asahi, R., Morikawa, T., Ohwaki, T., Aoki, K. & Taga, Y. Visible-light photocatalysis in nitrogen-doped titanium oxides. *Science* **293,** 269–71 (2001).

201. Tamaki, Y. *et al.* Dynamics of efficient electron-hole separation in TiO_2 nanoparticles revealed by femtosecond transient absorption spectroscopy under the weak-excitation condition. *Phys. Chem. Chem. Phys.* **9,** 1453–60 (2007).

202. Tang, J., Durrant, J. R. & Klug, D. R. Mechanism of photocatalytic water splitting in TiO_2. Reaction of water with photoholes, importance of charge carrier dynamics, and evidence for four-hole chemistry. *J. Am. Chem. Soc.* **130,** 13885–91 (2008).

203. Yamanaka, K. & Morikawa, T. Charge-Carrier Dynamics in Nitrogen-Doped TiO_2 Powder Studied by Femtosecond Time-Resolved Diffuse Reflectance Spectroscopy. *J. Phys. Chem. C* **116,** 1286–1292 (2012).

204. Pesci, F. M., Wang, G., Klug, D. R., Li, Y. & Cowan, A. J. Efficient Suppression of Electron − Hole Recombination in Oxygen- Defi cient Hydrogen-Treated TiO_2 Nanowires for Photoelectrochemical Water Splitting. (2013).

205. Powell, M. J., Dunnill, C. W. & Parkin, I. P. N-doped TiO_2 visible light photocatalyst films via a sol–gel route using TMEDA as the nitrogen source. *J. Photochem. Photobiol. A Chem.* **281,** 27–34 (2014).

206. QIAN, H. X., ZHOU, W. & ZHENG, H. Y. Cracking anf Exfoliation of TiO_2 Film Irradiated with Excimer Laser. *Surf. Rev. Lett.* **15,** 473–479 (2008).

207. Squadrito, G. L. & Pryor, W. A. Oxidative chemistry of nitric oxide: the roles of superoxide, peroxynitrite, and carbon dioxide. *Free Radic. Biol. Med.* **25,** 392–403 (1998).

208. Nosaka, Y., Daimon, T., Nosaka, A. Y. & Murakami, Y. Singlet oxygen formation in photocatalytic TiO_2 aqueous suspension. *Phys. Chem. Chem. Phys.* **6,** 2917 (2004).

209. Palgrave, R. G., Payne, D. J. & Egdell, R. G. Nitrogen diffusion in doped TiO_2 (110) single crystals: a combined XPS and SIMS study. *J. Mater. Chem.* **19,** 8418 (2009).

210. Henderson, M. A. A surface perspective on self-diffusion in rutile TiO_2. *Surf. Sci.* **419,** 174–187 (1999).

211. Henderson, M. A. Mechanism for the bulk-assisted reoxidation of ion sputtered TiO_2 surfaces: diffusion of oxygen to the surface or titanium to the bulk? *Surf. Sci.* **343,** L1156–L1160 (1995).

212. Kofstad, P. Note on the defect structure of rutile TiO_2. *J. Less Common Met.* **13,** 635–638 (1967).

213. Zhou, Y. *et al.* A facile approach to further improve the substitution of nitrogen into reduced TiO_{2-x} with an enhanced photocatalytic activity. *Appl. Catal. B Environ.* **170-171,** 66–73 (2015).

214. Wang, Y., Feng, C., Zhang, M., Yang, J. & Zhang, Z. Enhanced visible light photocatalytic activity of N-doped TiO_2 in relation to single-electron-trapped oxygen vacancy and doped-nitrogen. *Appl. Catal. B Environ.* **100,** 84–90 (2010).

215. J. Frank, A., Kopidakis, N. & Lagemaat, J. Van De. Electrons in nanostructured TiO_2 solar cells: transport, recombination and photovoltaic properties. *Coord. Chem. Rev.* **248,** 1165–1179 (2004).

216. Andrei, C., O'Reilly, T. & Zerulla, D. A spatially resolved study on the Sn diffusion during the sintering process in the active layer of dye sensitised solar cells. *Phys. Chem. Chem. Phys.* **12,** 7241–5 (2010).

217. Bossmann, S. H. *et al.* Electron Transfer Photocatalysis. 5374–5382 (2001).

218. Irie, H., Watanabe, Y. & Hashimoto, K. Carbon-doped Anatase TiO_2 Powders as a Visible-light Sensitive Photocatalyst. *Chem. Lett.* **32,** 772–773 (2003).

219. Bawaked, S. M. *et al.* Aerosol assisted chemical vapor deposition of conductive and photocatalytically active tantalum doped titanium dioxide films. *J. Mater. Chem. A* **2,** 12849 (2014).

220. Jaimy, K. B., Safeena, V. P., Ghosh, S., Hebalkar, N. Y. & Warrier, K. G. K. Photocatalytic activity enhancement in doped titanium dioxide by crystal defects. *Dalton Trans.* **41,** 4824–32 (2012).

221. Marchiori, C. *et al.* Unraveling the Cooperative Mechanism of Visible-Light Absorption in Bulk N,Nb Codoped TiO_2 Powders of Nanomaterials. *J. Phys. Chem. C* **118,** 24152–24164 (2014).

222. Kurita, D., Ohta, S., Sugiura, K., Ohta, H. & Koumoto, K. Carrier generation and transport properties of heavily Nb-doped anatase TiO_2 epitaxial films at high temperatures. *J. Appl. Phys.* **100,** 096105 (2006).

223. Hitosugi, T. *et al.* Electronic band structure of transparent conductor: Nb-doped anatase TiO_2. *Appl. Phys. Express* **1,** 1112031–1112033 (2008).

224. Liu, Y. *et al.* Niobium-doped titania nanoparticles: Synthesis and assembly into mesoporous films and electrical conductivity. *ACS Nano* **4,** 5373–5381 (2010).

225. Cottineau, T. *et al.* One step synthesis of niobium doped titania nanotube arrays to form (N,Nb) co-doped TiO_2 with high visible light photoelectrochemical activity. *J. Mater. Chem. A* **1,** 2151 (2013).

226. Lim, J. *et al.* Synergic photocatalytic effects of nitrogen and niobium co-doping in TiO_2 for the redox conversion of aquatic pollutants under visible light. *J. Catal.* **310,** 91–99 (2014).

227. Ghicov, A., Yamamoto, M. & Schmuki, P. Lattice widening in niobium-doped TiO_2 nanotubes: Efficient ion intercalation and swift electrochromic contrast. *Angew. Chemie - Int. Ed.* **47,** 7934–7937 (2008).

228. Kafizas, A., Dunnill, C. W. & Parkin, I. P. Combinatorial atmospheric pressure chemical vapour deposition (cAPCVD) of niobium doped anatase; effect of niobium on the conductivity and photocatalytic activity. *J. Mater. Chem.* **20,** 8336 (2010).

229. Zhang, S. X. *et al.* Niobium doped TiO_2: Intrinsic transparent metallic anatase versus highly resistive rutile phase. *J. Appl. Phys.* **102,** 013701 (2007).

230. Yu, Y. P., Liu, W., Wu, S. X. & Li, S. W. Impact of Nitrogen Doping on Electrical Conduction in Anatase TiO_2 Thin Films. *J. Phys. Chem. C* **116,** 19625–19629 (2012).

231. Minami, T. Transparent conducting oxide semiconductors for transparent electrodes. *Semicond. Sci. Technol.* **20,** S35–S44 (2005).